

Politecnico di Torino



Corso di Laurea Magistrale in Ingegneria Aerospaziale

Tesi di Laurea Magistrale

Characterization of Inconel 625/TiC composite fabricated by Laser Powder Bed Fusion

Relatore:

Prof.ssa Sara Biamino

Correlatore:

Dott. Giulio Marchese

Candidato:

Daniele Nigro

Aprile 2021

Contents

Contents.....	I
1 Riassunto in italiano	1
2 Introduction	Error! Bookmark not defined.
3 Additive Manufacturing (AM)	5
3.1 Powder atomization techniques.....	5
3.2 Materials for additive manufacturing.....	6
3.3 Additive manufacturing techniques.....	6
3.3.1 Stereolithography	6
3.3.2 Directed Energy Deposition (DED)	7
3.3.3 Electron Beam Melting (EBM).....	8
3.3.4 Laser Powder Bed Fusion (LPBF).....	9
3.4 Additive manufacturing in aerospace applications.....	14
4 Superalloys	17
4.1.1 Superalloy categories and composition.....	17
4.1.2 Microstructure	19
4.2 Superalloys in aerospace applications.....	20
4.2.1 Introduction	20
4.2.2 Jet engine materials	21
4.3 Superalloys for LPBF.....	24
4.4 Inconel 625 (IN625).....	25
4.4.1 Wrought Inconel 625.....	25
4.4.2 Evolution of Inconel 625.....	28
4.4.3 LPBFed Inconel 625.....	28
4.5 Metal matrix composite (MMC)	29
4.5.1 General overview	29
4.5.2 TiC/Inconel 625 MMC.....	30
5 Materials and methods.....	33
5.1 Flowability and apparent density test.....	33
5.2 Samples production	34
5.3 Archimedes' method	36
5.4 Heat treatments.....	37
5.5 Metallographic preparation	37

5.6	Samples analysis	38
5.6.1	Optical microscope.....	38
5.6.2	SEM microscope	39
5.6.3	ImageJ analysis	39
5.7	Brinell hardness tests.....	40
5.8	Tensile tests.....	41
6	Results	43
6.1	Powder characterization	43
6.2	Porosity and parameters optimization	44
6.3	Microstructure	47
6.3.1	Microstructure of samples in as-built condition (AB).....	47
6.3.2	Microstructure of samples solutioned at 1150 °C for 2 hours (HT1).....	51
6.3.3	Microstructure of samples solutioned at 1150 °C for 2 hours and aged at 700 °C for 8 hours (HT2).....	55
6.3.4	Microstructure of samples solutioned at 980 °C for 1 hour (HT3)	59
6.3.5	Microstructure of samples solutioned at 870 °C for 1 hour (HT4)	62
6.3.6	Microstructure of samples solutioned at 1190 °C for 2 hours (HT5).....	66
6.4	Brinell hardness tests.....	68
6.5	Tensile tests.....	70
7	Conclusions	71
8	References	72
9	Acknowledgements	78

1 Riassunto in italiano

Il settore aerospaziale ha avuto una crescita pressoché costante sin dalla sua nascita. I progressi conseguiti in questo ambito sono fortemente correlati con le innovazioni nel campo della scienza dei materiali, in quanto le prestazioni di un veicolo aerospaziale dipendono fortemente dalle proprietà fisiche e meccaniche dei materiali impiegati per la costruzione dei componenti. In particolare, per un velivolo i motori sono i componenti che devono resistere alle condizioni più avverse, in quanto devono sottostare a temperature estremamente alte, elevati sforzi meccanici e ad ambienti molto corrosivi, soprattutto all'altezza del combustore e delle turbine. Proprio per questi componenti, le superleghe hanno trovato largo impiego grazie alla loro fenomenale proprietà di poter operare a temperature molto vicine alla temperatura di fusione del materiale, abbinata alla eccellente resistenza alla corrosione e all'ossidazione, e alle buone proprietà meccaniche sia a temperature criogeniche che ad alte temperature. Tra le superleghe utilizzate in un motore aeronautico troviamo l'Inconel 625 che è una superlega di nichel rafforzata per soluzione solida e che presenta tra le migliori resistenze alla corrosione e all'ossidazione fra tutte le superleghe, in presenza di una buona duttilità e di ottime proprietà meccaniche fino a 650 °C, con la possibilità di utilizzarla fino a 1000 °C se non sono richieste prestazioni meccaniche eccessive. Per queste proprietà, l'Inconel 625 viene spesso utilizzato all'interno di un motore aeronautico, in particolare nei sistemi di scarico.

Le superleghe sono, tuttavia, molto difficili da lavorare con le tecniche di manifattura tradizionali, quindi per ottenere dei componenti di forma complessa sono necessarie numerose e costose lavorazioni. Negli ultimi decenni, si sono effettuati molti sviluppi e caratterizzazioni di alcuni materiali nell'ambito dell'additive manufacturing, conosciuto anche come stampa 3D, con il quale è possibile ottenere dei componenti che sono molto vicini alla loro forma finale (near net-shape) già con il solo processo di produzione, offrendo in particolare al settore aerospaziale la possibilità di realizzare componenti più complessi, più performanti e più leggeri. Tra le varie tecniche di additive manufacturing, quella del laser powder bed fusion (LPBF) è tra le più utilizzate, con la quale si stanno caratterizzando diversi materiali. L'Inconel 625 fa parte di questi materiali che presentano una buona affinità con metodo del LPBF grazie alla buona saldabilità della superlega, consentendo di ottenere dei campioni con una densità relativa molto vicina al 100 %.

La crescente necessità nel campo aerospaziale di sottostare alle sempre più stringenti normative riguardanti le emissioni di agenti inquinanti, abbinati al progresso tecnologico dei velivoli, richiedono materiali sempre più performanti, che resistano a sempre più alte temperature e che siano più leggeri con lo scopo di ridurre il peso del velivolo ed aumentare le temperature operative di un motore aeronautico, migliorando le prestazioni del velivoli in termini di spinta e impulso specifico, riducendone i consumi. Negli ultimi anni si stanno studiando i materiali compositi, ovvero dei materiali che presentano una matrice e un rinforzante di due classi di materiali diversi, con lo scopo di ottenere dei materiali che sfruttano i vantaggi di due classi. Tra questi esistono i compositi a matrice metallica (MMC) che presentano un metallo come matrice e un rinforzante che di solito è un materiale ceramico.

L'oggetto di questa tesi è un materiale composito formato da una matrice di Inconel 625 e un rinforzante ceramico di carburo di titanio (TiC) in polveri micrometriche, prodotto per LPBF,

con lo scopo di confrontare il composito con la lega base in termini di densificazione, evoluzione della microstruttura e proprietà meccaniche. Studi preliminari potrebbero portare questo materiale composito ad essere utilizzato nel settore aerospaziale. Per questo scopo, sono stati effettuati dei test di flowability sulla polvere di Inconel 625 caricata con diverse percentuali in peso di TiC, trovando che le polveri scorrono all'interno di un Carney flowmeter solo fino all'1 % in peso di rinforzante, mentre la flowability è estremamente ridotta per concentrazioni di TiC più elevate. Questo significa che la presenza del ceramico rinforzante non solo influisce sulla fase di fusione e solidificazione, ma anche già durante lo spargimento del letto di polvere, e che concentrazioni superiori al 1 % in peso possono rendere difficoltoso uno spargimento uniforme di polvere, portando la formazione di difetti. Lo studio preliminare sulle polveri ha determinato che il materiale presenta una discreta flowability fino a 1 % in TiC. Per questo motivo si sono prodotti dei campioni di composito con l'1 % in peso di TiC, riuscendo ad ottenere dei campioni con una densità relativa vicina al 100 %. Tuttavia, si è notato che i parametri di processo ottimali si ottengono con valori di volumetri energy density (VED) più elevati rispetto alla lega base. Questo perché le particelle di TiC alterano la viscosità del pozzetto di fusione ed è necessaria una maggiore energia per ottenere un buon spargimento del fuso.

Il primo risultato trovato è che i grani del composito sono molto più fini rispetto alla lega base, e questo è evidente laddove la concentrazione di particelle di TiC è maggiore. Questo è probabilmente dovuto alla diversa durezza e conducibilità termica di matrice e rinforzante, creando dei bordi di grano attorno alle particelle di TiC che in gran parte sono posizionate all'interno dei degli stessi bordi di grano, anche se molte particelle si posizionano all'interno della matrice. Sui campioni trattati termicamente con un processo di solubilizzazione ad alta temperatura (1150 °C) si è trovato che il composito presenta ancora i grani con direzione preferenziale lungo l'asse di accrescimento del materiale (asse z), anche se la ricristallizzazione è già cominciata, mentre la lega di Inconel 625 presenta già dei grani equiassici. Questo risultato è stato associato al fatto che il TiC aumenta la stabilità termica del composito, ostacolando la ricristallizzazione dei grani. Inoltre, con i trattamenti ad alte temperature (HT1 e HT2) si ha la presenza di precipitati che sono di dimensioni anche superiori a 1 μm nei bordi di grano, mentre dei precipitati più piccoli appaiono nei bordi di grano formati durante la ricristallizzazione e all'interno della matrice. Dalle mappe EDS si è ricavato che questi precipitati sono principalmente dei carburi ricchi in niobio, ma anche in molibdeno e titanio. Il carbonio in eccesso si forma soprattutto durante il trattamento termico di solubilizzazione ad alta temperatura, con il quale si ha la parziale decomposizione del TiC in titanio e carbonio, e sembra che il carbonio in eccesso tenda a legarsi più facilmente con il niobio.

Quanto appena detto influisce sulle proprietà meccaniche e termomeccaniche del composito, infatti sono stati trovati valori di durezza Brinell, carico di snervamento e di rottura più alti rispetto a quelli della lega base, con la durezza maggiore ottenuta con il trattamento di solubilizzazione a 1150 °C più un trattamento di invecchiamento a 700 °C con il quale, oltre ai carburi, precipita anche la fase γ'' . Tuttavia, lo svantaggio principale è che la duttilità dei compositi è inferiore rispetto a quella della lega. Questi risultati rendono il composito di Inconel 625 con l'aggiunta dell'1 % in peso di polveri micrometriche di TiC un materiale potenzialmente interessante per l'impiego aerospaziale in grado di sopportare carichi superiori rispetto alla lega base. In particolare, è interessante il fatto che il composito presenti ancora dei

grani colonnari anche ad alte temperature e questo potrebbe significare che il materiale possa essere impiegato a temperature operative più elevate rispetto alla lega base di Inconel 625. Infatti, un materiale con grani colonnari ha una forma che può portare a una maggiore resistenza al creep rispetto la presenza di grani equiassici.

2 Abstract

The aerospace field has made significant progress in the last decades, making it necessary to develop materials with higher mechanical performance. For instance, Jet engines require high-temperature properties, and Ni-based superalloys are excellent candidates for this purpose. Because of the difficulties encountered in obtaining complex-shaped components, additive manufacturing (AM) offers new horizons to create near-net-shaped components with a high level of reliability. Laser powder bed fusion (LPBF) is one of the most mature AM techniques, and it is widely used for an ever-increasing number of materials.

Inconel 625 is one of the most manufactured Ni-based superalloys with LPBF techniques, thanks to its high weldability. It presents extreme corrosion and oxidation resistance (up to around 1000 °C) coupled to good properties at elevated temperatures until 650°C. However, the fabrication of composites made of Inconel 625 alloy can produce higher mechanical performance than Inconel 625 alloy, making these composites an attractive candidate for the aerospace field.

In particular, to improve the high-temperature properties, it is possible to modify the Inconel 625 alloy by adding ceramic particles obtaining a metal matrix composite (MMC). One of the best candidates for the purpose is titanium carbide (TiC), a refractory material with a high melting point and exceptional hardness, which seems to have good adhesions with Inconel 625.

In this thesis, 1 wt. % of TiC micro-powders were added to Inconel 625 powders to obtain a TiC/IN625 composite by laser powder bed fusion (LPBF). The process parameters to obtain dense composites were determined. In detail, using higher energy with respect to the production of IN625 alloy, it is possible to obtain full densification with a relative density close to 100 %. Afterward, the microstructure of the as-processed and various heat-treated composites was compared to the base alloy in the same conditions. Finally, the mechanical properties were also evaluated and compared to the base alloy. The reinforcement enhanced the hardness as well as increased the temperature necessary for recrystallization with respect to the base alloy.

3 Additive Manufacturing (AM)

Additive manufacturing (AM) was born in the late 1980s and from the beginning it has been used in aerospace applications, in fact, Pratt & Whitney was one of the first five customers [1]. The automotive and aerospace industries are trying to exploit the advantages of metal AM, so the goal for the next years is to better understand the connection between the material properties, processing method and microstructure in order to produce consistent, reliable and qualified parts suitable for engineering applications [2].

Materials which can be processed by additive manufacturing are limited, but thanks to the large potential of metals produced by AM many studies have been done in industrial and academic field, and different materials have been added in the last years. AM machinability is strongly related to the weldability of the material, so not all materials are suitable for AM processes, but many of them can be chemically tailored to fully exploit the advantages of AM.

The majority of the AM techniques require metal powders, so before showing the most important AM techniques, a description of the gas atomization process is presented.

3.1 Powder atomization techniques

Several techniques exist to atomize metals. The most common method in industry is gas atomization which schematic is presented in Figure 1. It consists of remelting the metal ingot and to nebulize metal droplets with an inert gas (argon or helium). To obtain a spheroidal and high-quality powder, the atomise chamber must be dimensioned so that nebulized droplets solidify before they hit the chamber walls. In this way, it is possible to obtain powder of different sizes (particle size granulometric), and this is advantageous to cover the vacuum between the particles during AM processes as the gaps between larger particles can be filled in with smaller particles [1], [3].

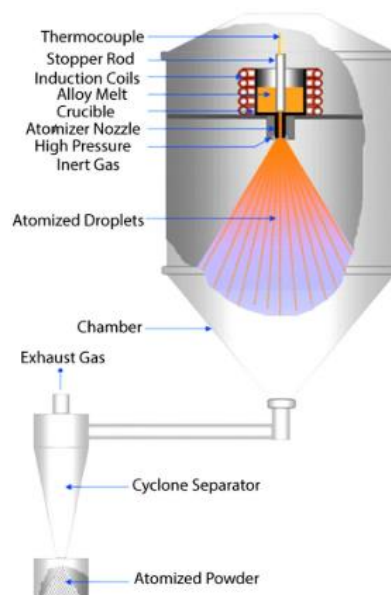


Figure 1: Gas atomization schematic [2].

Another used technique is water atomization that uses water instead of gas. The process is less expensive, but the shape of powders is irregular and low-quality due to the rapid water quenching and the high energy water jet impacting the molten stream [2].

3.2 Materials for additive manufacturing

A list of the most common alloys suitable for additive manufacturing is described in this section.

- Fe-based alloys: these materials are very diffused in engineering applications, but only a limited fraction is suitable for AM techniques. In this list are included some stainless steel such as 316-L stainless steel, 17-4 PH, maraging steel 1.2709 (MS1/M300) and H13 tool steel [2].
- Ni-based alloys: because of the difficulties to treat these materials with traditional techniques, there was a great interest on AM techniques obtaining excellent results. The most used in AM are Inconel 718, Inconel 625 and Hastelloy X alloys.
- Co-based alloys: these materials are quite useful for high-temperature applications such as aerospace and nuclear field. These alloys also exhibit good biocompatibility and are widely used in the biomedical field and in dental and orthopaedic prostheses. The primary alloy currently used in AM techniques is Co-Cr-Mo [2].
- Al-based alloys: the most used alloys used in AM techniques are those in combination with magnesium, silicon or copper. AlSi10Mg is the most researched Al-alloy in literature and AlSi₉Cu₃ is also certified and printable by companies [2].
- Ti-based alloys: these alloys have found extensive use in aerospace applications because are relatively light-weight materials with critical load bearing capabilities (high strength to weight ratio). Ti-6Al-4V was widely used for decades and it is the most researched alloy in literature, but there is a discrete number of α and β alloys that have been investigated [2].

3.3 Additive manufacturing techniques

3.3.1 Stereolithography

The patent for stereolithography was for the first time obtained in 1986, and it was the first technique used for rapid prototyping [4]. The process is suitable for photocurable resin, consisting of photopolymerizable monomers, such as acrylates and epoxides [5]. The technique is based on the curing or solidification of a photosensitive polymer when an ultraviolet laser makes contact with the resin [6]. The process starts with the building of a 3D model through a CAD and then it is converted in an STL language (Standard Tessellation Language), which generates a 2D model of each layer. The component is anchored in a platform that supports any overhanging structures. Then an UV laser is applied to solidify the resin where is request from the 2D model. This work is done for each layer until the final model is built. The advantage of this process is the material saving, as superfluous material is collected and can be reused. The principle of this process is photopolymerization which consists of the solidification of a monomer or polymer by applying ultraviolet light acting as a catalyst.

A scheme of the process is shown in Figure 2.

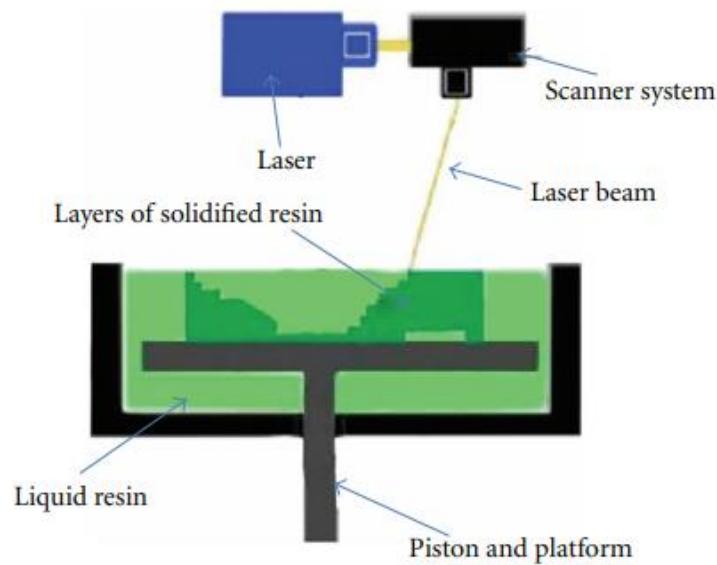


Figure 2: Stereolithography schematic [6].

Sustained progress through the years resulted in the development of an advancement of this process that offered much higher resolution, and it is known as micro stereolithography, that allows to manage a layer thickness less than $10\ \mu\text{m}$ [7].

During the process, various errors can present. Over-curing is one of the most common errors and occurs to overhang parts, due to the lack of fusion with a bottom layer. Another error is scanned line shape, which is induced by the scanning process. Moreover, the high viscosity of the liquid causes a variable layer thickness, and this introduces an error in the border position control [7].

3.3.2 Directed Energy Deposition (DED)

The directed energy deposition (DED) process is also known with other different names like 3D laser cladding and directed light fabrication. [8]. This process can be used to manufacture new parts, but it is mainly used for rapid prototyping and part repairing [9]. It consists of a laser heat source that deposits a thin metal layer on a substrate. The material (typically powder) passes through one or more nozzles, is sprinkled to the substrate by powder injection and then is melted by high-power laser. Similar to LPBF, the build volume is enclosed in a chamber where a gas is injected with cyclic purging or alternatively is released by the nozzle to shield the solidifying metal [2]. The gas must be inert to avoid the oxidation of the molten pool. Powders could be coarser than LPBF process because they are injected by a high-pressure gas and melted before contact with the molten pool [3]. Typical powder size for the DED process is typically in a range from 50 to $150\ \mu\text{m}$ [10].

It is possible to obtain high-density components with a reduced number of pores, but is also difficult to control the process because of the dynamic movement of the material powder which could cause problems of shape accuracy and powder efficiency [11]. For this reason, printed parts always require post-treatments. However, it is possible to improve the quality and complexity of the printed parts by adding additional kinematic degrees of freedom. Moreover, DED processing time is faster than LPBF. Finally DED systems can be coupled with subtractive

machining manufacturing techniques to obtain a good surface finishing and adequate dimensional tolerance for aerospace applications [2].

A schematic representation of the process is shown in Figure 3.

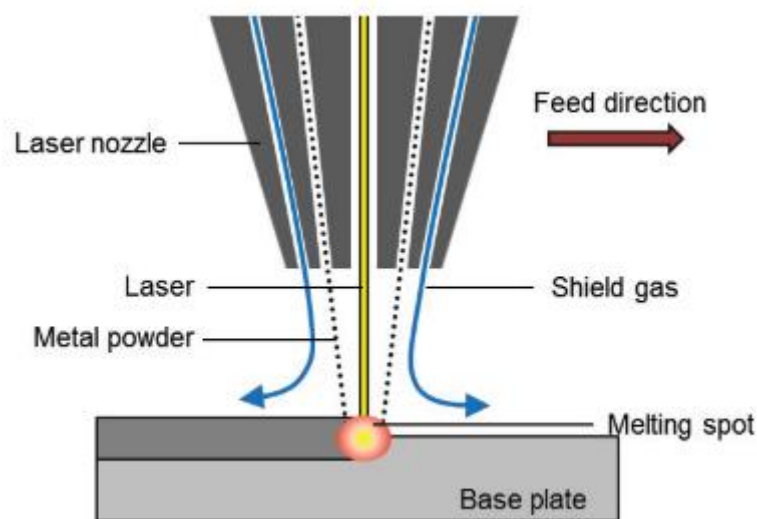


Figure 3: Direct Energy Deposition schematic [11].

3.3.3 Electron Beam Melting (EBM)

The process is similar to LPBF, but instead of a laser the power source is an electron beam driven by magnetic lenses. The power and the energy density are higher and the management of electron beam is controlled by electromagnetic coils, allowing an increased melting capability, thus leading to a higher productivity with respect to LPBF machines [4]. EBM allows to process higher layer thickness (70-200 μm [3]) and a higher size of the powder (45-150 μm) with a high production rate, however components present a worse surface finishing and roughness (30-50 μm) [4].

One of the most important differences with LPBF is that the EBM chamber works in a vacuum atmosphere (about 1×10^{-5} mbar) to prevent the dissipation of the electron beam and to reduce the level of contamination during the process, especially when reactive materials like titanium alloys are treated. Another peculiarity is that the high scanning rate allows a preheating of the powder (even up to 1100 $^{\circ}\text{C}$) to reduce the thermal stresses of the component and limiting the risk of crack formation for material with high crack susceptibility.

The most used materials for this process are TiAl alloys, especially for aerospace and marine applications [12]. Other materials, which feasibility has been evaluated with this process, are nickel-based superalloys like Inconel 625, Inconel 718, Rene142 and CMSX4, cobalt superalloys, copper, stainless steel and CoCrMo [4].

A schematic representation of the EBM machine is reported in Figure 4.

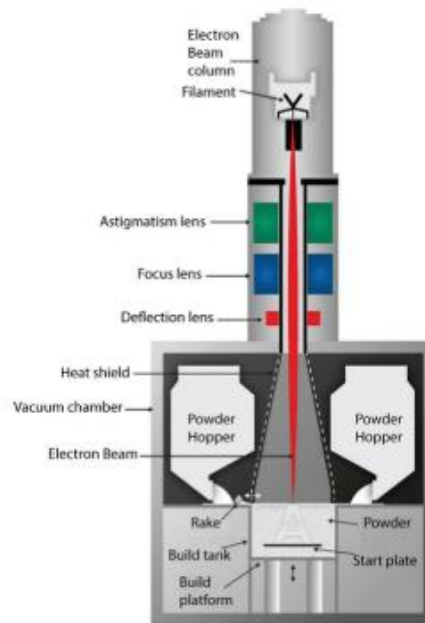


Figure 4: Schematic illustration of the EBM process [2].

3.3.4 Laser Powder Bed Fusion (LPBF)

3.3.4.1 The process

Laser Powder Bed Fusion (LPBF), also known as Selective Laser Melting (SLM) or Direct Metal Laser Sintering (DMLS) [1], [13]–[15], is one of the most promising Additive Manufacturing technique for a wide range of material. One of the main advantage of LPBF process is that it can be used as an in-process support structure for undercuts and overhangs, and therefore complex shapes with a high geometric accuracy (± 0.05 mm) can be manufactured [1].

The process starts with a 3D CAD model which must be converted in a STL (Standard Triangle Language) file to obtain “2D slices” that represent the dimension of the layers of the component. The building process begins by adding a thin layer (typically 20-40 μm) of metal powder from the supply platform over a substrate plate in the building chamber by the aid of a re-coater, which distributes the powder on the platform and makes the layer homogeneous. It is important to have spherical powder in order to have a good and homogeneous spread of the powder [3]. After that, a Nd-YAG laser is directed by a scanning mirror, which focuses the laser beam on different points of the powder bed as required from the CAD model by affecting and melting the powder selectively. Finally, the building platform is lowered, and a new layer of powder is added. This step is repeated until the component is complete, and then it must be separated from the substrate, then the process is repeated until the 3D component is complete. Due to the high temperature reached during the process, it is important to have a controlled atmosphere with an inert gas such as argon or nitrogen to avoid the oxidation of the material. The type of gas employed depends on the used material. For instance, for Ni-based superalloys is commonly used argon [1]. The platform is usually preheated at about 80-100 $^{\circ}\text{C}$ to reduce the residual stressed [2].

A schematic representation of the process PBF is shown in Figure 5.

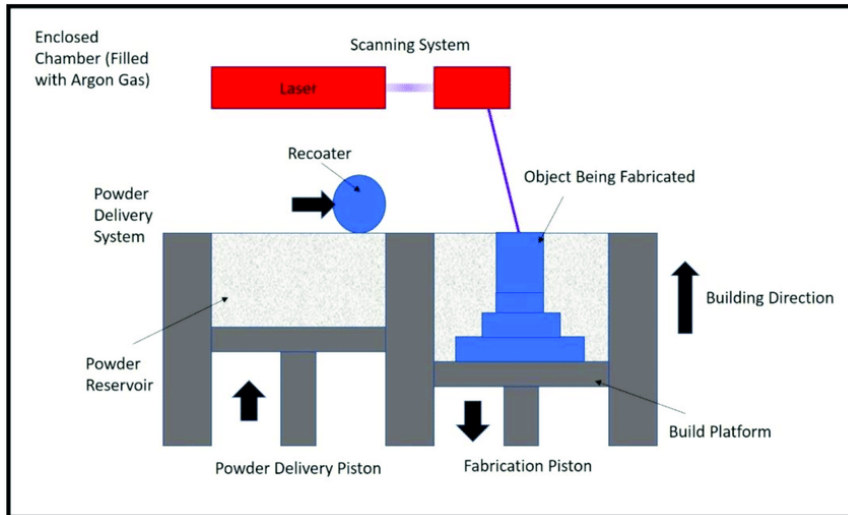


Figure 5: Schematic illustration of the LPBF process [16].

The morphology and size of powders are an important for powder bed fusion processes because they influence powder flowability, laser energy absorption and the thermal conductivity of the powder bed [1]. The powder size depends on the material, for instance, for Inconel powder the typical size is typically in a range from 15 to 63 μm [17]. To obtain lower internal stresses, part distortion, porosity and surface roughness in the built part a higher packing density is necessary, and it can be achieved with a wider distribution of particle size.

To obtain the material with low porosity, process parameters of LPBF must be optimized. The main process parameters include:

- Layer thickness t [mm]: represents the thickness of the powder layer.
- Laser power P [W]: influences the size of the molten pool.
- Scanning speed v [mm/s]: represents the speed of the laser beam.
- Hatching distance h_d [mm]: represents the average distance between two molten pool.
- Scanning strategy: the strategy employed to scan a specific area with the laser beam.

These parameters are usually incorporated in a parameter called Volumetric Energy Density (VED [J/mm^3]):

$$VED = \frac{P}{vh_d t}$$

This parameter defines the energy delivered to the material, and it is one of the most used for the optimization of LPBFed material [18].

If the VED is too low, the material does not receive enough energy, and this could produce balling phenomenon due to the lack of wetting of the molten pool with the previous layer, while if the VED is too high, the temperature of the molten pool increases with the risk of high thermal stresses which may generate microcracks, keyhole formation and melt pool instability, generating the formation of defects.

LPBF process has a high cooling rate (between 10^5 - 10^6 °C/s) which cause a non-equilibrium microstructure with a fine cellular or columnar dendritic microstructure [1], [19]. The refined microstructure is attributed to the high heating and cooling rates that induce superheating and undercooling.

3.3.4.2 Defects in laser powder bed fusion

Additive manufacturing techniques like LPBF are governed from a complex physics that is not fully understood yet. Various defects may occur if the process parameters are not optimal or the feedstock material and build chamber are inadequate.

The common defects include porosity, cracking, delamination, poor surface quality, balling, distortion, which compromise the properties of the material [2]. The morphology and size of metal powders are crucial to obtain a high-quality of the 3D component because they affect the powder bed smoothness and flowability. Defects are also produced by gas residual contained in the gas atomized powders [20].

A brief explanation of the main defects is reported in the following list:

- Porosity: pores are one of the most common defects in 3D printed parts and are known to be detrimental to the material in that they act as crack initiation sites, reducing toughness and fatigue strength. Pores usually are small, with a size less than 100 μm and may develop because of un-optimized process parameters, like keyhole (too high energy) or with fine dimensions (around few microns) from the residual gas inside the particles. This occurs because of the rapid solidification of the melt pool that inhibits the gas bubbles to rise and escape, remaining trapped in lower regions. Pores may also form when metal powders with a hollow structure are utilised in the process [21]. To alleviate or eliminate pores, aside controlling process parameters, post processing such as hot-isostatic pressing (HIP) can be applied [2]. An example of porosity is shown in Figure 6.

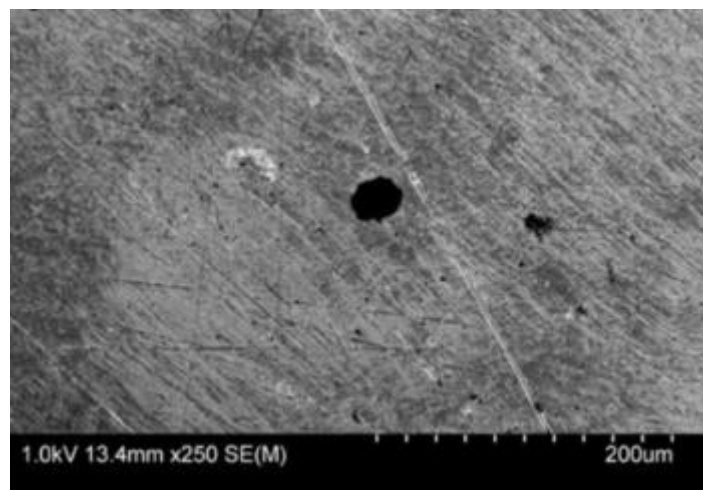


Figure 6: SEM image of 316L produced by LPBF showing large pores [2].

- Lack of fusion: these defects occur when the energy delivered to the material during the melting process is insufficient so that the layer is not completely fused and the new

layer may not deposit in the previous layer with a sufficient overlap [2], [21]. In fact, if the laser energy is too low, the width of the molten pool is small, causing an insufficient overlap between the scan tracks, and the un-melted powder may form between them. These particles are difficult to be re-melted after the deposition of the new layer and, as a consequence, incomplete fusion holes are formed and remains in the fabricated part [21]. Lacks of fusion are easily visible OM images because irregular-shaped pores are formed between the interface of adjacent layers [2]. Lack of fusion may contain un-melted particles. An example of lack of fusion is shown in Figure 7.

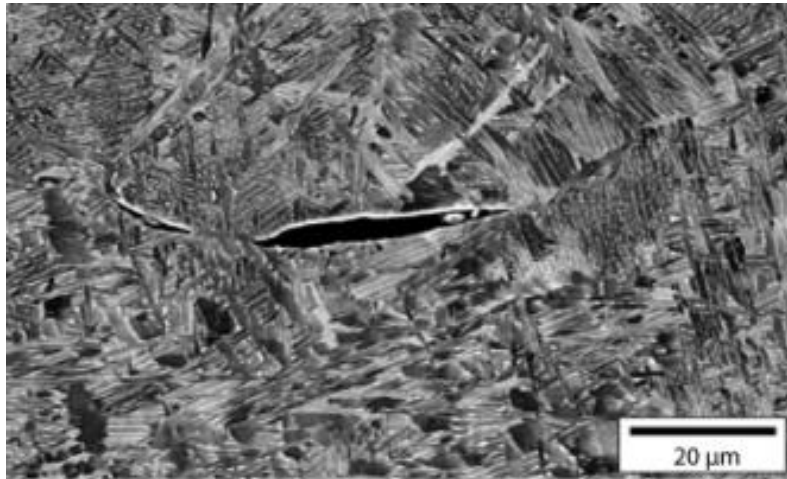


Figure 7: SEM image of 316L produced by LPBF showing a lack of fusion between layer [2].

- Residual stresses and cracking: cracking in LPBF techniques is due to thermal residual stresses generated by the high temperature gradient and fast solidification rate of the melt pool. It occurs especially when the energy delivered to the material is relatively high because the temperature reached by the material is higher, with the possibility to yield high thermal residual stresses, so preheating of the building chamber is crucial to truncate the local thermal gradient. If the residual stresses within the material exceed the local yield stress of the alloy, plastic deformations may occur, while if the residual stress is higher than the local ultimate tensile strength, cracking may appear. Cracks may nucleate also from un-melted particles and pores, and this underlines the importance of process parameters optimization. Material with a low thermal conductivity and high thermal expansion such as stainless steels and Inconel are more susceptible to cracking during the printing process. Two different kinds of cracking can occur: solidification cracking, that occurs when the molten pool presents too much energy and stresses are induced between solidified and un-melted areas of the melt pool, and it has a strong dependence on the solidification nature of the material (dendritic, cellular or planar) and on the melt pool viscosity; grain boundaries cracking, that occurs in the grain boundaries and it is typically caused by the formation of precipitate phases. Thermal stresses can be reduced by various techniques such as process parameters optimization, preheating the substrate to reduce the thermal gradient, using monitoring devices included thermal imaging systems and material composition. Materials like some superalloys and intermetallic are more susceptible to crack formation [2]. An example of cracking is shown in Figure 8.

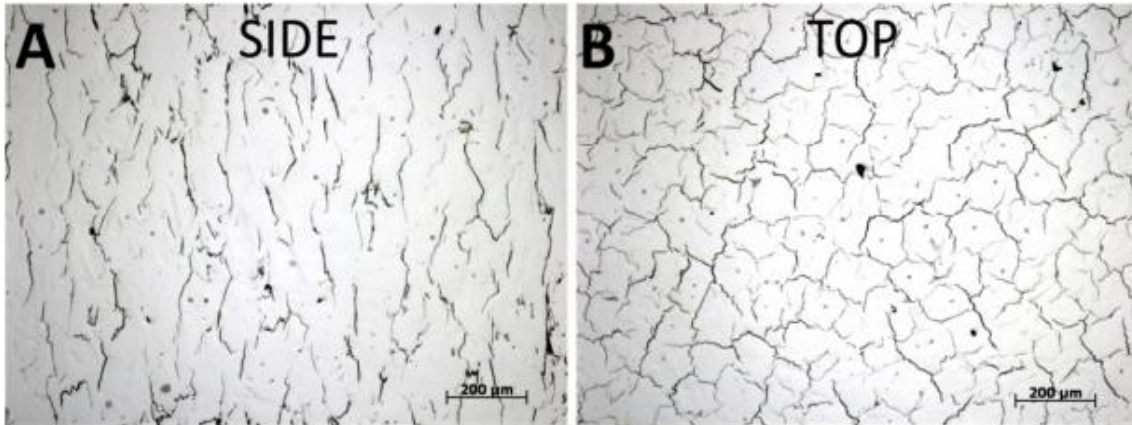


Figure 8: Cracking in Hastelloy C-276 produced by LPBF [22]

3.3.4.3 Melt pools

The melt pools form during the LPBF process, and the physics are quite complex and crucial to the final quality of the formed part. The characteristics of the melt pool are governed by various physical phenomena such as ablation pressure, vapor plume effect, surface tension, gravity, Marangoni turbulence, recoil pressure, etc. The melt pool can form in two different modes: conduction mode, that locally melts the material to form a molten pool and it occurs as a shallow and wide ellipse mitigating defects; key mode, that occurs when the energy density is sufficiently high forming a deep narrow pool where the metal evaporates generating a recoil pressure and a capillarity called keyhole.

The optimization of process parameters of LPBF process is quite important because they affect the size and depth of the keyhole generated and an eventually collapse may form porosity and other defects. The rapid solidification impedes vapor bubbles from leaving the melt pool which can create a keyhole pore within the part. It was noticed that Marangoni turbulence and recoil pressure are the main causes of the melt pool flow instability, in fact, the Marangoni turbulence occurs when un-melted particles are in contact with the melt pool, causing surface tension which pulls the fluid at the surface toward the colder region and so pores and gaps may appear, instead recoil pressure is due to the evaporation in the keyhole generating a vapor jet and a subsequent fluid flow in the keyhole and melt pool.

The pressure within the molten material can easily increase because the extremely high temperatures generated by the heat source, higher than the evaporation range of some chemical elements within the material. Due to the vaporization of the metal the recoil pressure is applied on the melt pool with a resulting high velocity vapor plume. If vapor recoil is sufficiently high the vapor plume has enough energy to leave the keyhole with a release of particles by momentum transfer through neighbouring particles called “spatter” which is the ejection of fluid particles from the melt pool and is very common in LPBF techniques. Spatter greatly effects the surface roughness of the 3D component [2], [23], [24].

A schematic mechanism of the melt pools is represented in Figure 9.

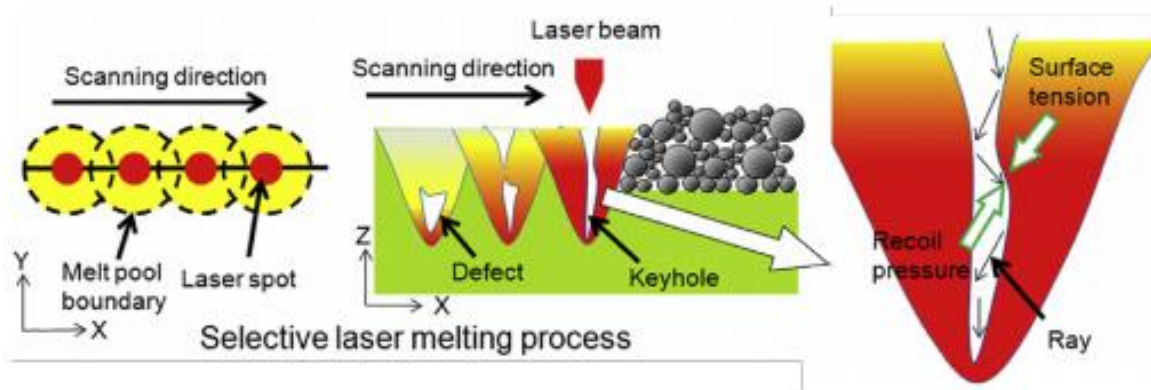


Figure 9: Physical mechanisms associated with melt pool dynamics and keyhole formation [25].

3.4 Additive manufacturing in aerospace applications

AM has radically changed the product design, manufacturing, and assembly in the aerospace industry. These techniques have found wide use since the launching in commerce as a rapid prototyping technique to save capital and time during the development period, but also for rapid tooling, direct part manufacturing and repair in aerospace industry. Various aerospace companies have widely used AM components, for example, Boeing has approximately 300 different part numbers on 10 different aircraft production programs, which amounts to more than 20,000 non-metallic additive manufactured parts that are on vehicles delivered to their customers. about 150 components in the forward fuselage area of the F/A-18 Super Hornet are produced through SLM. This because AM techniques in the aerospace field are suitable to obtain components that satisfy the requirements of materials for aerospace application [1]:

- Complex geometry: aircraft components usually have an integrated function, such as air foils with embedded cooling chamber or an engine turbine blade that may also have an internal structure for coolant. So, the shape of the components may be complex and often defined by mathematic formulae based on fluid flows. These features make conventional computer numerical control machining quite complicated, and for this reason, AM techniques are very suitable for this purpose.
- Difficult to machine materials: most of the materials used in the aerospace application are advanced materials, such as titanium alloys, nickel-based superalloys, cobalt-based superalloys, special steels and ultrahigh-temperature ceramics, which are difficult, costly and time-consuming to machine with traditional techniques, and these issues can be solved with AM techniques.
- Small production runs: AM is not convenient when a large production of components is required, but the advantages of AM are obvious with small production runs because the process does not need design and fabricate fixtures or special tools.
- Low production time: in aerospace field most of the components have very long working life (usually about 30 years), so maintaining and replacing old tooling is a notable inventory cost for manufacturers. AM allows to obtain spare parts and to substitute the old components with them in few weeks with a substantial economic vantage.

- High-performance components: aerospace field requires components with the lowest possible weight with a high strength-to-weight ratio to increase the performance, improve fuel efficiency and reduce emissions. Moreover, some aerospace components work in extreme conditions, such as engine components, which work with ultrahigh temperatures and severe chemical environments, so engines require new components with an innovative cooling solution and with flame-retardant materials. AM allows to obtain tailored parts for this purpose.

Some examples of components produced by AM from aerospace companies are displayed in Figure 10 and Figure 11. GE Aviation produced next generation jet engine components such as the fuel nozzle (Figure 10) via direct metal laser sintering, which is nowadays utilised in GE-Leap engines. This new design has more intricate cooling pathways and support ligaments with the result that it has a service life 5 times higher than the predecessor made by conventional techniques. The number of parts utilised to make the nozzle was reduced from 18 to 1 and the component is 25 % lighter than the previous version [1].



Figure 10: GE Leap Engine fuel nozzle created using laser powder bed fusion via the EOS metal powder bed fusion machine [1].

Avio Aero has successfully developed low pressure turbine blades produced by EBM utilising titanium aluminide (TiAl) for GE Aviation's GE9X jet engine (Figure 11), which powers the Boeing 777X jet. TiAl allows to obtain a 50 % weight reduction than the previous component produced with cast Inconel 718 making this material perfect to this purpose. However, TiAl is very difficult to cast as it is prone to crack, so EBM offers a cost-competitive solution for the fabrication of TiAl [26].



Figure 11: Turbine blades made of TiAl produced via EBM by Avio Aero [26].

4 Superalloys

With the term “superalloys” is defined a high-temperature material, that is a material which has the following features [27]:

- The ability to withstand loadings at an operating temperature close to its melting point so that the ratio $T_{\text{operative}}/T_{\text{melting}}$ is usually greater than 0.6-0.8.
- A substantial resistance to mechanical degradation over extended periods of time, in other words it has a good creep resistance.
- Tolerance of severe operating environments, so it has good corrosion and oxidation resistance.

So, superalloys are particularly suitable for components that have to withstand high mechanical stress at high temperature, such as the combustion chamber and the turbines in a jet engine in that they have the highest specific strength at high temperatures as shown in Figure 12.

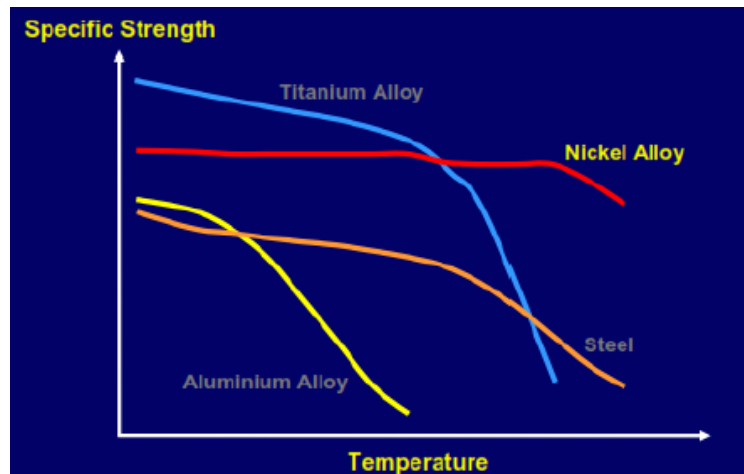


Figure 12: Temperature/specific strength diagram showing the high performance of nickel superalloys at high temperatures [3].

4.1.1 Superalloy categories and composition

Superalloys can be divided in three macro-categories [3], [28] :

- Nickel-based superalloys: contain 50-75 wt. % Ni.
- Iron-nickel-based superalloys: contain 10-50 wt. % Ni and 15-60 wt. % Fe.
- Cobalt-based superalloys: contain 10-35 wt. % Ni and 30-60 wt.% Co.

Nickel is face-centered cubic (fcc) in the whole range of temperature, and this give it a good ductility. Differently, iron and cobalt have different allotropic phases with temperature also presenting the phases body-centred cubic (bcc) and hexagonal close-packed (hcp):

- Iron is bcc until 910 °C, then is fcc until 1394 °C and finally is bcc until $T_{\text{fus}} = 1538$ °C.
- Cobalt is hcp until 430 °C and then fcc until $T_{\text{fus}} = 1495$ °C.

In these alloys, fcc phase can be stabilized by adding alloy elements, especially nickel to provide the best properties. Superalloys may often contain more than 15 alloy elements [3], and consequently, superalloys have a melting range and not a specific melting temperature. The role of the alloy elements is summarized in the following list [28]:

- Major elements: these are the most common elements that allow to obtain determinate properties. Molybdenum, tantalum, tungsten and rhenium increase strength; chromium and aluminium increase oxidation resistance by promoting the formation of Cr_2O_3 and Al_2O_3 in the external surface of the alloy; titanium increases hot corrosion resistance; nickel increases the phase stability; cobalt increases volume fractions (V_f) of favourable secondary precipitates. Some elements are added to form hardening precipitates like γ' ($\text{Ni}_3(\text{Al},\text{Ti})$) by adding aluminium and titanium, and γ'' (Ni_3Nb) by adding niobium.
- Minor elements: carbon and boron are added to form carbides and borides, which with magnesium are added for the purpose of tramp-element control; boron, zirconium and hafnium are added to promote grain-boundary effect and to improve precipitation and carbide formation; lanthanum is added to improve oxidation resistance and yttrium is useful to coatings and to enhance coating life.
- Rare earth elements: most modern superalloys contain elements like yttrium and cerium at a concentration of 2.5-6 % due to their feature of increased high-temperature creep resistance by precipitation and solid solution hardening. The problem with these materials is that they cause casting defects, so ruthenium is used in combination with rare earth metals to achieve high-temperature improvements of mechanical properties. Platinum, iridium, rhodium and palladium may be used for this purpose but are more expensive. To promote higher elevated temperature and stress rupture properties submicrometric oxide particles, such as ThO_2 and Y_2O_3 may be used [29].

It is important to find the right content of each element, as some elements like cobalt, molybdenum, tungsten, rhenium, and chromium may participate in the formation of undesirable tcp phases. There are also detrimental tramp elements: silicon, phosphorus, sulphur, lead, bismuth, selenium, tellurium, and silver which are known to decrease property-level in superalloys.

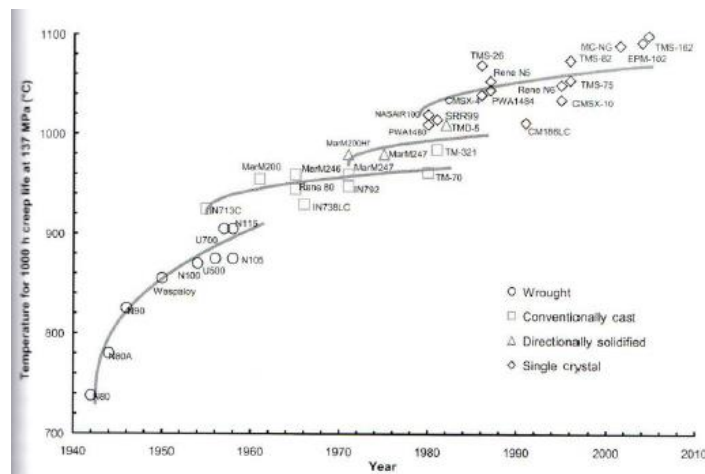


Figure 13: Historical development of superalloys [3].

Superalloys have undergone a historical development [3] and in recent years they have higher operative temperatures than past as shown in Figure 13. Firsts, superalloys were obtained by means of wrought process. To improve the creep resistance, at the end of 1950s cast alloys have been obtained, which present coarser grains and a higher operative temperature. Then, a directional solidification was applied to superalloys to obtain columnar grains and superior performance and better creep resistance at high temperatures. Finally, it was possible to obtain a single crystal structure which presents the highest operative temperatures.

4.1.2 Microstructure

Especially for iron-nickel-base and nickel-base superalloys, microstructure evolution has been more pronounced. In the list below a summary of the phases that can be found in a nickel-base wrought superalloy is presented [28]:

- γ matrix: is a fcc nickel-base nonmagnetic phase that usually contains other elements in solid-solution such as aluminium, tungsten, molybdenum, chromium, etc.
- γ' : is the main reinforcing phase of superalloys and is an intermetallic compound formed from aluminium and titanium ($\text{Ni}_3(\text{Al,Ti})$), which reacts with the nickel to form a phase coherent with the γ matrix. Also, niobium, tantalum, and chromium enter γ' . These precipitates have an excellent long-term stability, providing the superalloy a good creep resistance at high temperatures, but a high volume of γ' is needed to provide the material good strength and fatigue resistance. The precipitates form during heat treatment processes that involve solution and ageing treatments. The temperature and time of the ageing treatment depend on the application of the superalloy. Lower ageing temperatures and shorter time produce fine γ' precipitates that give to the material high strength and fatigue resistance (such as turbine discs), while with higher temperatures coarser γ' precipitates form and are indicated for components which need high creep and stress rupture resistance (such as turbine blades) [29]. To avoid any evolution of the microstructure, the components are usually water quenched after the heat treatments. γ' usually precipitates in spheroidal particles, but cuboidal precipitates were found in alloys with high titanium and aluminium content.
- γ'' : it forms in presence of iron from combination of nickel and niobium or vanadium forming a body-centered tetragonal (bct) Ni_3Nb or Ni_3V . This phase improves the strength of the alloy in low and medium temperatures, but it is metastable and tend to transform into delta phases for prolonged thermal exposures over 600-650 °C. This phase is the main strengthening phase for Inconel 718 and Inconel 625.
- Carbides: they form in the presence of carbon in the amount of 0.02 to 0.2 wt. %, which combine with reactive metals such as titanium, hafnium, tantalum, and niobium. Carbides are important in alloys that are not in single crystal state because are usually deposited in grain boundaries, but they can appear also into the matrix. In fact, carbides have three main functions: firstly, carbides in grain boundaries reinforce the alloy preventing or retarding grain-boundary sliding and permitting stress relaxation; secondly, fine carbides in the matrix have a reinforcement role too; finally, carbides tie up some elements that may cause phase instability. However, too many carbides may decrease the ductility, welding and fatigue resistance of the alloy. Various kinds of carbides exist, depending on composition and processing of the alloy. The most

important are MC, M₆C and M₂₃C₆ where M is a metal. Their formation depends on temperature and they have a different shape.

- Borides: low and hard density particles than may form when boron segregates in grain boundaries. Borides were found in different phases (M₃B₂ and MB₁₂), blocky to half-moon in appearance and are useful for creep-rupture properties.
- η (hcp Ni₃Ti): this phase can be observed in superalloys with a high titanium/aluminium ratio. It can be found in intergranular place as a cellular form or intragranularly as acicular platelets in Widmanstätten pattern.
- δ (orthorhombic Ni₃Nb): is an intermetallic phase that forms with an acicular shape between 815 and 980 °C, but also at lower temperature in case of prolonged heat treatments [30]. It forms by cellular reaction at low aging temperatures and by intragranular precipitation at high aging temperatures. δ has an incoherent phase and does not reinforce the material when is present in large quantities. However, it is reported that a small content of δ can control and refine the grain size with an improvement of mechanical properties and creep-behaviour [28].
- MN: nitrides are observed in alloys that contain titanium, niobium or zirconium. Nitrides have a square or rectangular shape and are insoluble at temperatures below the melting point.
- μ : has a rhombohedral crystal structure and it can be observed in alloys with high contents of molybdenum and tungsten. It is a A₇B₆ intermetallic, it forms at high temperatures and can be found as coarse, irregular Widmanstätten platelets.
- Laves phases: it has a hexagonal crystal structure and usually appears as irregularly shaped globules, elongated, or as platelets after extended high-temperature exposure. Laves phases have the A₂B general formula and they usually are Fe₂Mo, Fe₂Mo, Co₂Ta and Ni₂Nb, but in superalloys they assume a more complex composition such as (Fe,Ni,Cr,Mi,Si)₂(Mo,Ti,Nb).
- σ : has a tetragonal crystal structure and forms after an extended exposure to temperature between 540 and 980 °C. It presents the intermetallic composition A_xB_y, where x and y vary from 1 to 7, and it usually appears in alloys with high content of chromium and molybdenum (Cr,Mo)_x(Ni,Co)_y. It can be found as irregularly shaped globules, often elongated.

4.2 Superalloys in aerospace applications

4.2.1 Introduction

Superalloys had a key role in the development of high-thrust engines since the end of the Second World War, when there were the rapid rise of jet-powered civil aviation and rocketry. The main improvement in the thrust of jet engine is due to the increase of the operating temperature that is limited by the heat resistance of the materials. Superalloys also increased the durability of components so that a modern Boeing 747 engine can operate for more than 20 000 hours. Especially nickel-based superalloys are widely used in aerospace applications because of their long resistance to high temperatures (800-1000 °C), so are suitable for jet engines where superalloys are the main materials (over than 50 %) and are used in the hottest component such as high-pressure turbine blades, discs, vanes, combustion chamber, afterburners and thrust reverser, but are widely used also in low-pressure turbine case, shafts and burner cans This

because superalloys present some properties required from a gas turbine material: high strength, long life fatigue, fracture toughness, creep resistance and stress-rupture resistance at high temperatures. Besides, superalloys present an excellent oxidation and corrosion resistance so that they can be used in severe environments. The main problem of superalloys is the high density of the materials (usually 8-9 g/cm³), so lighter materials could be used to reduce the weight of the engine, such as titanium alloys or the intermetallic TiAl which present about half density and are used in components where temperature is not excessively high such as low-pressure turbine [29]. However, the main weakness of the intermetallic TiAl is its brittleness, and for this reason superalloys are still preferred.

4.2.2 Jet engine materials

Materials used in a jet engine must withstand extreme conditions such as high stress and a highly corrosive environment. Materials in the hottest section of the engine require excellent properties at high temperature:

- High yield stress and ultimate strength to prevent yield and failure.
- High ductility and fracture toughness to provide impact resistance and damage tolerance.
- High resistance to fatigue cracks to provide long operating life.
- High creep resistance and stress rupture strength.
- Resistance against hot corrosive gases and oxidation.
- Low thermal expansion to maintain close tolerances between rotating parts.

A schematic of a turbofan jet engine is presented in Figure 14.

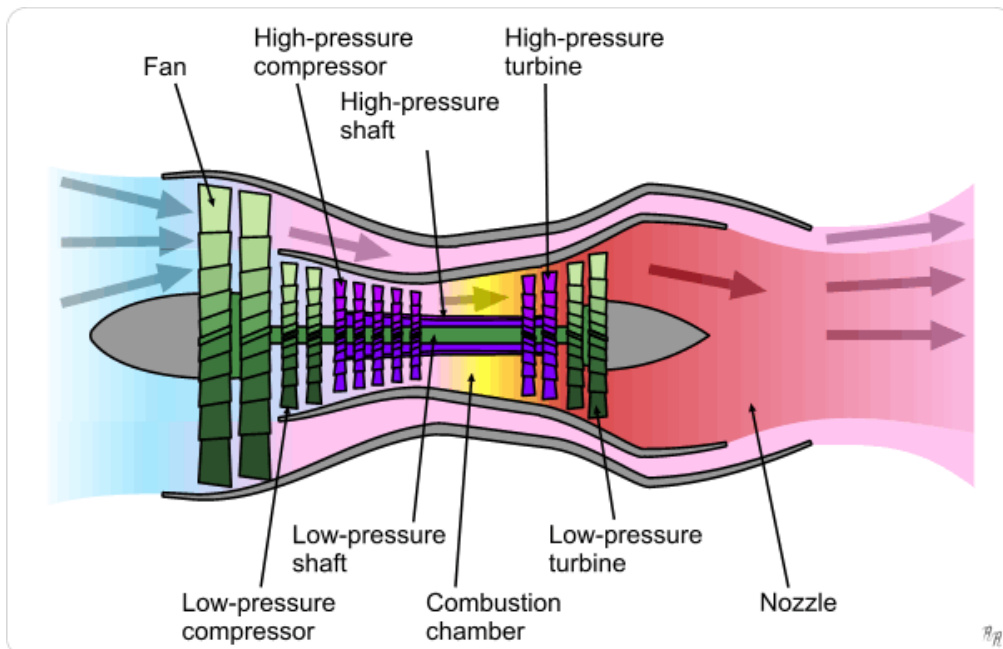


Figure 14: Turbofan schematic [31].

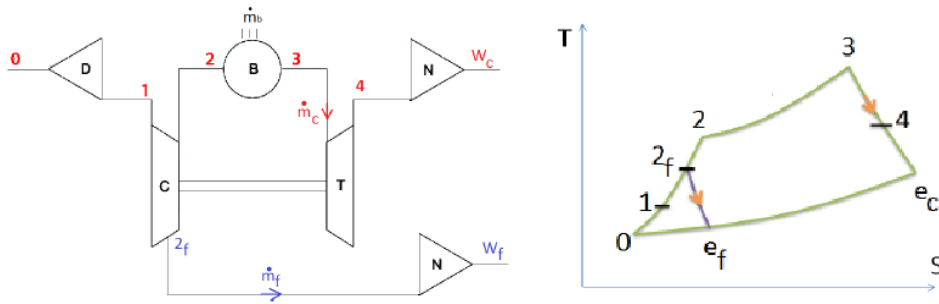


Figure 15: Simplified schematic and thermodynamic cycle of a separated-flow turbofan [32].

Figure 15 represents the schematic of a separated-flow turbofan and the Joule-Brayton thermodynamic cycle:

- 0-1: air intake. The aim of the intake is to act as interface between the external environment and the first component of the engine.
- 1-2: compressors. There are two compressors: a low-pressure compressor (LPC) which include a fan where both the cold and the hot flows are compressed, and a booster that represents the final part of the LPC where only the hot flow is compressed (section 1-2_f), and a high-pressure compressor (HPC) where the hot flow coming from the booster is further compressed (section 2-2). The fan is made of large blades with the aim to have a high by-pass ratio (BPR) and are subjected to strong centrifugal forces, so fan blades are made by light and high-specific strength materials such as titanium, aluminium and stainless steel, but titanium alloys present the highest strength to weight ratio, corrosion resistance and creep resistance, and are widely used. Instead, due to the compressing air, the temperature of the flow rises in the compressors, so Fe-, Ni-, and Ti-based alloys are used for the purpose. Boosters, where temperature is lower are usually made of titanium alloys like Ti-6Al-4V (used also in fan blades), while HPC requires a better resistance to higher temperature, and so Nickel-based superalloys such as Hastelloy X are used, but in recent years modern titanium alloys are replacing nickel superalloys in order to reduce the weight of the engine [33].
- 2-3: combustion chamber. The hot flow enters in the combustion chamber and here is mixed with the fuel. The mixture is ignited, and the temperature rises at constant pressure up to the Turbine Inlet Temperature (TIT) that is usually higher than 1000-1200 °C, and which strongly depends on the materials resistance of the turbine blades. For this purpose, combustors are made of Ni- or Co- based alloys with several additives to improve the superalloy properties, such as aluminium and titanium for strength, chromium for corrosion resistance, molybdenum, tungsten and rhenium for high-strength resistance. To increase the operating temperature of the combustion chamber, a thermal barrier coating which consists of a thin ceramic film (usually ZrO₂ or Y₂O₃) that is used to cover the walls of the combustion chamber in order to reduce heat flow into the superalloy. One of the most used material in this section is Hastelloy X [29].
- 3-4: turbines. The mixture gases from the combustion chamber are then expanded first in a high-pressure turbine (HPT) and then in a low-pressure turbine (LPT). Turbine blades are moved from the flow, and rotation is transmitted to the shaft and consequently to the compressor. Turbines, especially HPT, are the most critical component in terms of temperature and pressure, so the material must present different

requirements, such as high creep strength, high temperature fatigue strength, and high corrosion resistance. Ni-based alloys are used for this purpose, and for the first stages of the HPT, where temperatures are excessively high, cooling passages design and thermal barrier coating of ZrO_2 can be used to improve turbine blades performances. Typical Ni-based superalloys for turbine discs are Rene 95 and Discaloy, while for turbine blades Nimonic, PWA1480 and PWA1422 are widely used [33]. For LPT, where temperatures are lower, the intermetallic TiAl could be used to reduce the weight of the engine.

- 4-e: exhaust and nozzle. The exhaust system is the part in the rear of the engine which aims to transfer the exhaust gases coming from the last stage of the turbine to the nozzle. It includes various component, but the main ones are shown in Figure 16. The tail cone (or exhaust cone) has a diverging shape which aims to reduce the velocity of the gases coming from the turbine in order to reducing the friction losses. It also protects the engine against the gases getting back into it. The tail pipe (exhaust pipe or jet pipe) is the section which is connected with the nozzle, and it must be as short and large as possible to reduce the friction losses. The gases in this section have a temperature between 550 °C and 850 °C. Finally, the nozzle has a convergent shape and aims to increase the velocity of the gases in order to produce the thrust. In the exhaust system passes the exhaust gases, so it requires materials that must be durable, hard-wearing, and resistant to high temperatures and corrosion. In particular, Inconel 625 can be used in tailpipes, vector nozzles, bellows and hush kits, among other primary components [34].

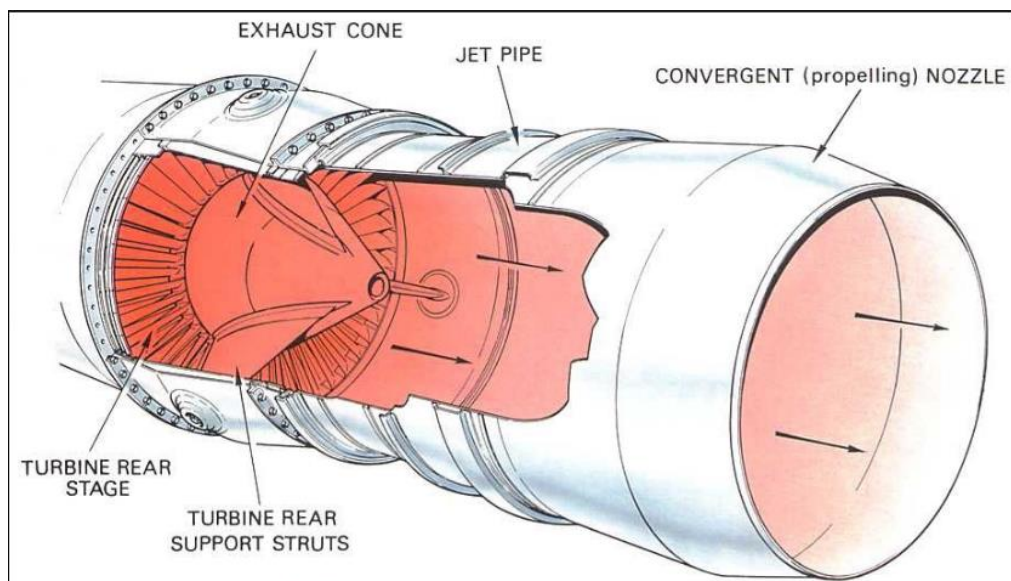


Figure 16: Exhaust system schematic [35].

So, the materials used in the various components inside a jet engine are strongly depended on the temperature and the mechanical stresses that they have to withstand. In Figure 17 are shown the typical temperature and pressure profiles inside a jet engine.

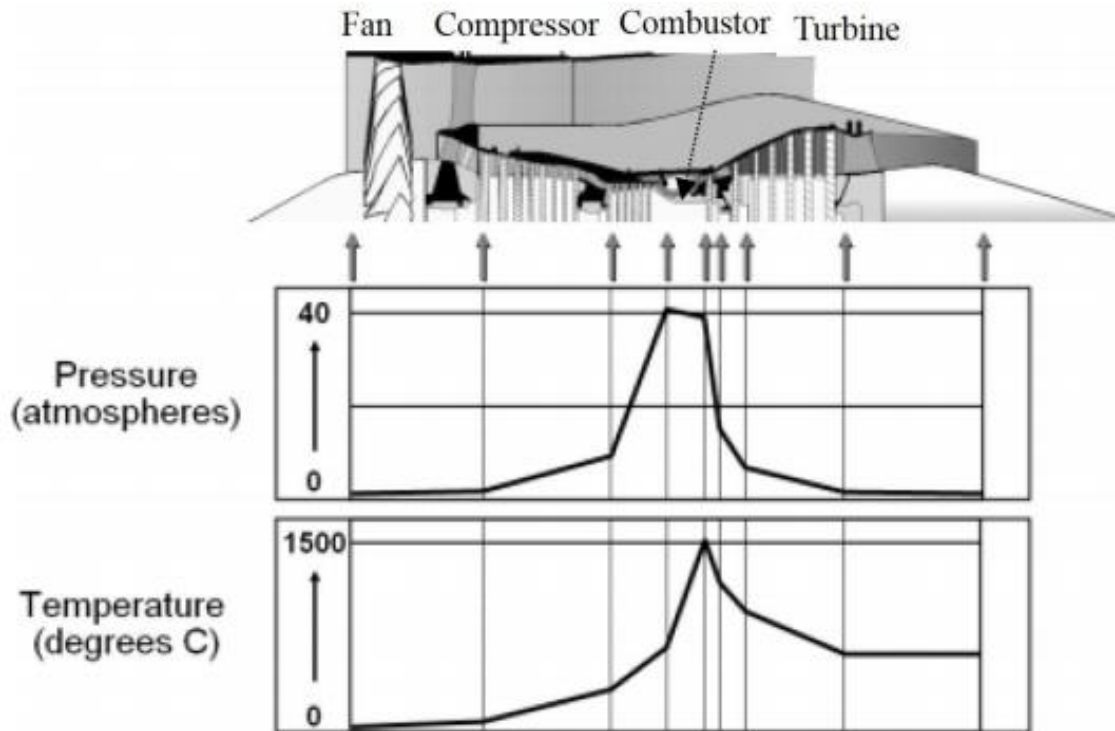


Figure 17: Temperature and pressure profiles of an aircraft engine [33].

4.3 Superalloys for LPBF

Because of the difficulties to machine the superalloys with traditional techniques, Additive Manufacturing like LPBF process can be a solution especially for complex-shape components. A limited range of superalloys are suitable for LPBF, but in general weldability should be taken in consideration, since a high weldability is associated with low defect susceptibility [36]. The weldability strongly depends on the alloy composition. It was found that the weldability of Ni-based superalloys is sensitive to Al and Ti elements, in fact, if the content of Al and Ti exceeds 5 % inside the superalloy, it can become non-weldable because of the formation of high fraction of γ' and TCP phases. Cr elements have also a key role in weldability as superalloys with a concentration between 16 and 30 % at present a good weldability, but a higher concentration cause the formation of harmful σ phases, reducing the mechanical properties [36].

The main difference between a wrought alloy and an alloy produced by LPBF is the epitaxial growth of grains along the building direction due to the high solidification rate ($10^5/10^6$ K/s) which leads to a very fine dendritic microstructure [13], [37]. This results in a different microstructure evolution and mechanical properties under heat treatments with respect to the traditional processed superalloys. Figure 18 shows the typical texture of the Ni-based superalloys with elongated grains along the building direction.



Figure 18: Electron backscatter diffraction (EBSD) scan of an Inconel 718 sample produced by LPBF. It can be noticed that grains are elongated through the building direction (z axis) while are irregular in the plane x-y [37].

The main superalloys treated by LPBF are:

- Hastelloy X [38];
- Inconel 625, 718, 939, 738LC [18], [39]–[41];
- Haynes 282 [42];
- CM247LC [43].

This thesis focuses on an Inconel 625 matrix, so it will be described in detail in the next paragraph.

4.4 Inconel 625 (IN625)

4.4.1 Wrought Inconel 625

Inconel 625 (UNS N06625) was invented in 1950 and was commercialized for the first time in 1962 [44]. It is a nickel-based alloy strengthened mainly for solid solution by the addition of chromium, molybdenum, and niobium [45]. The major application of the alloy is in the aeronautics, aerospace, marine, nuclear, chemical and petrochemical industries [13]. The chemical composition of the Inconel 625 produced by EOS GmbH is shown in Table 1. The alloy is used for service temperatures from cryogenic to 650 °C under large stress, but it is possible to use it up to 982 °C for its oxidation and corrosion resistances if high mechanical performances are not required [46]. It is appreciated for a combination of high yield strength, tensile strength, creep strength, fatigue and thermal fatigue strength, excellent fabricability, weldability, and good corrosion resistance at high temperatures and for prolonged exposure to an aggressive environment [47] which make the material quite suitable for aerospace application, especially in the exhaust system and ducting system of the engines, but also in thrust-reverser systems, resistance welded honeycomb structures for housing engine controls,

fuel and hydraulic line tubing, turbine shroud rings, spray bars, bellows, and heat-exchanger tubing in environmental control systems [34], [46]. Inconel 625 also maintains good tensile strength, ductility, impact and toughness properties at cryogenic temperatures [48]. The presence of chromium at high concentration and aluminium are responsible for its excellent resistance to oxidation and corrosion thanks to the formation of an oxide layer of Al_2O_3 and Cr_2O_3 , while niobium and molybdenum improve the resistance to reducing acids and have a key role on the strengthening of the alloy at elevated temperatures. However, high concentration of niobium, molybdenum and silicon promote the precipitation of undesirable Laves phases starting from the grain boundaries where there is a high concentration of carbides. These particles are hexagonal close packed A_2B compounds that may contain impurity elements and decrease the strength and resistance of the alloy if are present in large quantities, but Laves phases can be eliminated by solution annealing at high temperatures [49]. Then, high concentration of carbon is responsible of the precipitation of niobium carbides NbC. NbC are not as disadvantageous as Laves phases, but are difficult to remove after their precipitation because they present a higher melting point than Laves phases [49]. The carbides can be liquefied with heat treatments at a temperature over to 1190-1205 °C that coincide with the eutectic (Figure 19). The resultant liquid is highly concentrated in niobium and molybdenum, forming a solid solution very rich of these elements during cooling, so an acicular shape δ phase can precipitate if the alloy is subsequently heat treated at 870 °C [49]. Moreover, the T-T-T diagram shows that various types of carbides aside NbC can precipitate after few minutes with thermal treatments. At higher temperatures, roughly between 870 and 1038 °C M_6C carbides, where M is nickel, chromium and molybdenum, are present, while at lower temperatures (between 704 and 871 °C) $M_{23}C$ carbides precipitate where M is almost entirely chromium. The precipitation of carbides in grains boundary seems to be sensitive to the silicon contents as well as the carbon content [49], in fact it was noticed that with a low concentration of carbonium (below 0.15 %), the silicon retarded the formation of carbides, while it seems that the silicon has no effect with high concentration of carbonium.

Table 1: Chemical composition of Inconel 625 in wt. % (EOS GmbH) [50]

	Cr	Mo	Nb	Fe	Ti	Al	Co
Min	20.00	8.00	3.15	-	-	-	-
Max	23.00	10.00	4.15	5.00	0.40	0.40	1.00

	Si	Mn	C	Ta	P	S	Ni
Min	-	-	-	-	-	-	58.00
Max	0.50	0.50	0.10	0.005	0.015	0.015	Bal.

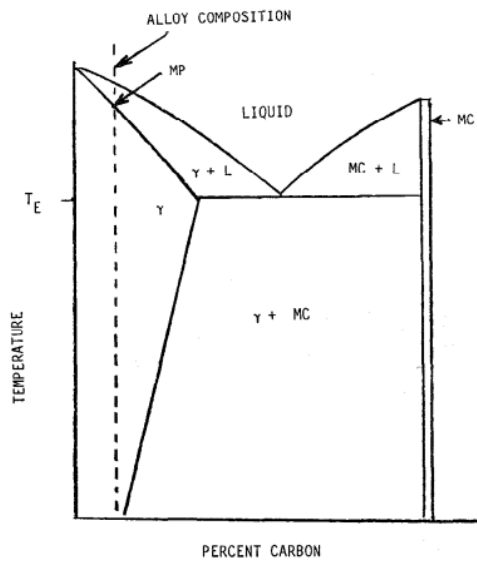


Figure 19: Pseudo phase diagram M-C. The eutectic point is at 1190-1205 °C [49].

ASTM designed two grades of the alloys based on the main areas of application [48]:

- Grade 1 materials is intended as “annealed”. It presents good resistance to aqueous corrosion, good resistance to slightly high temperature (service temperature up to 593 °C) and exhibits a fine grain structure [48].
- Grade 2 materials is intended as “solution annealed” and is used for service temperatures over 593 °C for its high strength and resistance to creep, rupture and corrosion at high temperatures [48].

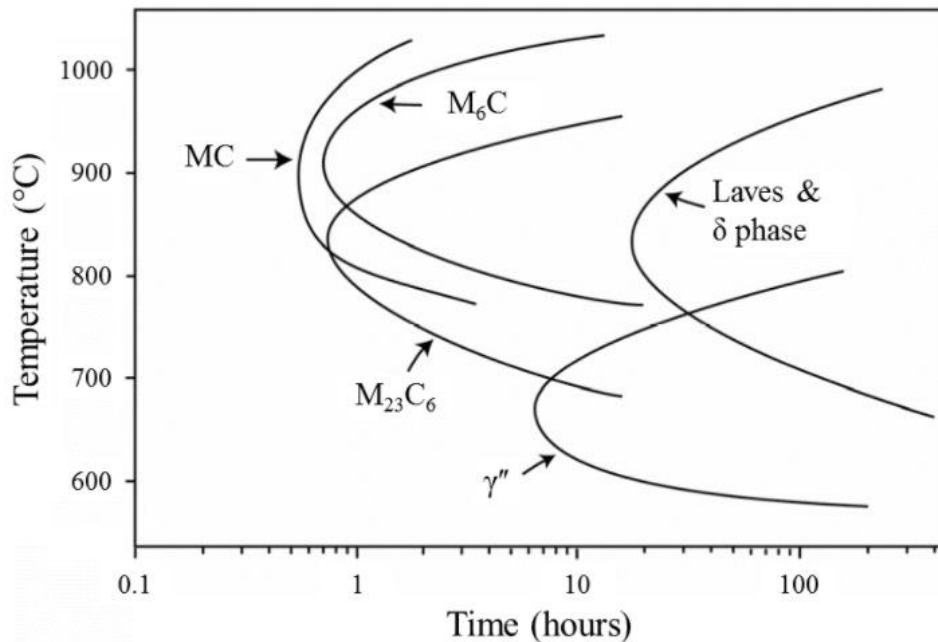


Figure 20: T-T-T diagram for solution annealed, wrought alloy 625 [51].

IN625 was initially designed as a solid solution hardened alloy, but it can be reinforced by the precipitation of intermetallic phases and carbides under heat treatments. In fact, because of the presence of niobium at a concentration of about 4 % a fine γ'' Ni_3Nb can precipitate if the alloy is heated between 649 and 871 °C. Various types of carbides can also precipitate especially in the grain boundaries [48]. The time-temperature-transformation diagram (T-T-T diagram) of Inconel 625 summarizes the phases that can precipitate under thermal exposures, as displayed in Figure 20.

4.4.2 Evolution of Inconel 625

To improve the properties of IN625 different variations of the alloy were developed as shown in Figure 21. The most important is Inconel 718, which is an age-hardenable alloy thanks to the high content of aluminium, titanium, and niobium that leads to precipitation of gamma prime γ' $\text{Ni}_3(\text{Al,Ti})$ phase and the metastable gamma double prime γ'' Ni_3Nb phase. Inconel 718 was further modified, obtaining an age-hardenable alloy called alloy 706 used for large turbine wheels thanks to its high strength, good machinability, and capability of being stress-rupture notch ductile in large cross-section [44]. Some turbine manufacturers added a high percentage of cobalt to increase the service temperature obtaining Rene 220 from GE and PWA 1472 from Pratt & Whitney. Over the years, there was the need to improve the sour gas resistance at high temperatures especially in petrochemical field because of the increasing depth of oil and gas wells, so some high-corrosion resistance alloys such as Inconel 725 developed by Inco Research and Development Center in Suffern, NY, and the Inconel 625 Plus developed separately by Cartech which are strengthened by precipitation of γ' and γ'' phases during aging [44]. Alloy 725 exhibits essentially the same composition of alloy 625 with the difference that contains a major concentration of titanium (around 1.5 wt. %) to enhance precipitation hardening, and iron (around 15 %) [52]. With these concentrations alloy 725 presents the excellent strength properties close to the Inconel 718 in combination with the good corrosion and oxidation resistance of Inconel 625 [48].

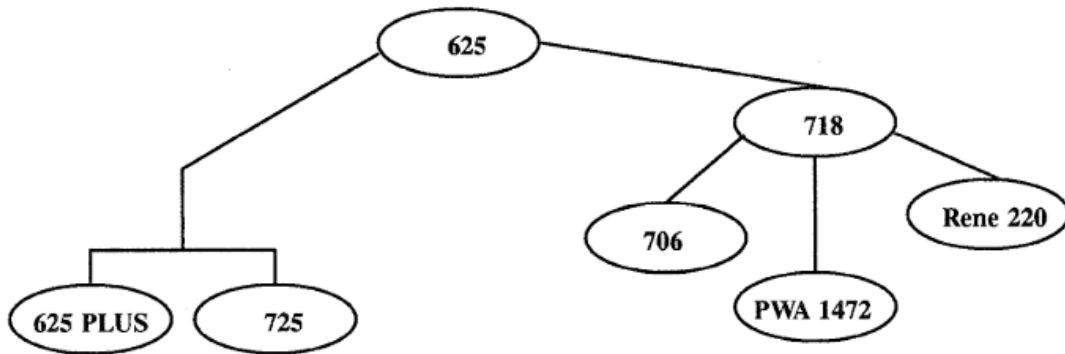


Figure 21: Derivates of alloy 625 [44]

4.4.3 LPBFed Inconel 625

Because of the high weldability of the Inconel 625, this alloy is widely employed in LPBF process. Properties of the LPBFed superalloys are different from wrought IN625. Tensile properties can be superior in as-built LPBFed alloy than the minimum typical value of the wrought IN625 alloy in the same condition, due to the fine dendritic structure mainly below 1

μm with high dislocation density and possible formation of MC carbides [13], [53]. The fine dendritic structure can be explained with the extremely fast solidification rate ($10^5/10^6$ K/s) involved on this process which have also a key role in the suppression of formation or macro segregation of large Laves phases or large carbides that could be detrimental to the mechanical properties of the alloy [13]. However, the high solidification rate causes high thermal stresses and nonequilibrium microstructure in the as-built components, and therefore, post heat treatments such as solutioning, ageing, hot-isostatic pressing (HIP) or a combination of them must be performed to obtain specific properties to match industrial requirements. In fact, different thermal treatments are made to reduce thermal stresses, to eliminate segregation of element, and to obtain a specific microstructure and mechanic properties suitable for different conditions [13], [37].

In Table 2 are shown some typical values of the tensile properties for a wrought and LPBFed Inconel 625.

Table 2: Tensile properties at room temperature for wrought Inconel 625 and samples manufactured by LPBF method

Samples	Ultimate tensile strength [MPa]	Yield strength (0.2 % offset) [MPa]	Elongation [%]
Horizontal direction	980 ± 5	720 ± 5	33 ± 2
Vertical direction	870 ± 10	630 ± 5	48 ± 2
Wrought IN625 – minimum typical value (special metals)	827	414	30

4.5 Metal matrix composite (MMC)

4.5.1 General overview

Innovations in the aerospace field, especially in jet and rocket engines which performance depends on the temperatures reached, are strongly related to the materials improvement so, high performance nickel-based superalloys are in increasing demand. To improve the high-temperature performance, a large number of Ni-based superalloys are precipitation hardened by the addition of titanium and/or aluminium which form the γ' precipitates. In fact, it is known that an increasing content of Ti al Al is suitable for the precipitation of γ' with an improvement of the high temperature properties, such as Inconel 939 and CM247LC alloys. However, there is also an increasing of the susceptibility to strain age cracking and a decreasing in ductility [54].

Another possible strategy is the addition of ceramic particles in the alloy to form a metal matrix composite (MMC) utilizing a solid solution strengthened nickel alloy as the matrix, improving the high-temperature mechanical properties. MMCs hold a good potential to obtain a benefit in specific strength and stiffness [54]. MMCs are very useful engineering materials as they combine the advantages of a ductile metal matrix and a hard reinforcement. Nickel matrix composites (NMCs) are quite suitable for this purpose in that they have good high-temperature mechanical properties, thermal fatigue resistance, oxidation resistance, and thermal corrosion resistance, and may have a wide application in aircraft engines, pipelines, insulation, pollution control equipment, special seawater equipment, nuclear reactors, and nuclear power equipment [55]. However, it is difficult to obtain a good quality of the NMC with traditional methods, such

as infiltration casting, powder metallurgy, and injection moulding, in fact, the materials obtained with cast methods can present defects like aggregations of ceramic reinforcement and pores. One of the main problems in creating composites is the interfacial bonding ability between the hard reinforcement and the relative ductile metal matrix, which have a strong influence on the properties of the MMC. The use of nano-ceramic particles can provide higher strength and hardness than micrometric ceramic particles, but nanoparticles are prone to agglomeration because of the large Van der Waals attraction between nanoparticles which produce a non-uniform microstructure. Moreover, nanometric powder can represent a danger for human healthy, and for these reasons they are more difficult to manage [55]–[57].

In recent studies, it results that additive manufacturing, and especially LPBF, has a great potential to produce MMCs, with the aim to exploit the advantages of the additive manufacturing techniques described in the previous chapter to obtain complex-shape components, in fact, LPBF was used to produce different ceramic MMC such as aluminium-based, titanium-based and nickel-based composites [58]. Cooper et al. [54] investigated Inconel 625-MMC with three different ceramic particles (Al_2O_3 , SiC with micrometric size and TiC from 0.44 to 1.18 μm) at 5 wt. % content. They found that the addition of titanium carbide to an Inconel 625 matrix is preferable than aluminium oxide and silicon carbide, demonstrating the higher density, an absence of micro cracking and a relevant increase in hardness compared to the other reinforcements. Another potential ceramic reinforcement is TiB_2 . Zhang et al. [59] investigated on $\text{TiB}_2/\text{IN625}$ MMC obtaining exceptional microhardness, but with a high level of porosity.

The work of this thesis focuses on TiC/IN625 MMC with the reinforcement with micrometric dimensions, and it is described in detail in the next paragraph.

4.5.2 TiC/Inconel 625 MMC

Inconel 625 is widely used in the aerospace field for its exceptional corrosion and oxidation resistance. However, it presents a relatively low hardness, wear resistance and mechanical properties to very high temperatures, so the application of Inconel 625 is limited to areas in which corrosion and abrasion are severe, while it cannot be applied for components that requires extreme high mechanical properties at temperature superior to 650 °C. To improve these properties, a ceramic particle, such as titanium carbide (TiC), can be added to the IN625 matrix [58]. TiC is a refractory compound, considered one of the most suitable ceramic material to reinforce a metal matrix thanks to its unique properties such as high melting point (3067 °C), moderate density (4.93 g/cm^3), exceptional hardness (2800-3200 HV), high mechanical strength, high wear resistance, good thermal and electrical conductivity and possess high thermal stability during the metallurgy process [60], [61]. In addition, TiC has high chemical stability, which prevents or reduces adverse reactions that produce harmful products between the TiC particles and the Ni matrix [58]. Meanwhile, nickel is quite suitable for TiC-reinforced because it has high toughness and ductility, high corrosion resistance, and exceptional oxidation resistance at high temperatures. Moreover, TiC particles possess high wettability with nickel liquid, which is beneficial for incorporating TiC reinforcements into Inconel 625 [62]. The addition of TiC particles in the IN625 matrix may be beneficial especially for high-temperature mechanical properties [61], making the material a good candidate to be applied in aerospace field such as in engines that require exceptional properties at high temperatures. However, the

presence of TiC may reduce the corrosion resistance of Inconel 625 MMC, and the reason may be attributed to galvanic coupling of the reinforcement constituent and matrix alloy, the formation of an interfacial phase between the ceramic reinforcement and matrix, and microstructural changes and processing contaminants resulted from the manufacture of the MMC [60].

In recent years, some researchers are studying the TiC/Inconel 625 composite produced by additive manufacturing. However, little attention has been paid to TiC/IN625 with micron-sized particles. Currently, TiC particles are commonly incorporated in the Ni matrix via mechanical mixing process to obtain homogeneous mixture of nickel and TiC. However, the mechanical mixing process would deteriorate the flowability of the nickel powders, impacting the processability and mechanical properties of the materials [63].

Chen et al. [55], [56], [58] conducted an elaborate study about TiC/IN625 nanocomposite with 4-6 wt. % TiC content produced by LPBF. They conducted his experiments with a fixed laser power of 200 W, a layer thickness of 30 μm , a hatching distance of 80 μm and a variable scanning speed to obtain different VED values founding the following results:

- Large cavities and balling are formed at low VED values due to incomplete fusion and some un-melted particles are trapped in cavities and aggregation of TiC particles were found. Increasing the VED large cavities disappear, but small pores are visible while some un-melted TiC particles still appear, however, the higher temperature of the molten pool generates thermal stress during the liquid-solid transition, resulting in microcracks. In LPBF process, Inconel 625 powders are fully melted, while TiC particles are only partially melted because of the higher melting point. This causes an increasing in viscosity and a reduction of the fluidity and wettability of the molten pool which are closely related to the densification of the material during the LPBF process.
- From the microstructure of the optimized material, on the plane y-z results that the addition of nano-TiC particles to the IN625 matrix tends to change the microstructure from cellular dendrites to columnar dendrites. This because the addition of nano-TiC particles may reduce the G/V_s ratio. Columnar dendrites grow epitaxially perpendicular to the molten pool boundary along the direction of the heat flow. A small number of cellular dendrites appear in the overlapping zones at either side of the molten pool due to the higher temperature gradient caused by the remelting. TiC particles are not homogeneously distributed in the matrix and some agglomeration can occur due to the Van der Waals forces. At higher VED dendrites are continuous, the growth is epitaxial, the DAS is lower, and the TiC particles are homogeneously distributed in the matrix. In general, DAS in TiC/IN625 composites is lower than pure IN625 because of the thermal conductivity of TiC particles (23 W/ (m °C)) is higher than IN625 (12 W/ (m °C)), so the TiC particles dissipate heat in the molten pool faster, increasing the cooling rate. Cellular dendrites appear more frequently in high VED sample and it seems that TiC particles tends to refine the cellular structures. It results that MC carbides rich in niobium and Laves phases appear in the inter-dendritic region and in sub-grain boundaries. The TiC particles act as nuclei for heterogeneous nucleation during solidification, which facility the refinement of the crystal structure. Moreover, grain refinement induces many sub-grains boundaries, which hinder the dislocation movement.

- After heat treatments, at high temperature there is a recrystallization of the grain structure, but it seems that the nanocomposite TiC/IN625 has a good thermal stability, and the recrystallization temperature of the composite is much higher (over 1070 °C). So, below this temperature the grain morphology might maintain the original macrostructure after the heat treatment. At high-temperature TiC decompose in Ti and C, and C preferentially reacts with Nb and Ti to form MC carbides. After double ageing treatment, many disc-shaped γ'' phases appear in grain boundaries. The γ' phase is not present in pure IN625, while it could appear in TiC/IN625 nanocomposite because of the higher content of Ti and this may improve the high-temperature properties of the material [55].
- With TEM analysis, it results that TiC/IN625 nanocomposite exhibit finer cellular structures than pure IN625 and the TiC nanometric phase that is uniformly distributed in the grain boundaries which can act as obstacles against grain growth. Dislocation lines are present because of the high solidification rate due to the addition of TiC particles. However, the difference of CTE between TiC and metal matrix causes different thermal deformations during the temperature change, which may lead to residual stresses in the matrix and may cause dislocations if the stresses are higher than the yielding point.
- The microhardness of the TiC/IN625 nanocomposite is higher than IN625, and it increases as the VED increase. This because the TiC particles refine the microstructure, and the hardness is higher as the TiC particles are homogeneously distributed. TiC phases in grain boundaries also have an important role in the grain boundaries strengthening effect.

5 Materials and methods

In this section will be described the details of the materials produced by LPBF, methods and the instruments used to treat and analyse the material. Here are explained the flowability and apparent density, samples production, Archimedes' method, heat treatments, metallographic preparation, samples analysis with optical microscope and SEM, hardness and tensile tests.

5.1 Flowability and apparent density test

The flowability is an important characteristic of the powder for the LPBF process. For the LPBF technique, it is very important to know the powder's degree of distribution during the process. No uniform distribution of powder may produce parts not covered by powder and may create pores within the printed parts. The ability of the powder to flow is a function of interparticle friction, in fact, as interparticle friction increased the flow is slower. Humidity and moisture content influence the flow rate. Wet or moist powders may not flow.

It was adopted a static flow method according to ASTM B213-20 and ASTM B964-16 standards [64], [65]. The ASTM B213-20 standard provides the use of a Hall flowmeter shown in Figure 1, which presents a calibrated funnel with an orifice with a diameter of 2.54 mm. A weighed mass (50.0 g) of metal powder is timed as it flows through the orifice. The test has been taken 3 times. Then is possible to evaluate the Hall flow rate (FR_H):

$$FR_H = \frac{t}{50 \text{ g}}$$

where t is the flow time in seconds.

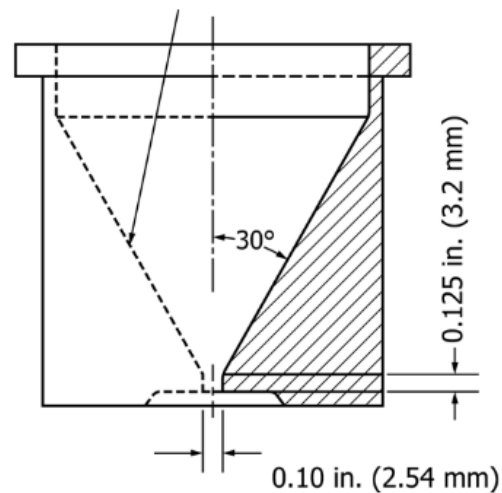


Figure 22: Hall flowmeter funnel [64].

Test method B213 using the Hall funnel is the preferred method for evaluating the flowability of the metal powder, but if the powder does not flow through the funnel is possible to use a Carney funnel according to ASTM B964-16 standard. The component presents an orifice with a diameter of 5.08 mm, as shown in Figure 23. The weighed mass is increased to 150 g for ferrous and copper-based powder. The test has been taken 3 times. Then is possible to evaluate the Carney flow rate (FR_C):

$$FR_c = \frac{t}{150 g}$$

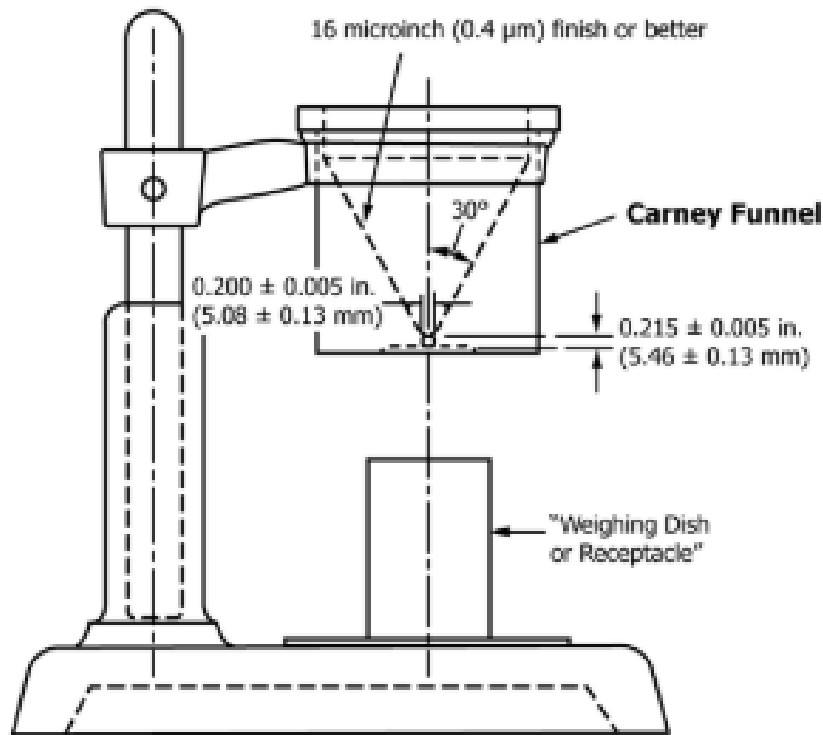


Figure 23: Carney flowmeter funnel [65].

The apparent density is related to the capacity of the powder to fill a fixed volume, so it includes voids contained in the powder. This property influences the performance of the LPBF process. The presence of moisture or oil may alter the physical characteristic of the powder.

The test was done according to ASTM B212-17 standard [66] for free-flowing metal powders using the Hall flowmeter funnel and to ASTM B417-18 standard [67] for non-free-flowing metal powders using the Carney flowmeter funnel. A cylindrical brass cup with a volume of 25 cm³ has been filled with the powder. Then the weight of the powder was measured with an analytical balance. The apparent density was finally calculated:

$$AD = \frac{m}{V}$$

where m is the mass of powder in the density cup in grams and V is the volume of the density cup in cubic centimetres.

The tests of flowability and the apparent density have been carried out for Inconel 625 powder and with different concentrations of TiC.

5.2 Samples production

The Inconel 625 powder used for this thesis was purchased from EOS GmbH which declared composition is reported in Table 3. The powder size is from 20 to 50 μm. The TiC powder is

produced by H.C.Starck, and it has a micrometric size from 1 to 5 μm . The powder of the metal matrix and the reinforcement were mixed by a wander for 48 hours. Two different materials were produced for the purpose:

- Inconel 625 (IN625)
- Inconel 625 + 1 % TiC in weight (IN625 + 1 wt. % TiC).

Table 3: Chemical composition of Inconel 625 in wt. % (EOS GmbH) [50]

	Cr	Mo	Nb	Fe	Ti	Al	Co
Min	20.00	8.00	3.15	-	-	-	-
Max	23.00	10.00	4.15	5.00	0.40	0.40	1.00

	Si	Mn	C	Ta	P	S	Ni
Min	-	-	-	-	-	-	58.00
Max	0.50	0.50	0.10	0.005	0.015	0.015	Bal.

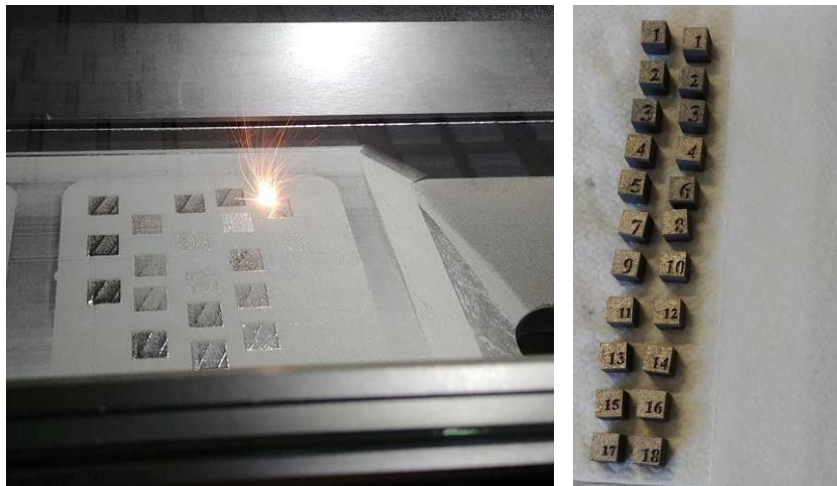


Figure 24: production of the samples on the LPBF machine and pictures of some IN625 + 1 wt. % TiC samples.

Samples shown in Figure 24 were fabricated by means of a Mlab Cusing R system (Concept Laser GmbH, Lichtenfels, Germany). Different types of samples were produced:

- Cubic 1 x 1 x 1 cm samples that have been utilised to evaluate the porosity, the microstructure and the hardness of the material.
- Tensile tests samples with a gauge length of 16 mm and a diameter of 4 mm.

All the samples were produced with a fixed laser power of 95 W and a layer thickness of 20 μm . The scanning strategy used for the jobs consists of stripes of 5 mm with a rotation of 67° between consecutive layers of powder. Different scanning speeds and hatching distances were considered with the aim to optimize the process parameters and the combinations are reported in Table 4.

Table 4: Process parameters. Sample were produced with a fixed laser power of 95 W and a layer thickness of 20 μm .

N° sample	Scanning speed [mm/s]	Hatching distance [mm]	VED [J/mm^3]
1	1600	0.03	99
2	1600	0.04	74
3	1600	0.05	59
4	1200	0.03	132
5	1200	0.04	99
6	1200	0.05	79
7	800	0.03	198
8	800	0.04	148
9	800	0.05	119
10	600	0.03	264
11	600	0.04	198
12	600	0.05	158
13	400	0.03	396
14	400	0.04	297
15	400	0.05	238

5.3 Archimedes' method

Archimedes' method is an economic way to evaluate the relative density of LPBFed parts [68]. This is a method widely used to measure the solid density and porosity of powder metallurgy products, in that they are related to the quality of the printed parts. It consists of measure the mass of the samples both in air and in a liquid (distilled water at room temperature for this purpose) with the use of an analytic balance (Figure 25), and the density is calculated with the following formula based on the Archimedes' principle:

$$\rho = m_{in\ air} \frac{\rho_{liquid}}{m_{in\ air} - m_{in\ liquid}}$$

where ρ_{liquid} is the density of the liquid generating buoyancy, $m_{in\ air}$ is the mass of the sample in air and $m_{in\ liquid}$ is the mass of the sample in the liquid. The relative density is calculated as follows:

$$\rho_{rel} = \frac{\rho}{\rho_{th}} 100$$

where ρ_{th} is the theoretical density. The theoretical density can be evaluated knowing both the IN625 density ($8.44\ \text{g}/\text{cm}^3$) and the TiC density ($4.93\ \text{g}/\text{cm}^3$). The values of the theoretical density for each material are shown in Table 5.

Table 5: Theoretical density values.

Material	Theoretical density ρ_{th} [g/cm^3]
Inconel 625	8.440
Inconel 625 + 1 wt. % TiC	8.384

However, in this thesis, for the density of the composite was used the vale determined by picnometric analysis instead of the theoretical density ($8.417\ \text{g}/\text{cm}^3$)

The method has been applied according to the ASTM B311-17 standard [69], which is suitable for the materials with a porosity of less than 2 %, not taking into account the effect of the surface-connected cavities (open cavities).



Figure 25: Analytic balance for Archimedes' method.

5.4 Heat treatments

Different heat treatments were applied to the materials to study the microstructure evolution and mechanical properties of the composites compared to the Inconel 625 alloy. Materials were treated in a muffle furnace in the air followed by water quenching to avoid any precipitation of secondary phases during cooling. The heat treatments are listed in Table 6.

Table 6: List of heat treatments.

Heat treatment (HT)	Solutioning temperature	Solutioning time	Ageing temperature	Ageing time
HT1	1150 °C	2 h	\	\
HT2	1150 °C	2 h	700 °C	8 h
HT3	980 °C	1 h	\	\
HT4	870 °C	1 h	\	\
HT5	1190 °C	2 h	\	\

5.5 Metallographic preparation

Before analyzing the samples, is necessary to prepare them by metallographic preparation. It consists of three steps:

- Cutting: samples were cut in half with the Presi Mecatome T210 precision automatic micro-cutting machine shown in Figure 26 a. Samples were cut along the building

direction (z-axis) and perpendicular to the building direction (x-y plane) to evaluate the microstructure in both planes.

- Polishing: a Presi Mecatech 234 polishing machine shown in Figure 26 was used. The samples were polished using 180-800-1000-2500 SiC grind papers. Then, diamond suspensions were used to obtain a 1 μm polishing. Finally, a mix of distilled water and alumina suspension was used to obtain a fully polished surface.
- Chemical etching: with the aim to highlight the grain boundaries, melt pools, and precipitates, a chemical etching was performed on the polished samples.



Figure 26: Presi Mecatome T210 precision automatic micro-cutting machine (a) and Presi Mecatech 234 polishing machine (b) [70], [71].

5.6 Samples analysis

5.6.1 Optical microscope



Figure 27: Leica DMI5000 M inverted research microscope [72].

The optical microscope, also referred to as a light microscope, is a type of microscope that commonly uses visible light and a system of lenses to generate magnified images of small

objects. The microscope was used to evaluate the porosity in polished samples by taking 10 images for each sample at 100x magnification which were then analysed with ImageJ, and to study the microstructure evolution of etched samples with a focus on grain boundaries, melt pools, and precipitates at different magnifications. In this thesis, a Leica DMI5000 M inverted research microscope shown in Figure 27 was used.

5.6.2 SEM microscope

Scanning electron microscope (SEM) exploits electron to obtain images by scanning the surface with a focused beam of electrons. It allows to obtain a higher resolution than an optical microscope in that the wavelength of electrons is lower than photons. The electrons interact with atoms in the sample, producing various signals which contain information about the surface topography and composition of the samples. The microscope is connected to an analytical energy-dispersive X-ray spectroscopy (EDS) to obtain a mapping of the elements that form the alloy. For this thesis, a SEM - Phenom XL (Phenom-World BV, Eindhoven, The Netherlands) shown in Figure 28 was used.



Figure 28: SEM - Phenom XL, Phenom-World BV [73]

5.6.3 ImageJ analysis

ImageJ is a Java-based open-source image processing program developed by the National Institute of Health (NIH). Images obtained from optical microscope have been processed with this software with the aim of calculating the porosity percentage with a method that provides the ratio between dark pixels (pores) and white pixels (matrix) by adding a colour threshold. The interface of the software is shown in Figure 29.

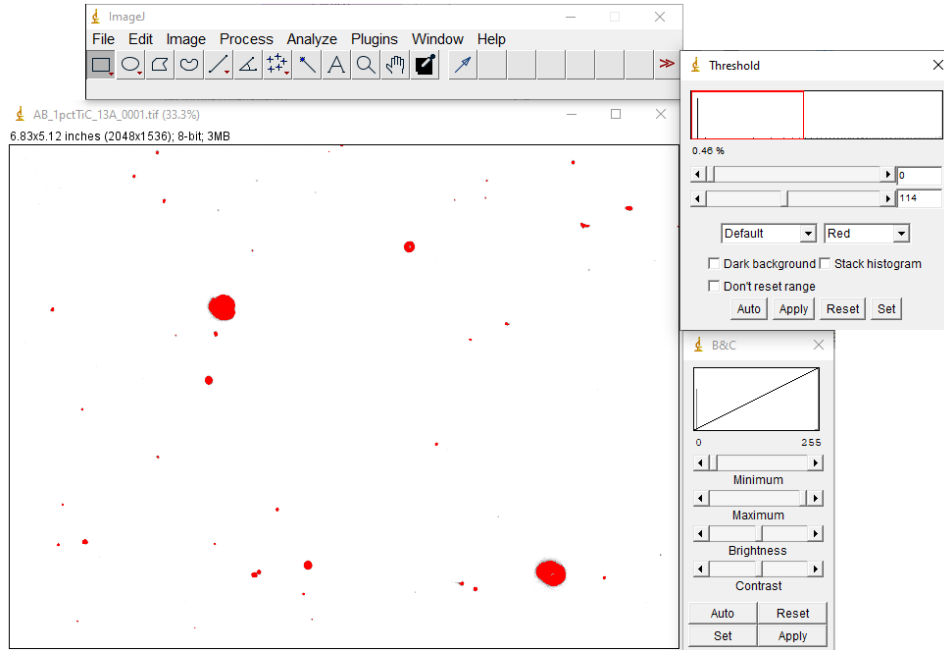


Figure 29: ImageJ interface.

5.7 Brinell hardness tests

Hardness is a measure of the resistance to localized plastic deformation induced by indentation. Hardness is an essential mechanical property that may correlate to tensile strength as well as wear resistance.

The testing machine consists of a support for the specimen and a spherical indenter made of hardened steel or tungsten carbide, which is pressed to the specimen with a defined force for a certain time. The mean diameter of the indentation is then evaluated with an optical microscope. Then, the Brinell hardness is calculated according to the following equation:

$$HBW = \frac{2F_{kgf}}{\pi D(D - \sqrt{D^2 - d^2})}$$

Where F_{kgf} is the test force in kgf, D is the diameter of the indenter ball in mm, and d is the measured mean diameter of the indentation in mm [74].

For this thesis, Brinell tests were carried out 5 times for each sample by means of an EMCO TEST M4U hardness test machine shown in Figure 30, with a load of 62.5 kg for 15 s (HBW2.5/62.5, HB10) in accordance with the ASTM E10-17 standard [74].



Figure 30: EMCO TEST M4U hardness test machine.

5.8 Tensile tests

Tensile tests provide information quite important for the aerospace field related on the strength and ductility of materials under uniaxial tensile stresses. In particular, they allow to obtain the stress-strain curve of the material, which contains the following information [75]:

- Young's modulus E : it is the constant of proportionality of the Hooke's law that is the equation that materials obey in elastic field:

$$\sigma_e = E \epsilon_e$$

where σ_e is the stress and ϵ_e is the elastic strain.

- Yield stress σ_y : it represents the stress that is needed to induce plastic deformation of the material. This value is often associated with the strain which induces a permanent strain of 0.2 %.
- Ultimate tensile strength UTS or σ_f : it represents the maximum stress that the material can handle before it is subjected to brittle breaking in case of brittle materials or the stress at which a necking appears with a reduction of the cross-sectional area.
- Breaking strength σ_r : it represents the stress at which the sample breaks, and it can coincide with σ_f in brittle materials.
- Elongation: it is a measure of deformation that occurs before the material break.

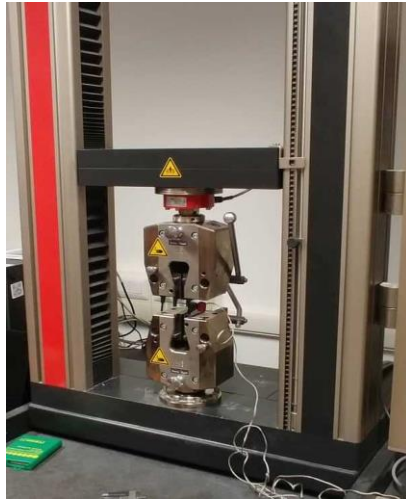


Figure 31: Zwick Roell -Ulm Germany Z050 tensile-tester.

Tensile tests were conducted according to the ASTM E8/E8M-16A standard [76] by a Zwick Roell -Ulm Germany Z050 tensile-tester with samples in AB and HT1 conditions. The gauge length of the samples is 16 mm, and the diameter of the cross-section is 4 mm.

6 Results

6.1 Powder characterization

The first experiment has been conducted by a Hall flowmeter funnel according to ASTM B213-20 standard [64]. Since none of the powder flowed through this funnel, it was necessary to use a Carney flowmeter for the purpose, following the ASTM B964-16 standard [65]. It resulted that only the powders of Inconel 625 and Inconel 625 + 1 wt. % TiC flow in the Carney funnel. This probably means that the TiC particles increase the interparticle friction thus affecting the flowability of the powder. Therefore, concentration of 2-3 wt. % of TiC dramatically altered the flowability, resulting in no flow of the powder through the Carney funnel.

The apparent density results show that for powder of Inconel 625 from 0 to 3 wt. % TiC content the apparent density decrease with the increment of the content of TiC (Figure 32), as the TiC has a lower density than Inconel 625.

Numerical results are reported in Table 7.

Table 7: Flowability and apparent density results. The flowability test were carried out by a Carney flowmeter with 150 g of powder.

Powder	Flow time [s]	St. dev.	Apparent density [g/cm ³]	St dev
IN625	8.73	0.12	4.44	0.01
IN625 + 1 wt. % TiC	14.47	0.47	4.32	0.01
IN625 + 2 wt. % TiC	-	\	4.14	0.01
IN625 + 3 wt. % TiC	-	\	4.04	0.01

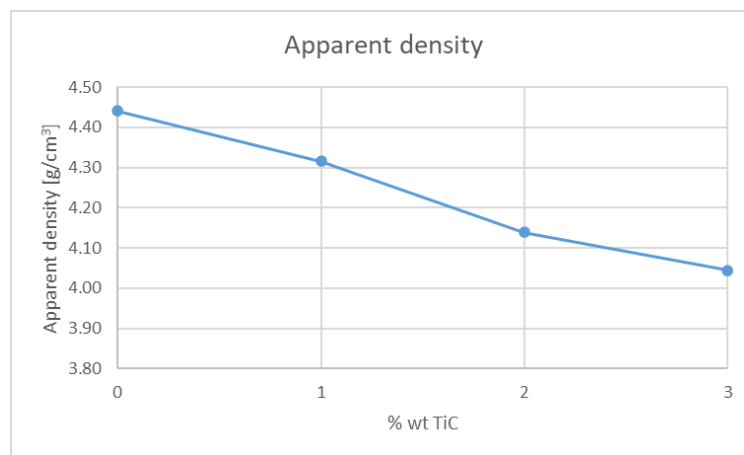


Figure 32: Apparent density in function of the wt. % TiC powder.

Based on these results, it was chosen to produce composite sample with 1 wt. % TiC, since the powder still keep a certain flowability in the Carney flowmeter.

Figure 33 shows the SEM images of the Inconel 625 powder mixed with 1 wt. % TiC. Inconel 625 particles appear fairly spherical, even if some irregular particles are visible, while TiC

particles are visible as dark and irregular-shaped particles, as confirmed by EDS maps (Figure 34). The powder with 1 wt. % TiC shows a good adhesion between the matrix and the reinforcement. TiC particles are distributed quite uniformly.

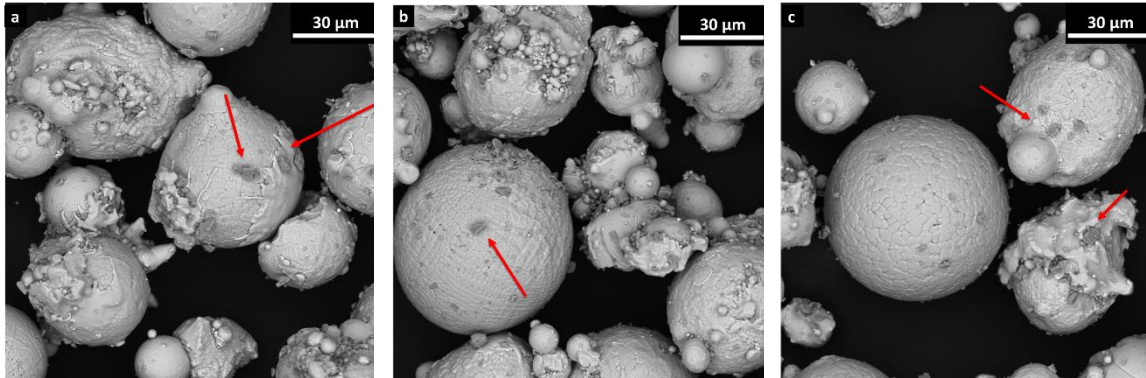


Figure 33: SEM images of IN625 + 1 wt. % TiC powder. In red are highlighted TiC particles.

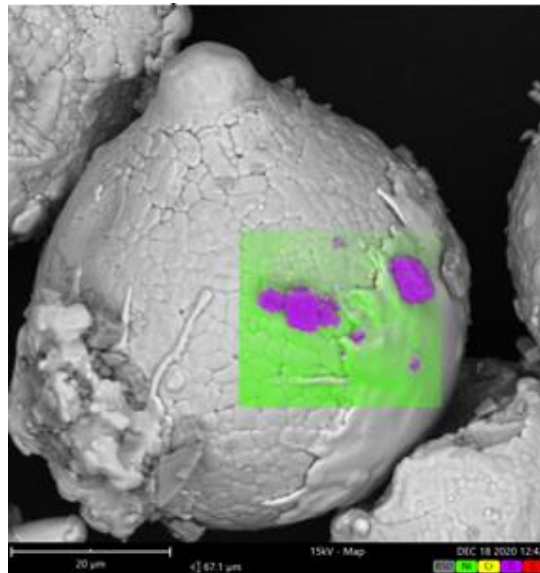


Figure 34: EDS maps of powder of IN625 + 1 wt. % TiC which confirm the presence of TiC particles.

6.2 Porosity and parameters optimization

From this section on, the Inconel 625 will be called “alloy” and the Inconel 625 + 1 wt. % TiC will be called “composite”.

In Figure 35 are reported the data of porosity percentage found with the Archimedes’ method in relation to VED of the alloy and the composite. It can be noticed that the VED necessary to obtain a dense composite is higher with respect to the alloy. In fact, according to these values, it is possible to obtain a low level of porosity (< 0.5 %):

- From VED = 99 J/mm³ for the alloy.
- From VED = 132 J/mm³ for the composite.

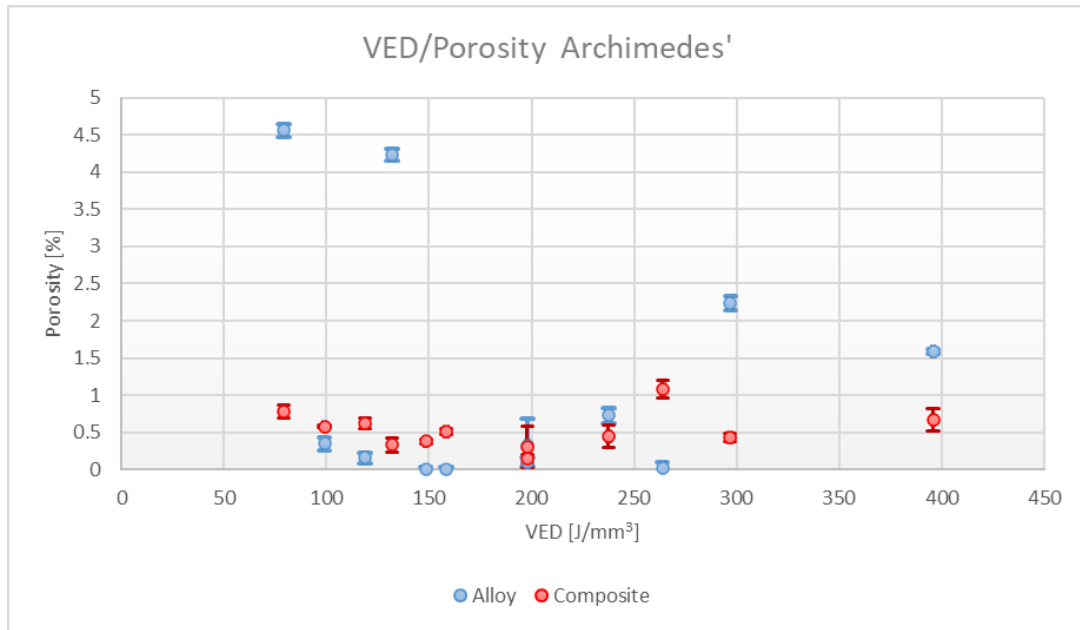


Figure 35: Relation between VED and porosity obtained with Archimedes' method for the alloy and the composite.

Sample were also observed by optical microscope, and the porosity was calculated with ImageJ. For the composite were considered the pores with a diameter higher than 5 μm to avoid counting the unmelted TiC particles, and the trends are shown in Figure 36. It can be noticed that at low VED (up to 99 J/mm^3) is possible to obtain porosity less than 0.1 % for the alloy, while the porosity drastically increases at higher VED. The composite, instead, presents a higher porosity than the alloy for low VED, but is possible to obtain denser samples than the alloy at higher VED.

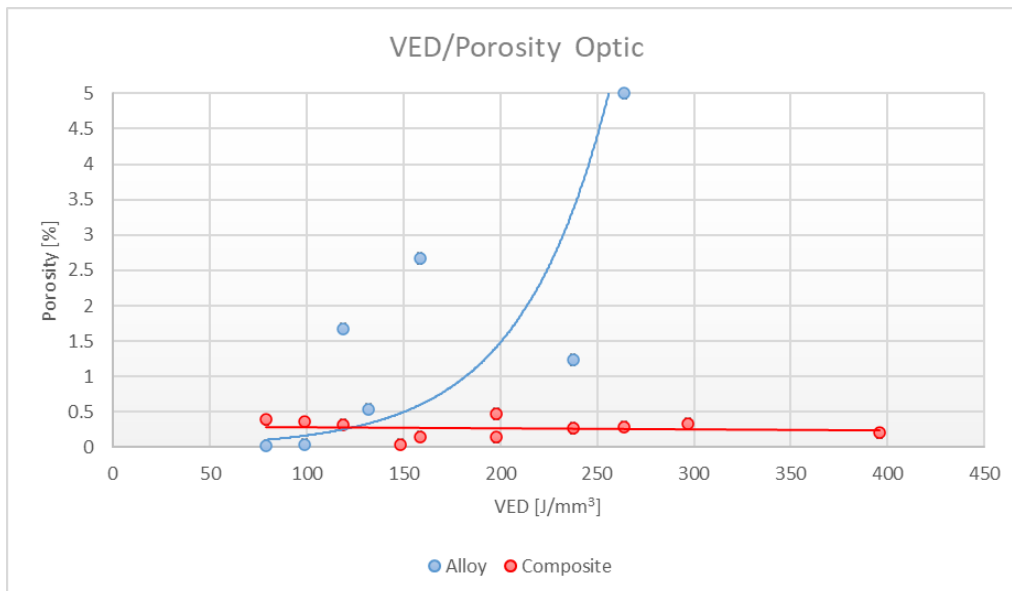


Figure 36: Relation between VED and porosity obtained by the optic microscope for the alloy and the composite.

The process mapping of composite is shown in Figure 37. Images show the presence of lack of fusion with a size up to 200 – 300 μm in the samples with higher scanning speed, while they

disappear at scanning speed lower than 1200 mm/s. It can be noticed the presence of micrometric particles up to 5 μm of diameter that consists of TiC particles, and they are more evident in the sample with a lower VED. This may mean that the process is not able to melt the TiC particles because of the much higher melting point of the ceramic reinforcement.

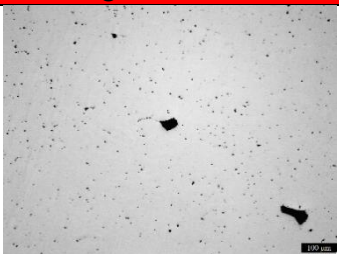
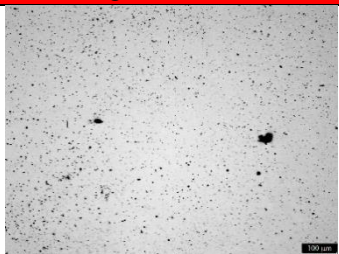
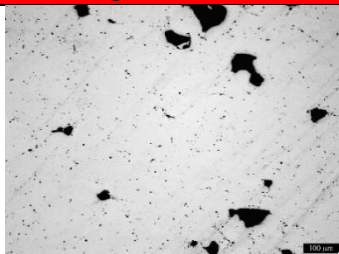
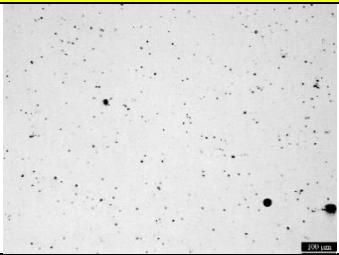
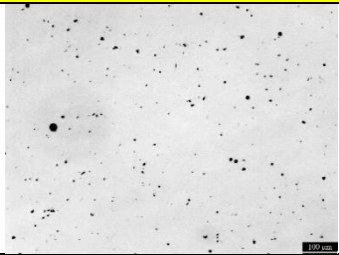
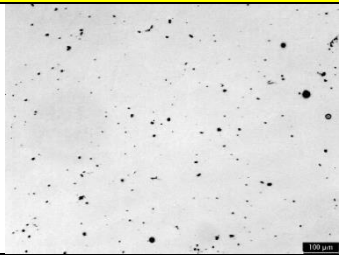
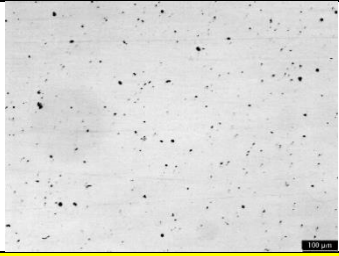
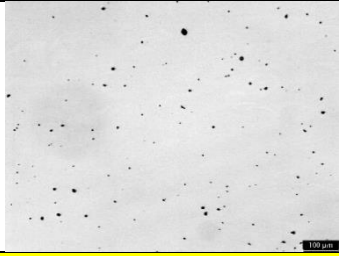
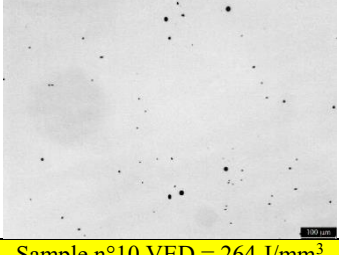
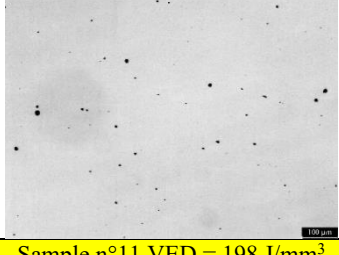
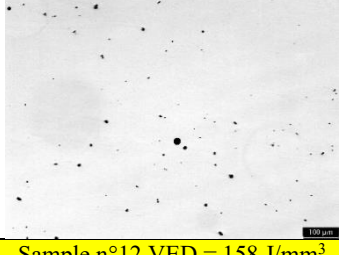
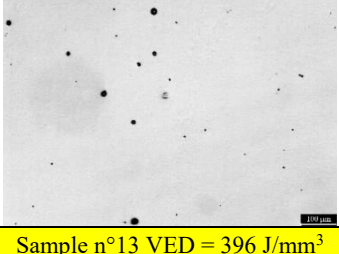
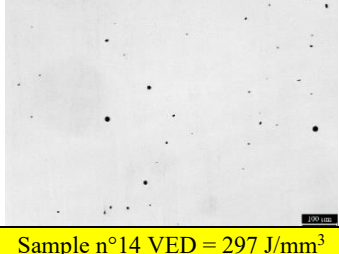
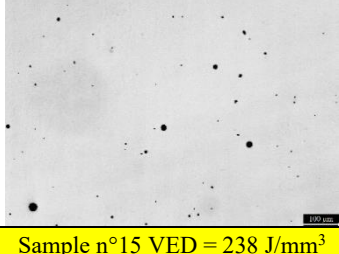
	Hatching distance 0.03 mm	Hatching distance 0.04 mm	Hatching distance 0.05 mm
Scanning speed 1600 mm/s			
	Sample n°1 VED = 99 J/mm ³	Sample n°2 VED = 74 J/mm ³	Sample n°3 VED = 59 J/mm ³
Scanning speed 1200 mm/s			
	Sample n°4 VED = 132 J/mm ³	Sample n°5 VED = 99 J/mm ³	Sample n°6 VED = 79 J/mm ³
Scanning speed 800 mm/s			
	Sample n°7 VED = 198 J/mm ³	Sample n°8 VED = 148 J/mm ³	Sample n°9 VED = 119 J/mm ³
Scanning speed 600 mm/s			
	Sample n°10 VED = 264 J/mm ³	Sample n°11 VED = 198 J/mm ³	Sample n°12 VED = 158 J/mm ³
Scanning speed 400 mm/s			
	Sample n°13 VED = 396 J/mm ³	Sample n°14 VED = 297 J/mm ³	Sample n°15 VED = 238 J/mm ³

Figure 37: Representative OM images of LPBFed IN625 + 1 wt. % TiC. Note that the laser power and layer thickness are constant at 95 W and 20 μm , respectively.

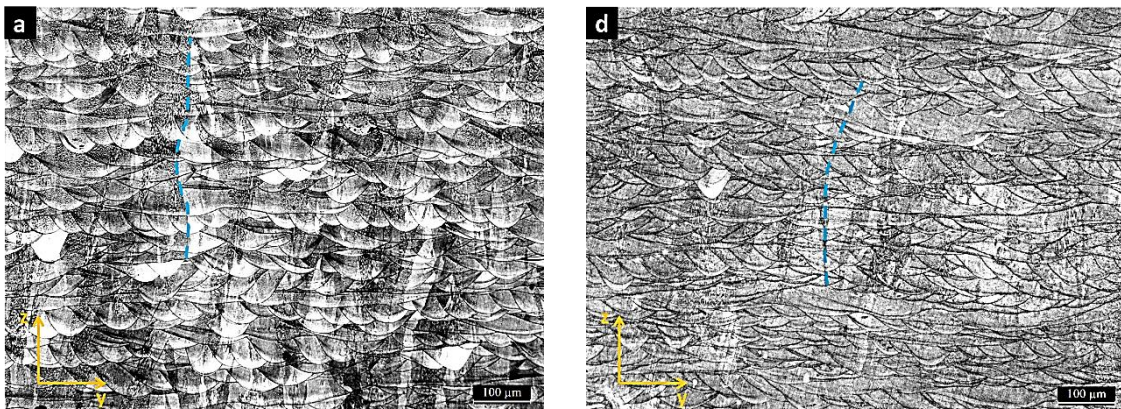
6.3 Microstructure

In this section it was made a microstructure comparison between the optimized alloy and the composite at the as-built state and after heat treatments.

The study of the composite was performed on the samples built with the parameters $v = 600\text{mm/s}$, $h_d = 0.04\text{ mm}$, $P = 95\text{ W}$ and $t = 20\text{ }\mu\text{m}$. The density of the new samples was checked, confirming a relative density very close to 100 %.

6.3.1 Microstructure of samples in as-built condition (AB)

OM images in Figure 38 and SEM images in Figure 40 show the microstructure in the building direction (z-axis) of the alloy (a-c) and the composite (d-f) in AB conditions. It can be noticed that in both material the melt pools are clearly visible, are partially overlapped and the sizes are different because of the rotation of each layer of 67° chosen as scanning distance [40]. Adhesion between layers is good. Grains are elongated along the building axis (z-axis), as expected from the literature. However, the composite presents zones with finer grains than the alloy due to the addition of the ceramic particles. At higher magnifications, dendritic structures are visible showing an alternance of cellular and columnar dendrites, due to the high solidification rate of the process. Many particles with a size between 1 and 5 μm , which is coherent with TiC particles (highlighted in red), appear inside the composites, and the presence of TiC reinforcement was confirmed from EDS maps in Figure 41. It was realized that the TiC particles tend to refine the grains. Moreover, the presence of large particles of TiC could change the dendritic microstructure from cellular to columnar as TiC particles may reduce the G/V_c ratio [56], and this is visible at higher magnification in Figure 39 where a columnar dendritic zone is present nearby a large TiC particle. This could be due to the higher thermal conductivity of TiC ($23\text{ W/(m }^\circ\text{C)}$) than Inconel 625 ($12\text{ W/(m }^\circ\text{C)}$), so TiC particles dissipate heat to the molten pool faster, thereby increasing the cooling rate (V_c).



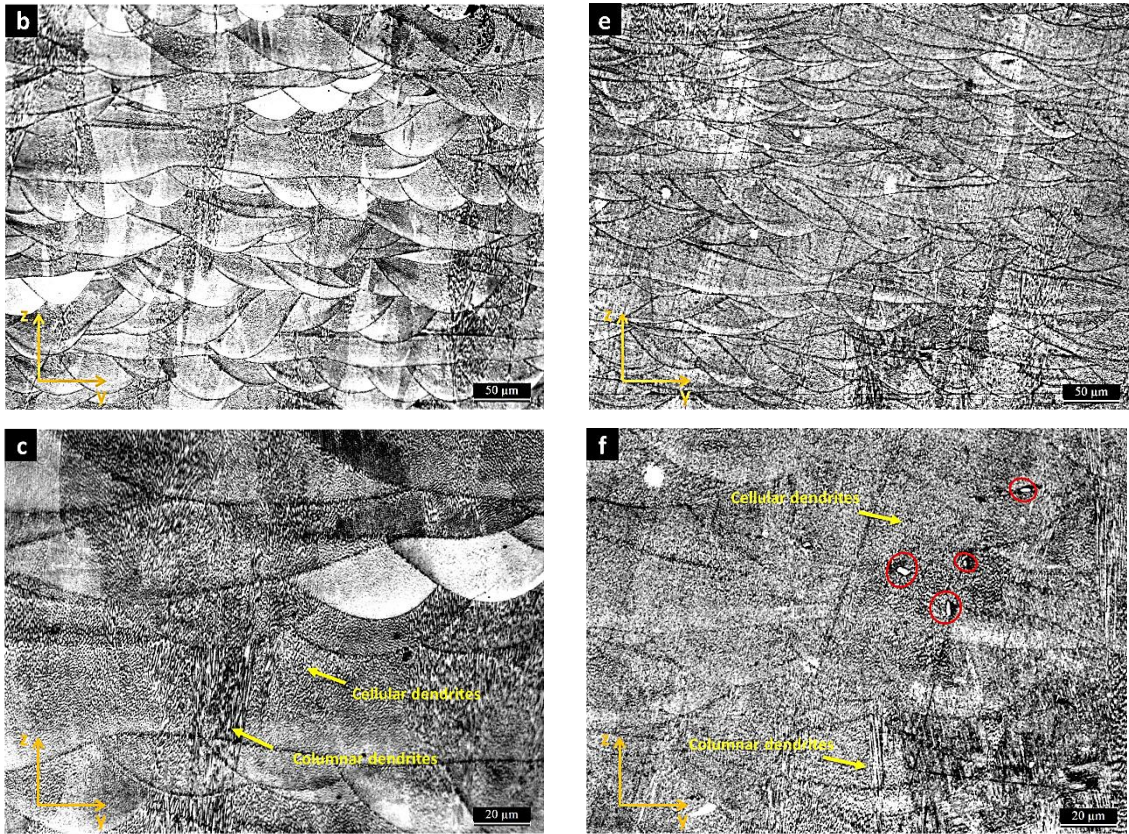


Figure 38: OM images of the alloy (a-c) and the composite (d-f) in AB conditions at 100x, 200x and 500x along the building direction (z-axis). In red are highlighted the TiC particles, in blue the grain boundaries.

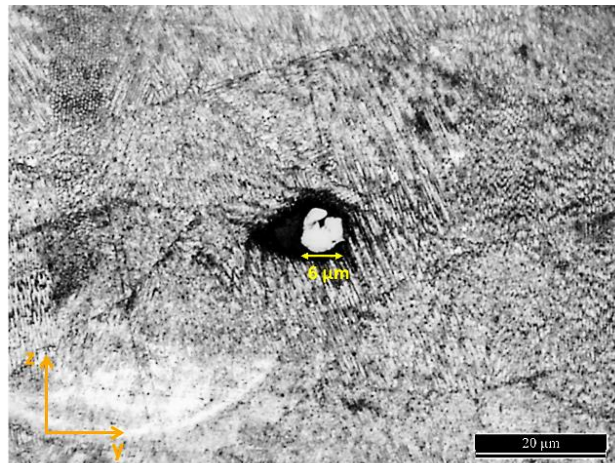


Figure 39: OM images of the composite in AB conditions at 1000x along the building direction (z-axis) showing a large TiC particle.

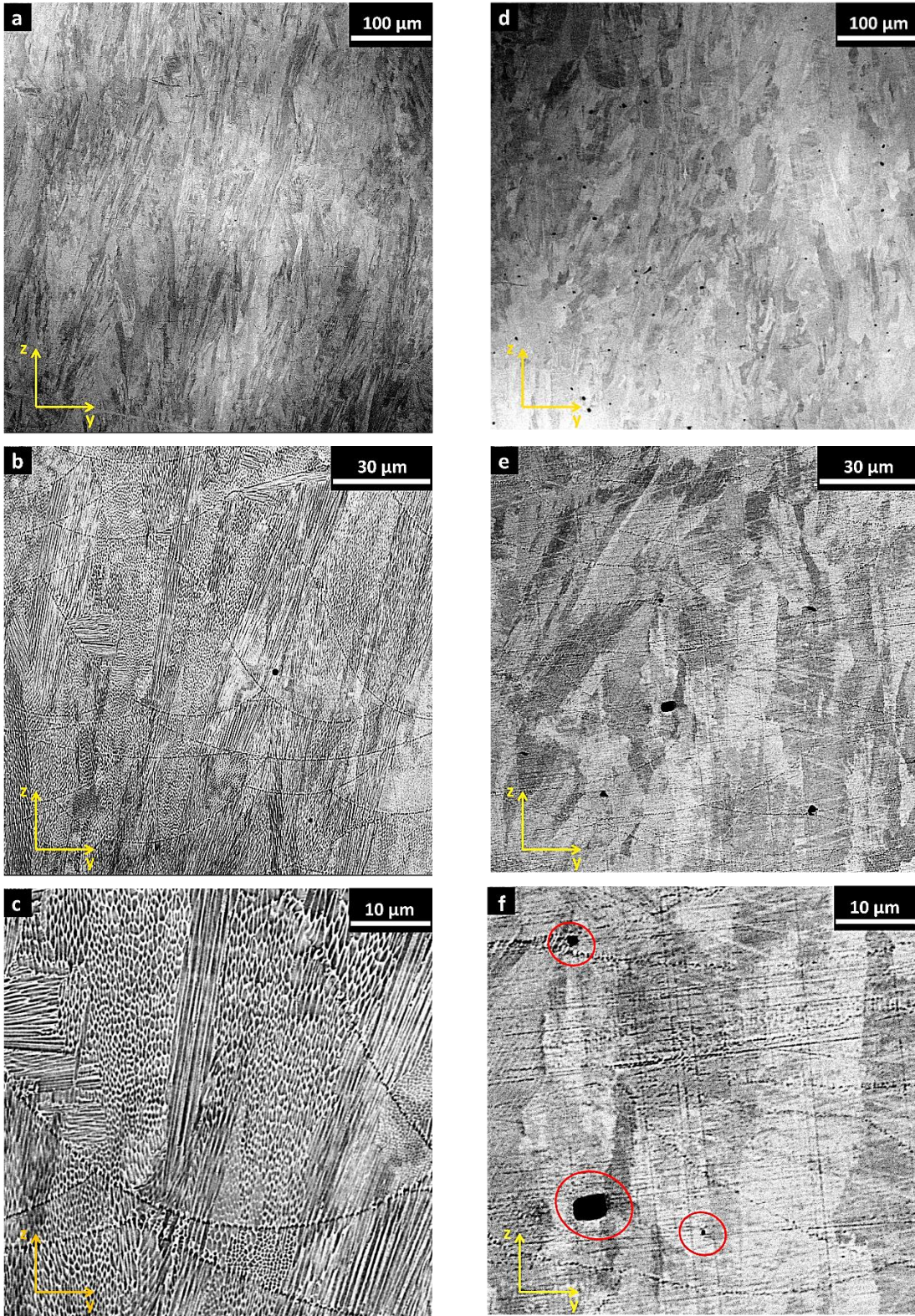


Figure 40: SEM images of the alloy (a-c) and the composite (d-f) samples in AB conditions at 500x, 2000x, 5000x. In red are highlighted TiC particles.

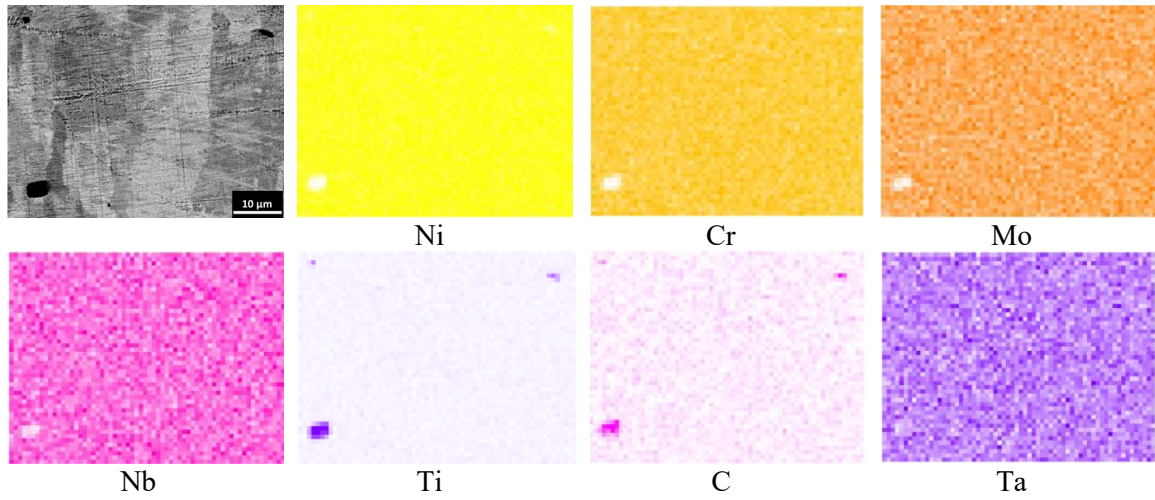
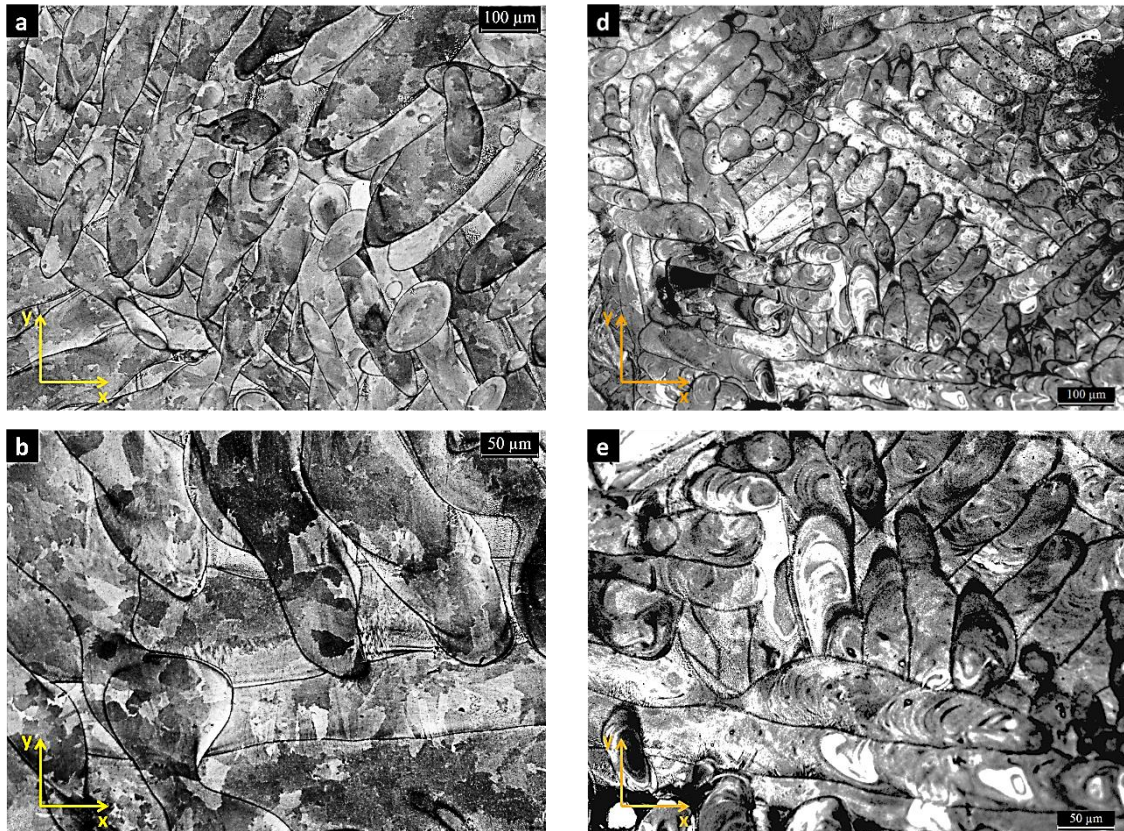


Figure 41: EDS maps of the composite sample in AB condition showing TiC particles.

The OM images in Figure 42 show the plane x-y of the alloy (a-c) and the composite (d-f) at different magnifications, which point out the overlapped melt pool and confirm the presence of TiC particles in the composite (highlighted in red).



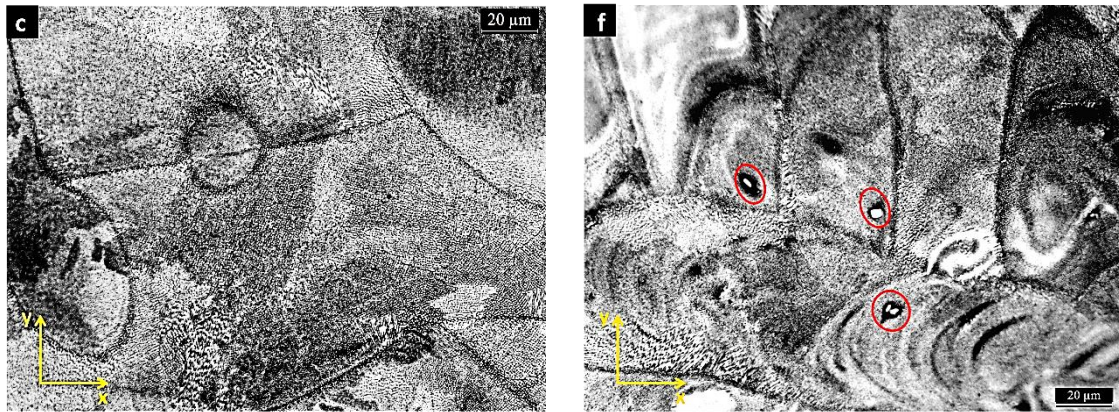


Figure 42: OM images of the alloy (a-c) and the composite (d-f) in AB conditions at 100x, 200x and 500x along the x-y plane. In red are highlighted the TiC particles.

6.3.2 Microstructure of samples solutioned at 1150 °C for 2 hours (HT1)

OM images in Figure 43 and SEM images in Figure 44 show the microstructure in the building direction (z-axis) of the alloy (a-c) and the composite (d-f) in HT1 conditions. The grains are quite different, as the alloy developed equiaxed grain after the solution treatment, while the composite still presents columnar grains along the building direction, though initial recrystallization seems began. The reason is suggested by Chen et al. [55] who studied the effect of heat treatments on the microstructure of TiC/Inconel 625 nanocomposites fabricated by LPBF founding that the TiC particles tend to increase the thermal stability of the composite and so the recrystallization begins at a temperature higher than IN625 alloy. So, the solutioning treatment at 1150 °C for 2 hours is not sufficient to fully recrystallize the composite. In both the material dendritic structure were eliminated after the heat treatment. It is interesting to note that twin boundaries appear frequently in the alloy, while in the composite they rarely appear. At higher magnifications, it is possible to observe the precipitates, and it can be noticed that in the alloy precipitates are finer and well distributed into the matrix (probably carbides, according to the diagram T-T-T of Inconel 625), while the composite presents a much higher content of larger precipitates (also > 1 μm), which are larger in the grain boundaries, while finer precipitates appear intragrain and in the grain boundaries. From EDS maps (Figure 45), it resulted that these precipitates are carbides rich in niobium preferentially, and molybdenum in the second hand, but tracks of titanium are visible. The higher content of carbides in the composite may be due to the higher content of carbon which may derive from the decomposition of TiC particles in titanium and carbon during the solutioning treatments at high temperatures [55]. It seems that the excess carbon has a higher affinity with niobium, forming carbides rich of this element, and this may improve the hardness, tensile properties and creep resistance of the composite, losing in ductility, compared with the alloy at the same conditions. However, large TiC particles are still present in the composite (highlighted in red), preferentially in grain boundaries, due to the fact that the LPBF process in not able to fully melt the reinforcement powder, and that carbides do not fully decompose at 1150 °C.

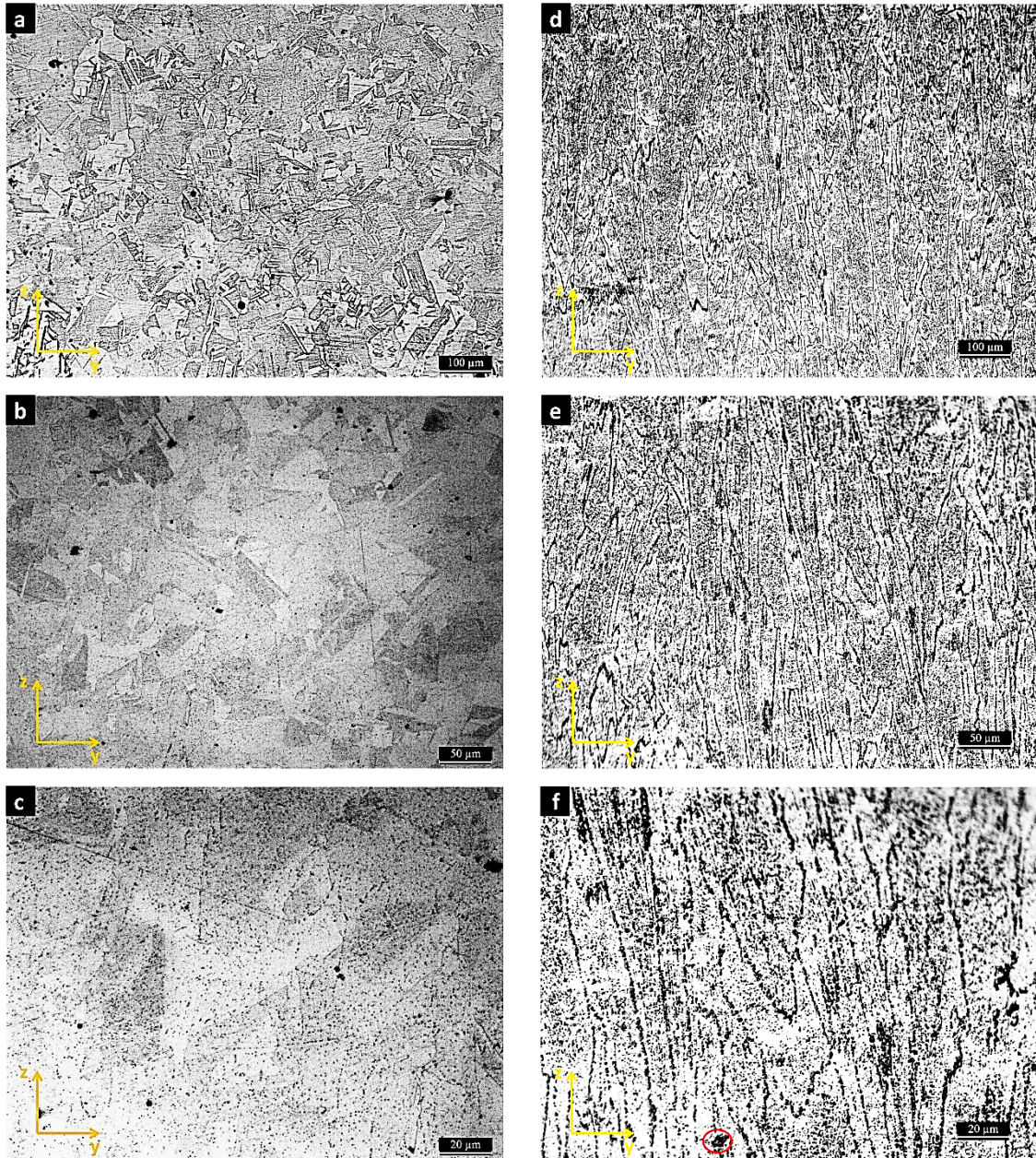


Figure 43: OM images of the alloy (a-c) and the composite (d-f) in HT1 conditions at 100x, 200x and 500x along the building direction (z-axis). In red are highlighted the TiC particles.

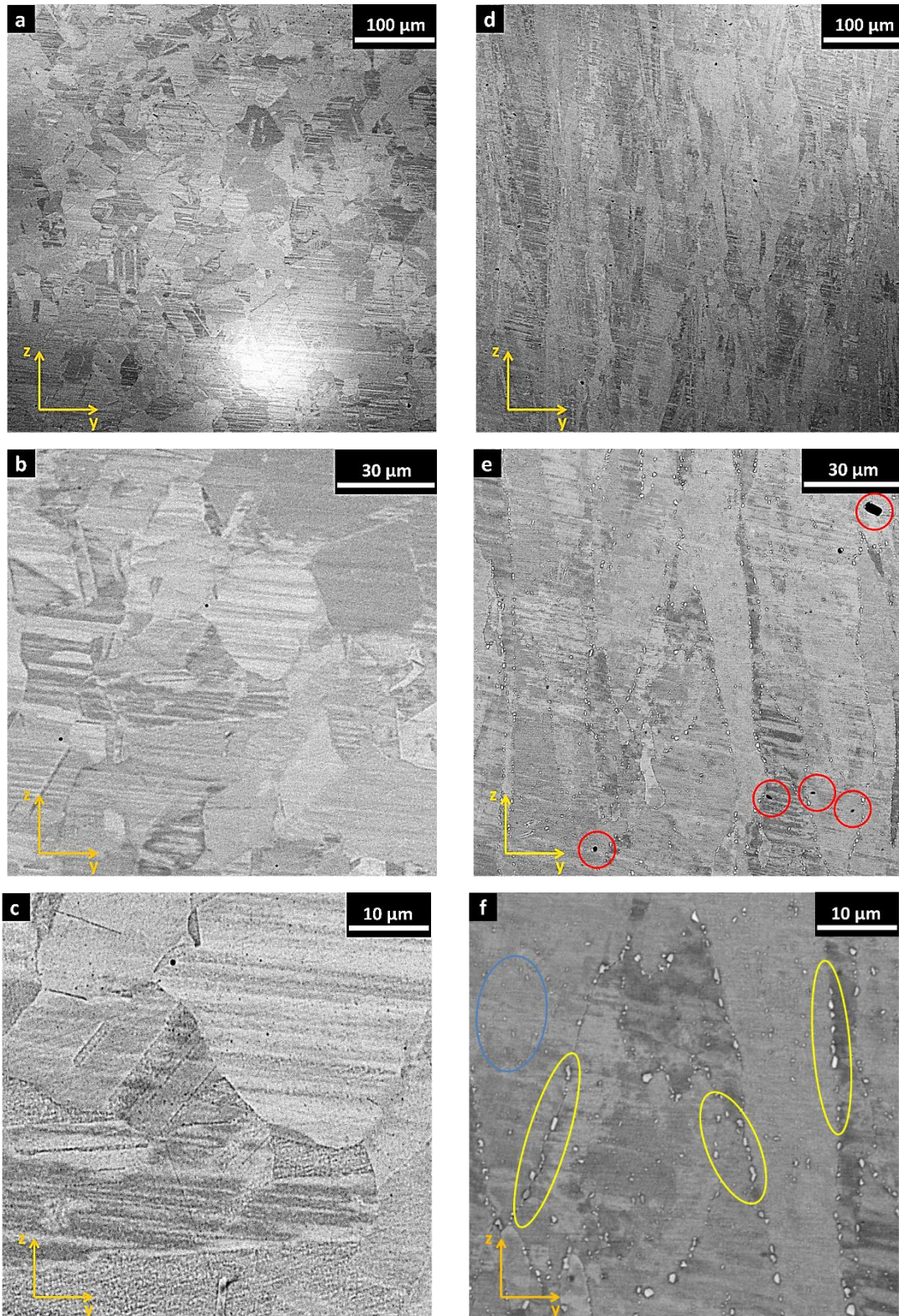


Figure 44: SEM images of the alloy (a-c) and the composite (d-f) samples in HT1 conditions along the building direction (z-axis) at 500x, 2000x, 5000x. In red are highlighted TiC particles, in yellow coarse carbides rich in niobium into the grain boundaries, in blue fine carbides into the matrix and along the grain boundaries formed during the recrystallization.

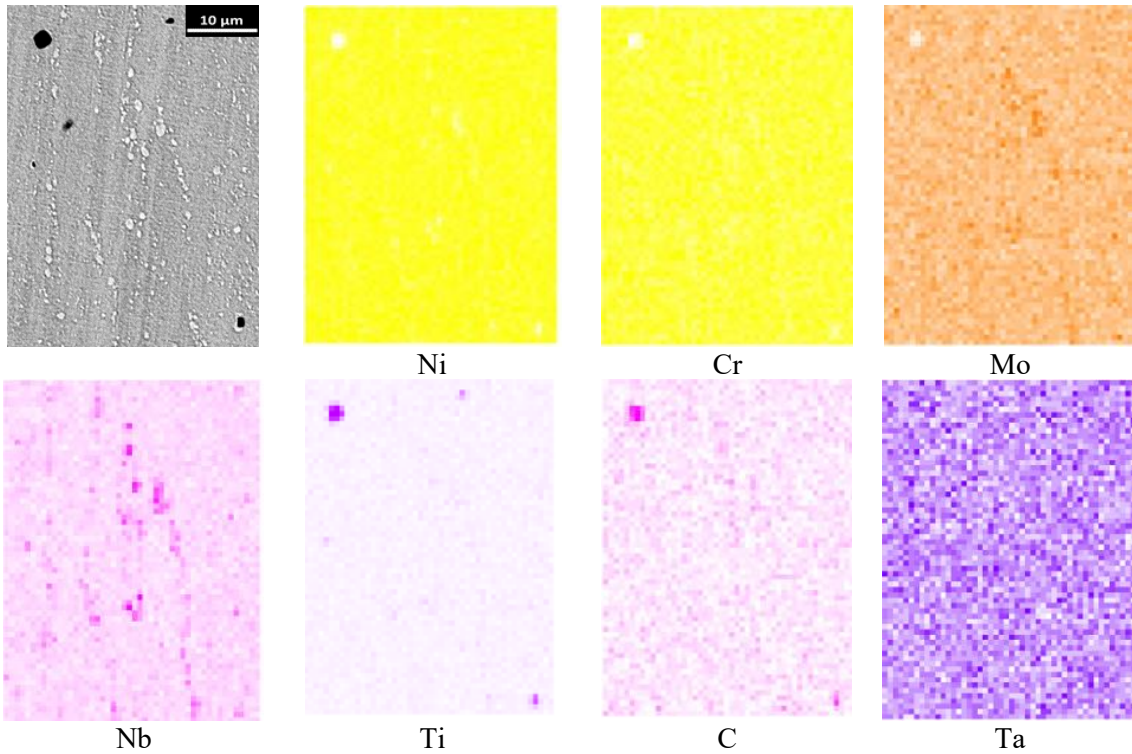
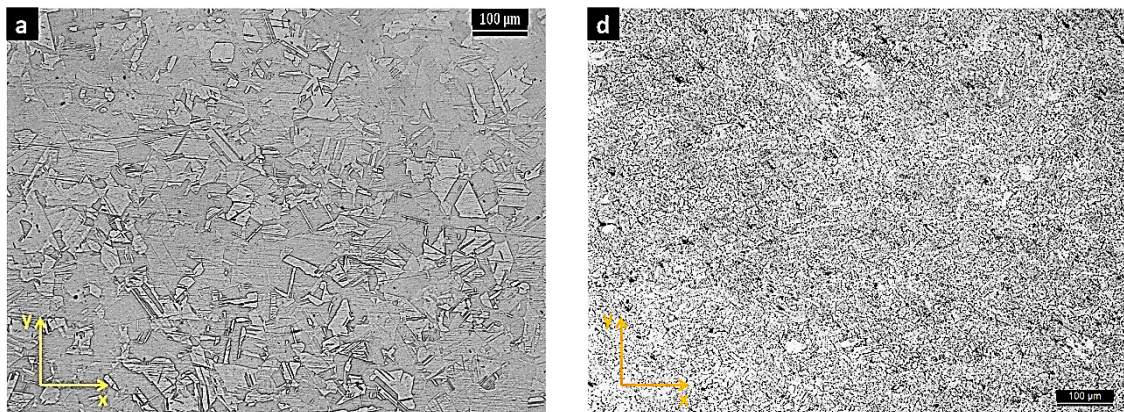


Figure 45: EDS maps of the composite sample in HT1 conditions at 3000x showing carbides rich in niobium and molybdenum, with tracks of titanium in the grain boundaries, and large TiC particles.

The OM images in Figure 46 show the plane x-y of the alloy (a-c) and the composite (d-f) at different magnifications. It can be noticed that grains of the composite are finer than the alloy, so it seems that the TiC particles (highlighted in red) tend to inhibit the grain growth.



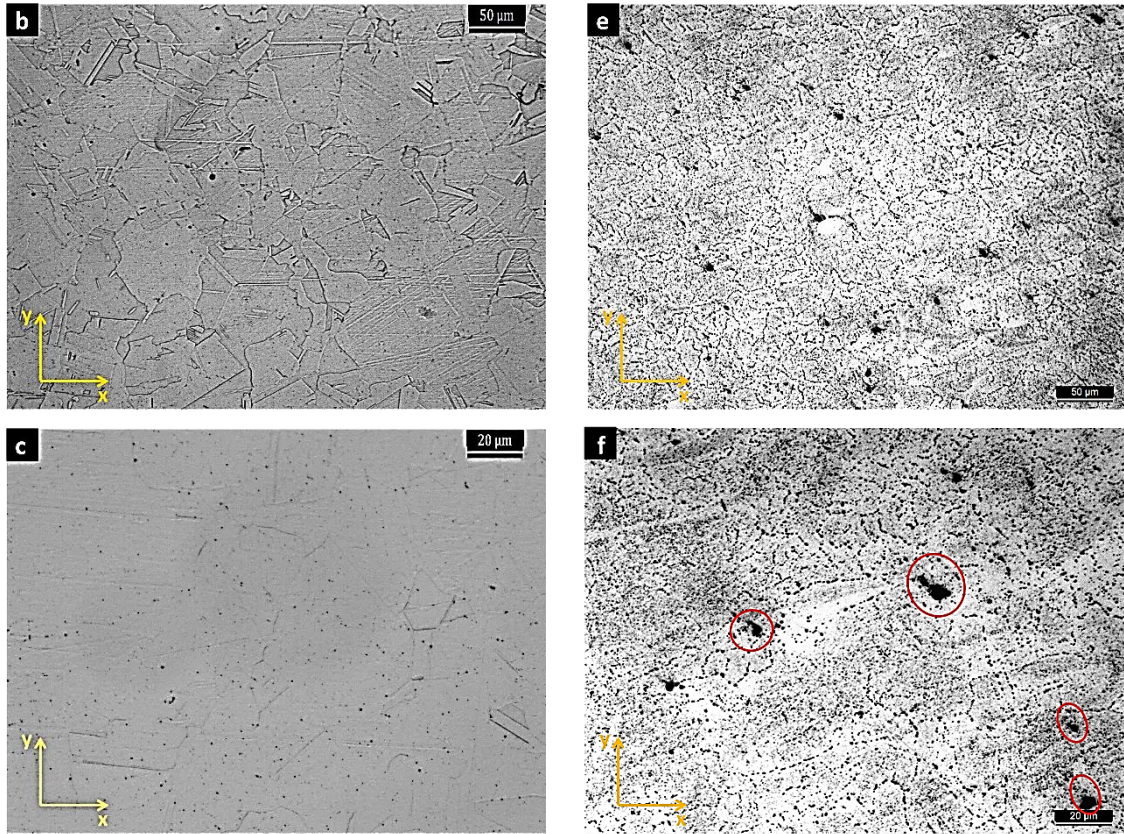


Figure 46: OM images of the alloy (a-c) and the composite (d-f) in HT1 conditions at 100x, 200x and 500x along the x-y plane. In red are highlighted the TiC particles.

6.3.3 Microstructure of samples solutioned at 1150 °C for 2 hours and aged at 700 °C for 8 hours (HT2)

OM images in Figure 47 and SEM images in Figure 48 show the microstructure in the building direction (z-axis) of the alloy (a-c) and the composite (d-f) in HT2 conditions. Like HT1 condition, the alloy has equiaxed grains, while the composite keep an alternance of columnar grains and refines zones, so the ageing treatment at 700 °C for 8 hours has no effect on the grain refinement. Grain boundaries appear more clearly than HT1 condition probably because of the higher content of inter-grain precipitates which consist of carbides and γ'' [13]. A large number of coarse precipitates are visible in the composite in grain boundaries, while finer precipitates appear into the matrix and in the new grain boundaries formed during the recrystallization. EDS maps in Figure 49 confirm that these large precipitates are rich prevalently in niobium, with tracks of molybdenum and titanium in the grain boundaries, so they consist of carbides according to T-T-T diagram of Inconel 625. Large TiC particles (highlighted in red) appear in the composite prevalently in grain boundaries, but many TiC particles are also present into the grains. A high number of twin boundaries are visible in the alloy, while they rarely appear in the composite. Dendritic structures are not visible as they were eliminated during the solutioning treatment in both the materials.

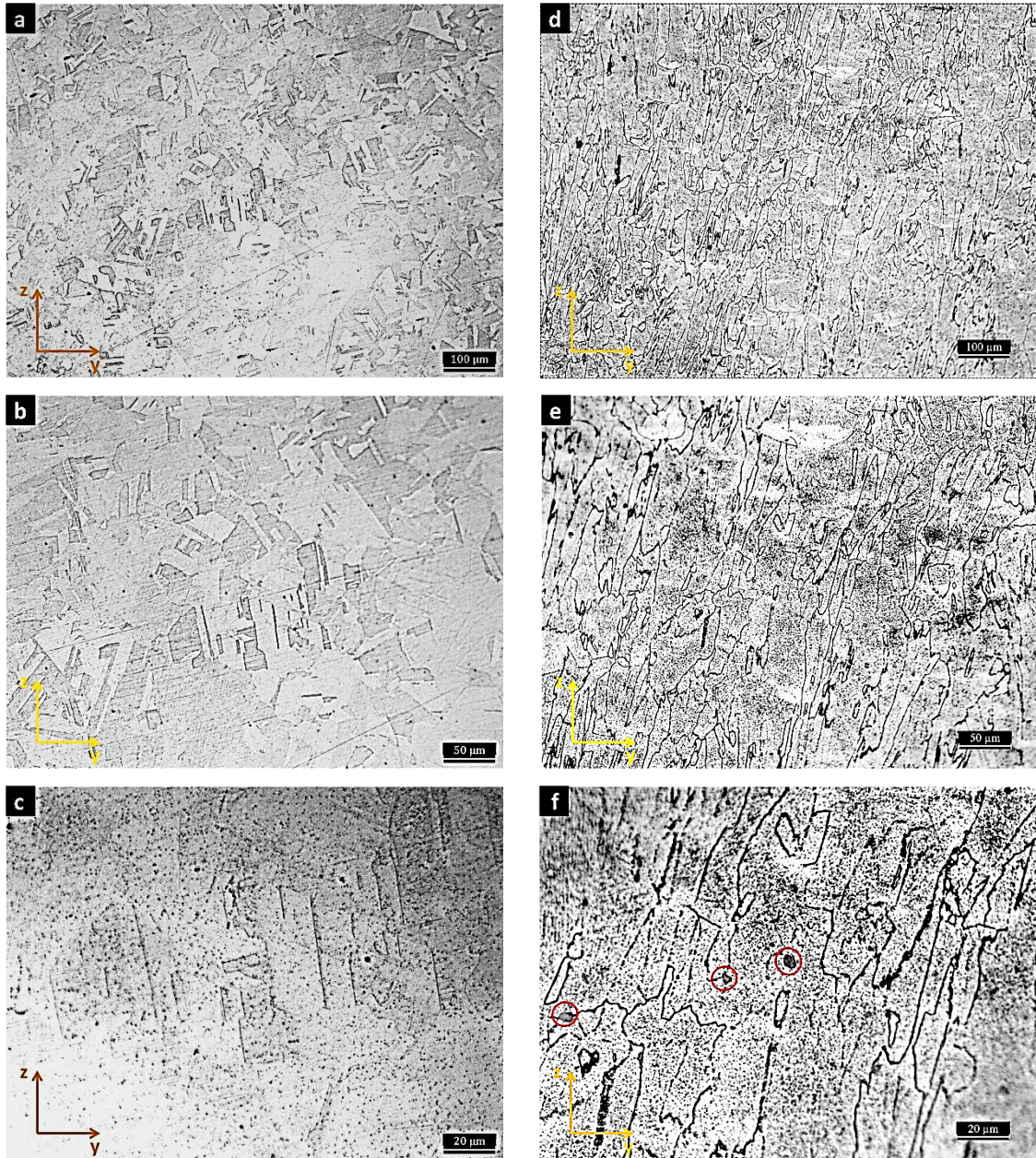


Figure 47: OM images of the alloy (a-c) and the composite (d-f) in HT2 conditions at 100x, 200x and 500x along the building direction (z-axis). In red are highlighted the TiC particles.

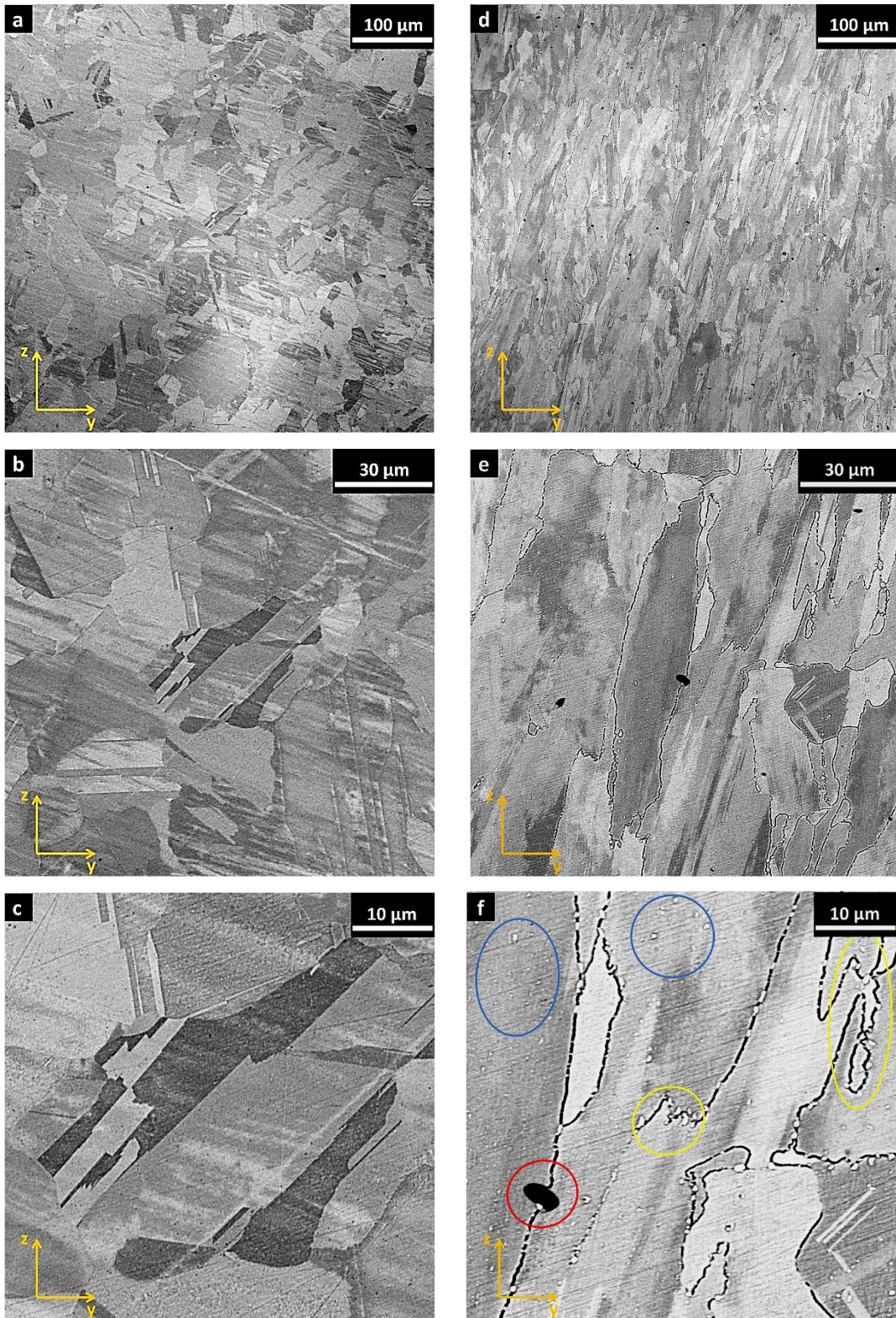


Figure 48: SEM images of the alloy (a-c) and the composite (d-f) samples in HT2 conditions along the building direction (z-axis) at 500x, 2000x, 5000x. In red are highlighted TiC particles, in yellow carbides into the grain boundaries and in blue fine carbides in new grains formed during the recrystallization.

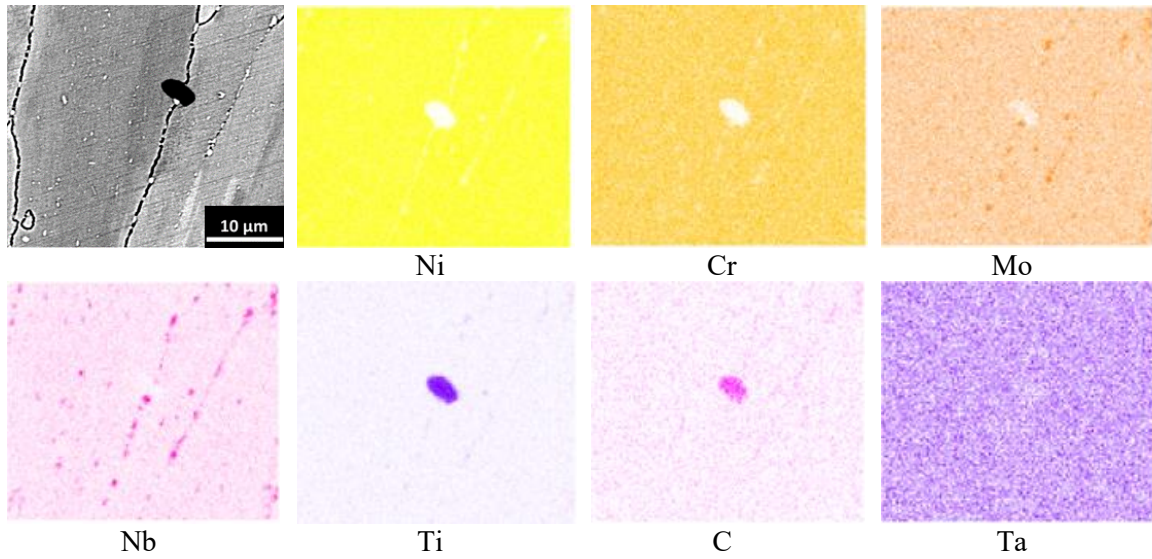
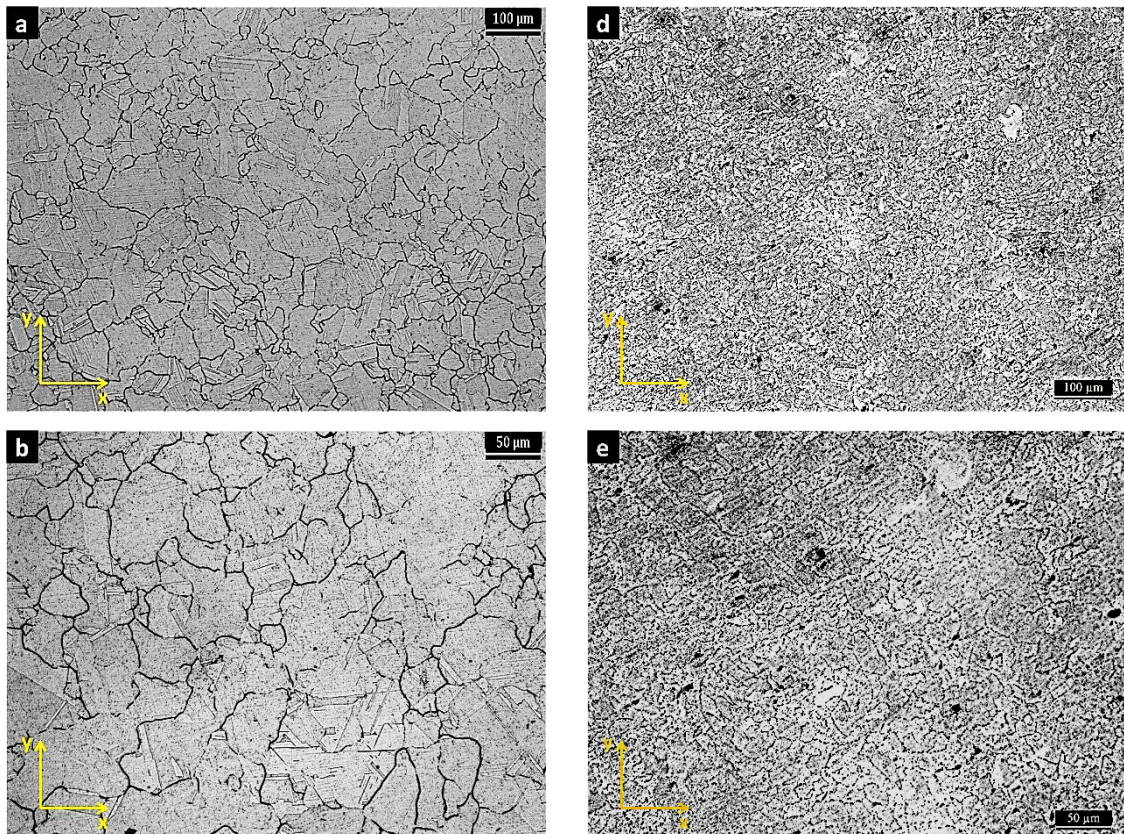


Figure 49: EDS maps of the composite sample in HT2 conditions at 3000x showing intra-grain TiC particles and carbides rich in niobium and molybdenum with tracks of titanium in the grain boundaries.

The OM images in Figure 50 show the plane x-y of the alloy (a-c) and the composite (d-f) at different magnifications. Also, in this condition the grains are finer in the composite.



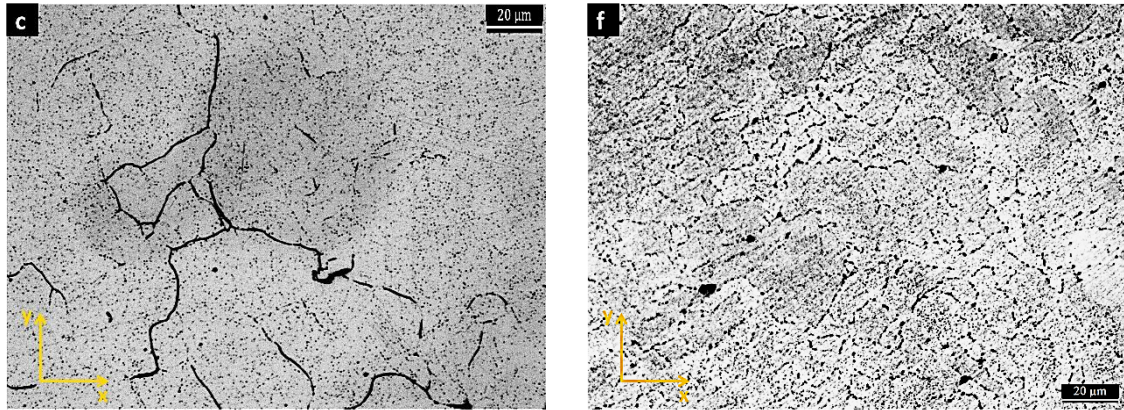
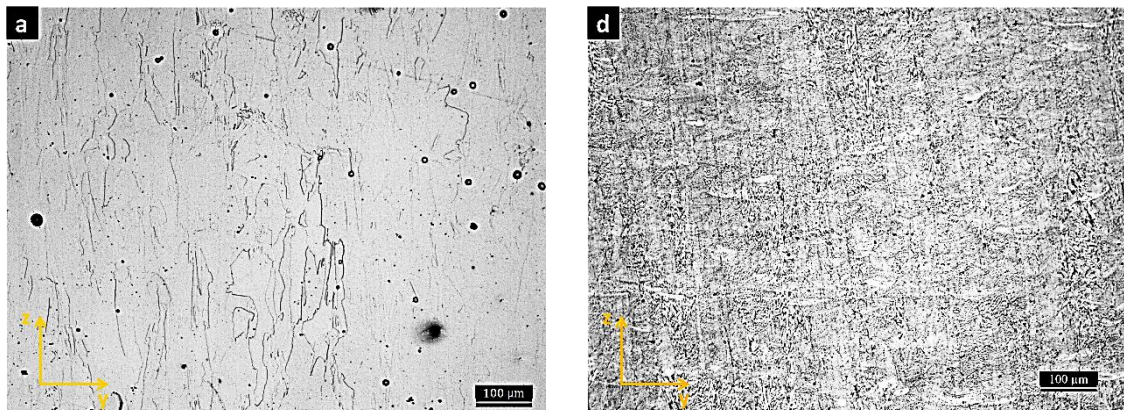


Figure 50: OM images of the alloy (a-c) and the composite (d-f) in HT2 conditions at 100x, 200x and 500x along the x-y plane.

6.3.4 Microstructure of samples solutioned at 980 °C for 1 hour (HT3)

OM images in Figure 51 and SEM images in Figure 52 show the microstructure in the building direction (z-axis) of the alloy (a-c) and the composite (d-f) in HT3 conditions. Both the material present large size and columnar grains with a preferential growth direction along the z-axis induced by the LPBF process. However, the composite presents some zones with finer grains compared with the alloy, especially in the zones with a higher concentration of TiC particles. EDS maps in Figure 53 confirm the presence of these ceramic particles in the composite. Dendritic structures were eliminated with the treatment in the alloy, while columnar and cellular dendrites are slightly visible in the composite.



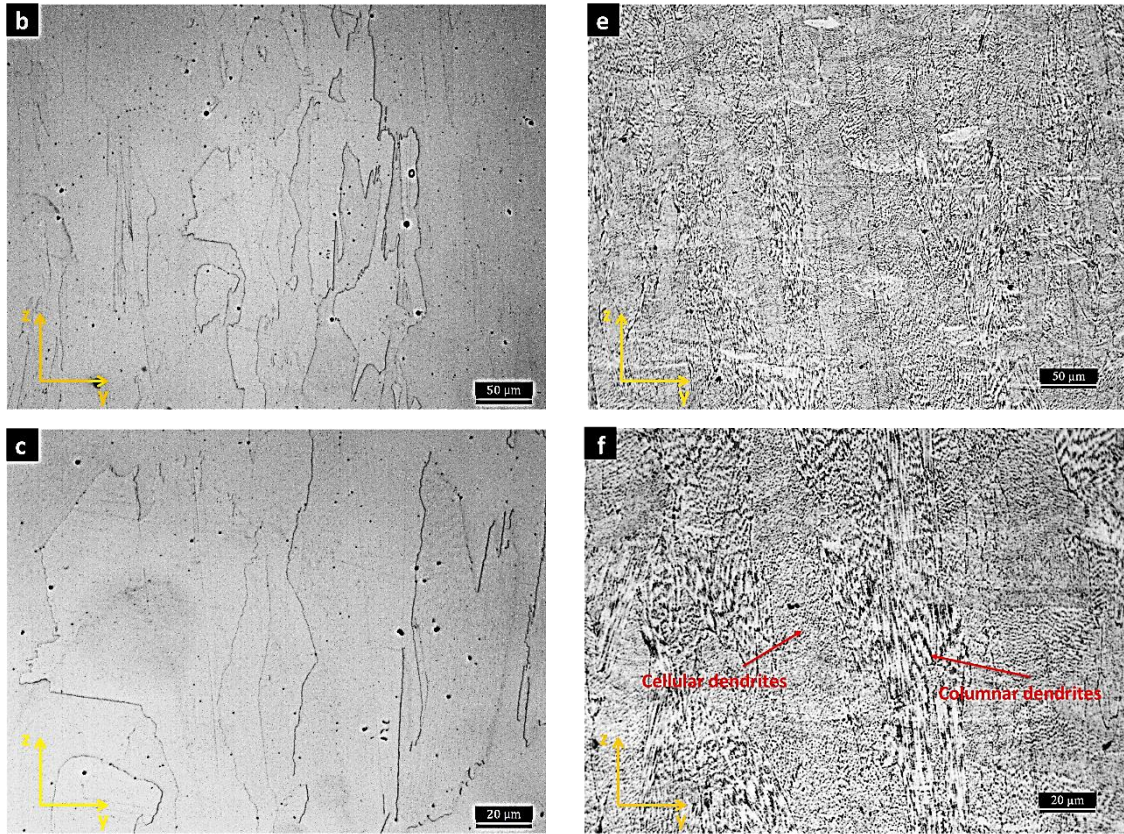
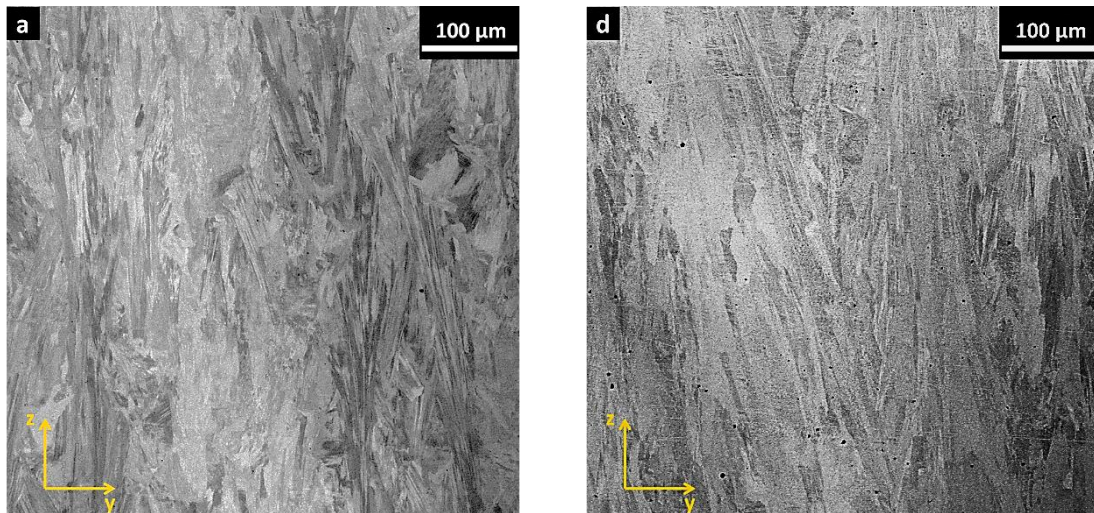


Figure 51: OM images of the alloy (a-c) and the composite (d-f) in HT3 conditions at 100x, 200x and 500x along the building direction (z-axis).



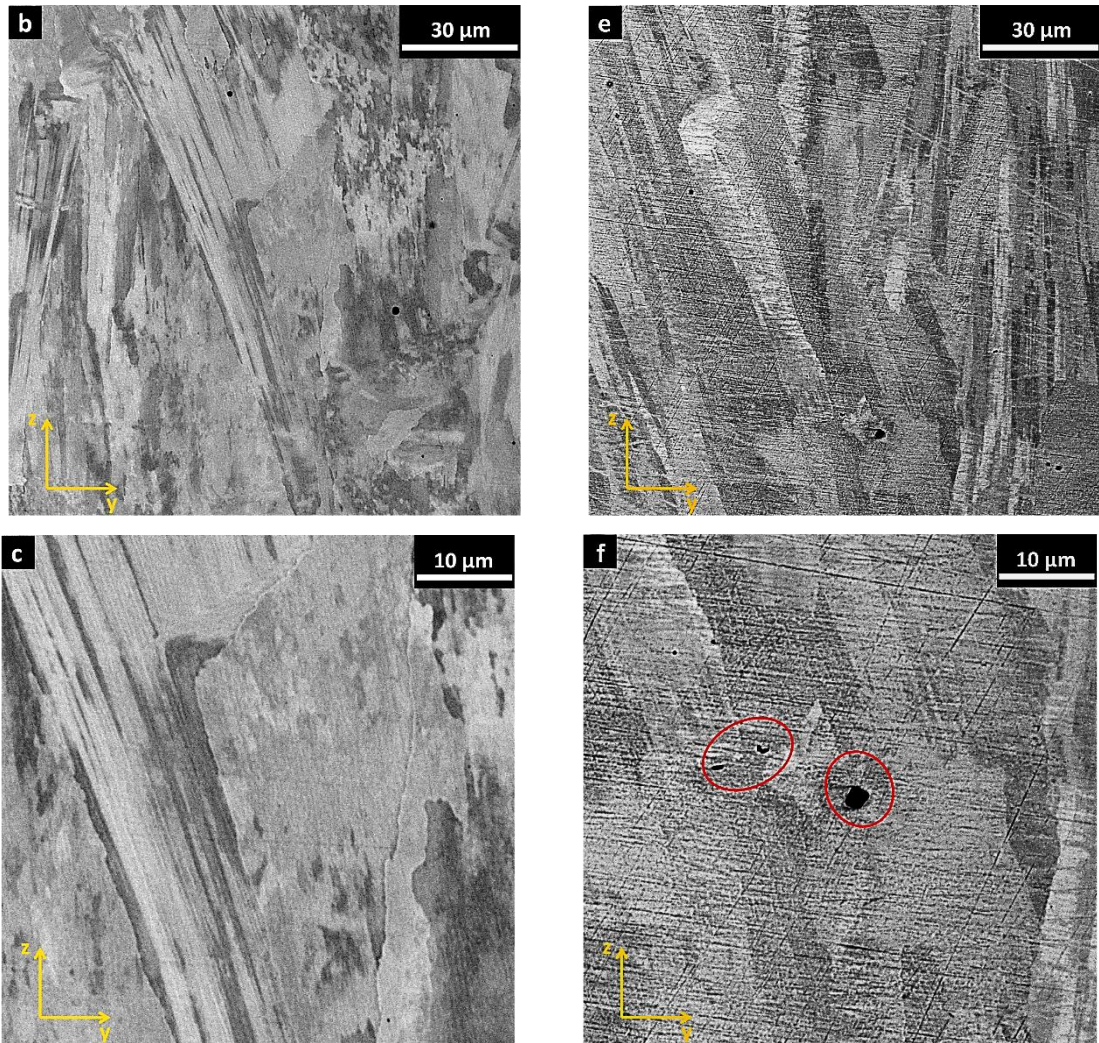


Figure 52: SEM images of the alloy (a-c) and the composite (d-f) samples in HT3 conditions along the building direction (z-axis) at 500x, 2000x, 5000x. In red are highlighted TiC particles.

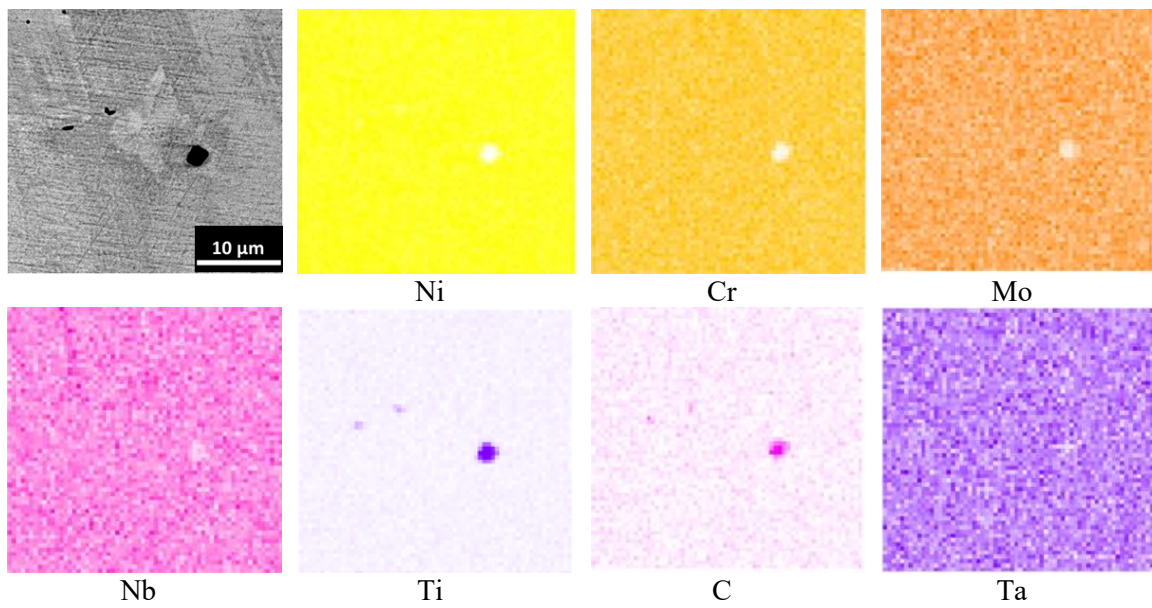


Figure 53: EDS maps of the composite sample in HT3 conditions at 3000x, showing the presence of TiC particles.

The OM images in Figure 54 show the plane x-y of the alloy (a-c) and the composite (d-f) at different magnifications. The melt pools are still widely visible in the composite, probably due the fact that TiC particles (highlighted in red) tend to increase the thermal stability of the material.

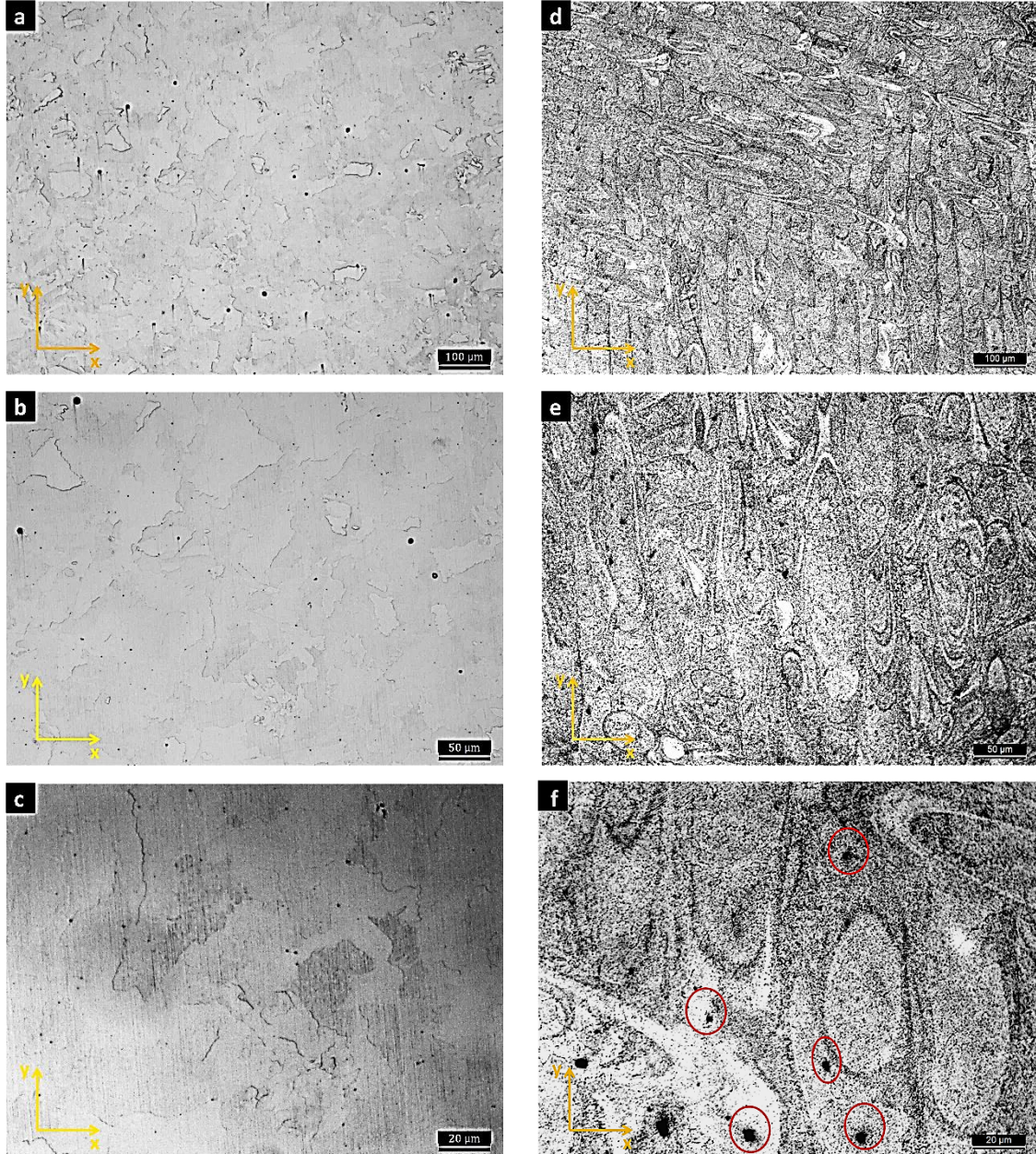


Figure 54: OM images of the alloy (a-c) and the composite (d-f) in HT3 conditions at 100x, 200x and 500x along the x-y plane. In red are highlighted TiC particles.

6.3.5 Microstructure of samples solutioned at 870 °C for 1 hour (HT4)

OM images in Figure 55 and SEM images in Figure 56 show the microstructure in the building direction (z-axis) of the alloy (a-c) and the composite (d-f) in HT4 conditions. Both the materials present columnar grain along the building direction, even if the composite presents

finer grains. In both the materials melt pools are still visible. At higher magnification is possible to observe the presence of precipitates, probably carbides or delta phases formed during the thermal exposure along the grain boundaries. EDS maps in Figure 57 confirm the presence of large TiC particles, along the grain boundaries and inside the grains. Columnar and cellular dendritic structures are still visible in both the material.

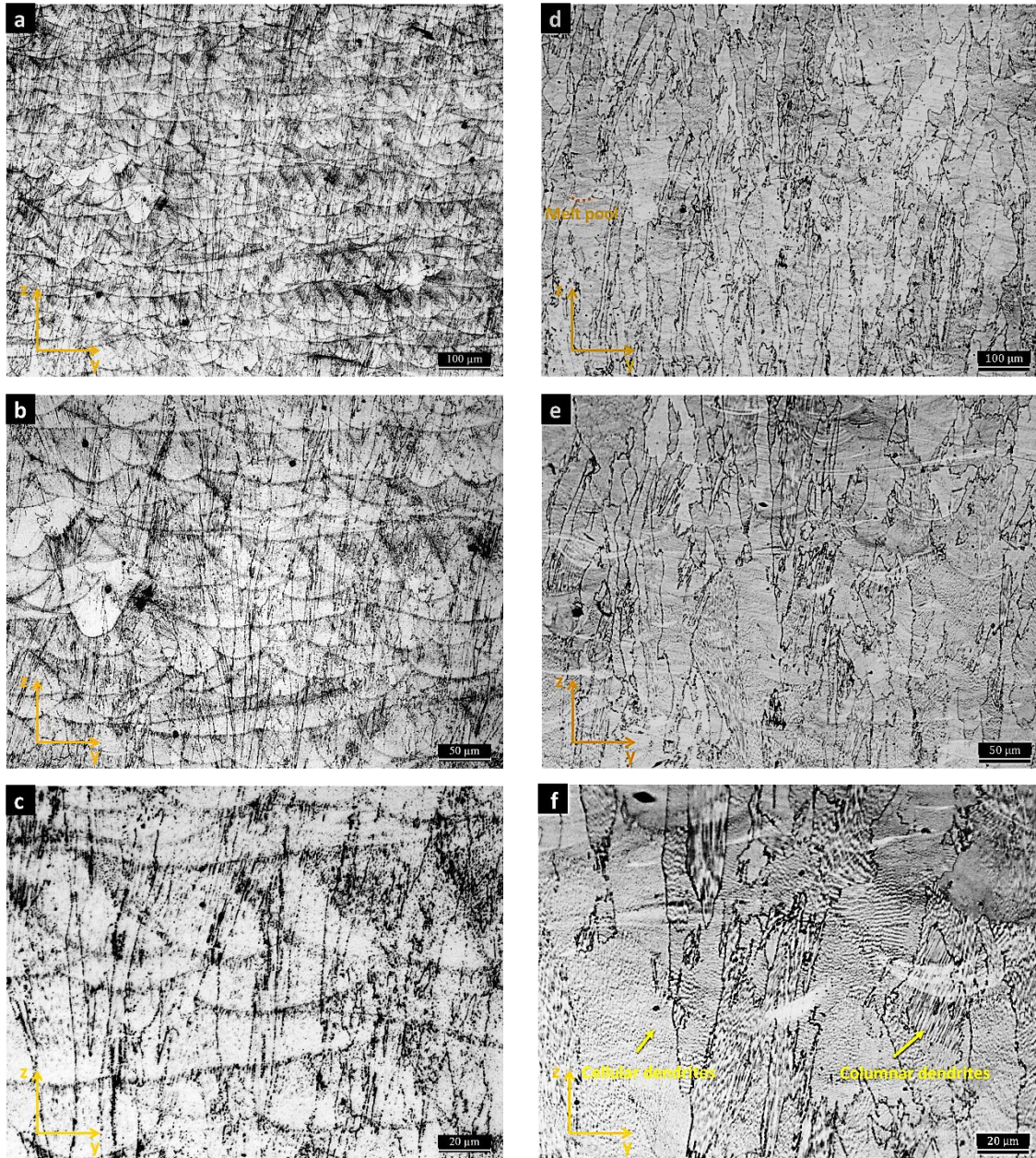


Figure 55: OM images of the alloy (a-c) and the composite (d-f) in HT4 conditions at 100x, 200x and 500x along the building direction (z-axis).

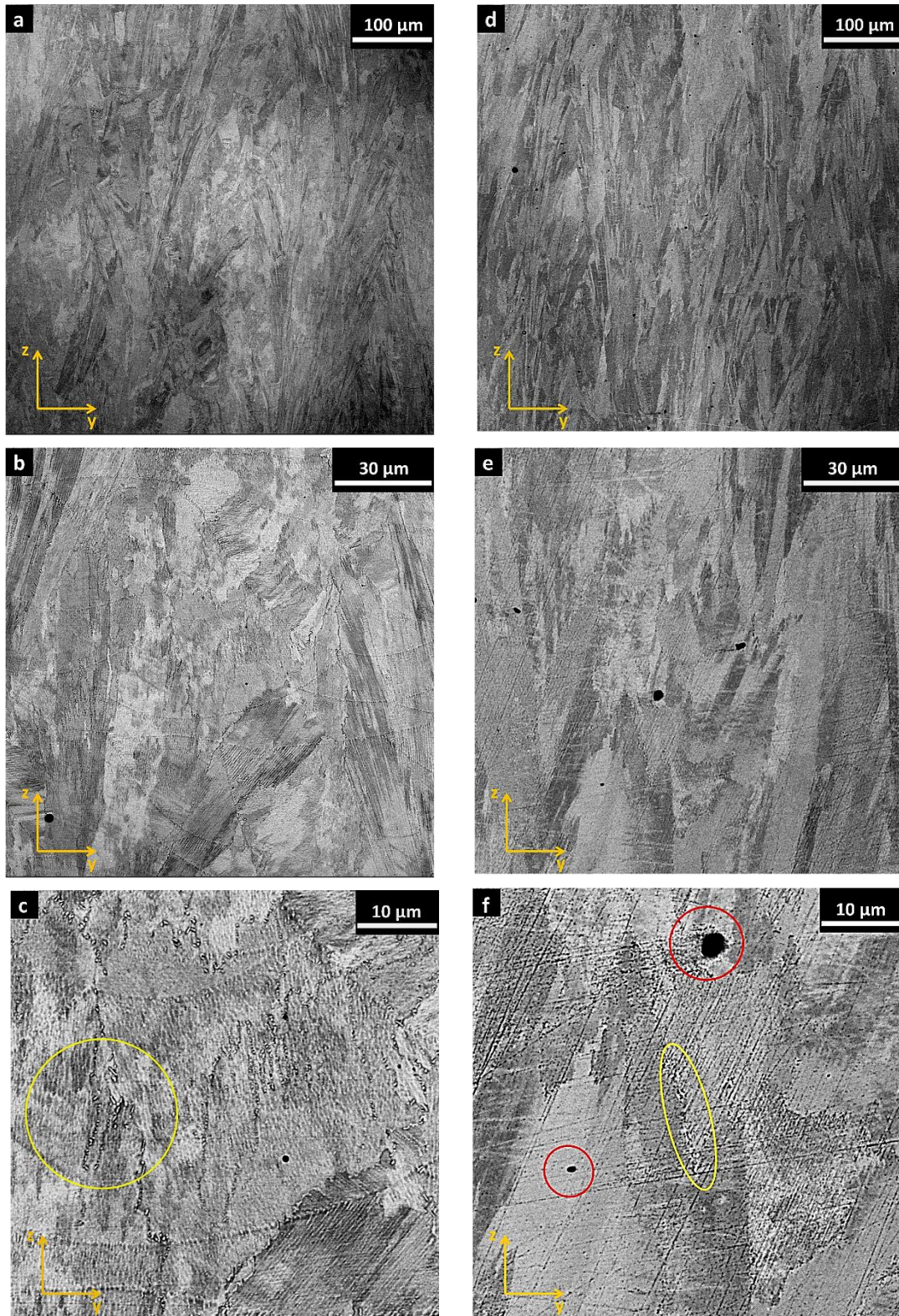


Figure 56: SEM images of the alloy (a-c) and the composite (d-f) samples in HT4 conditions along the building direction (z-axis) at 500x, 2000x, 5000x. In red are highlighted TiC particles, in yellow carbides in grain boundaries.

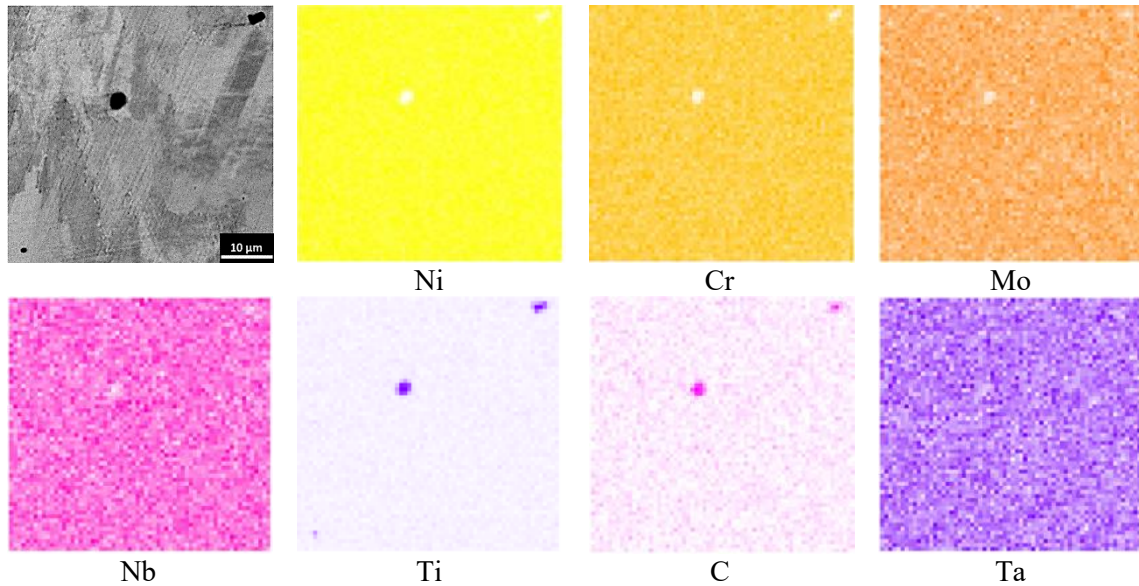
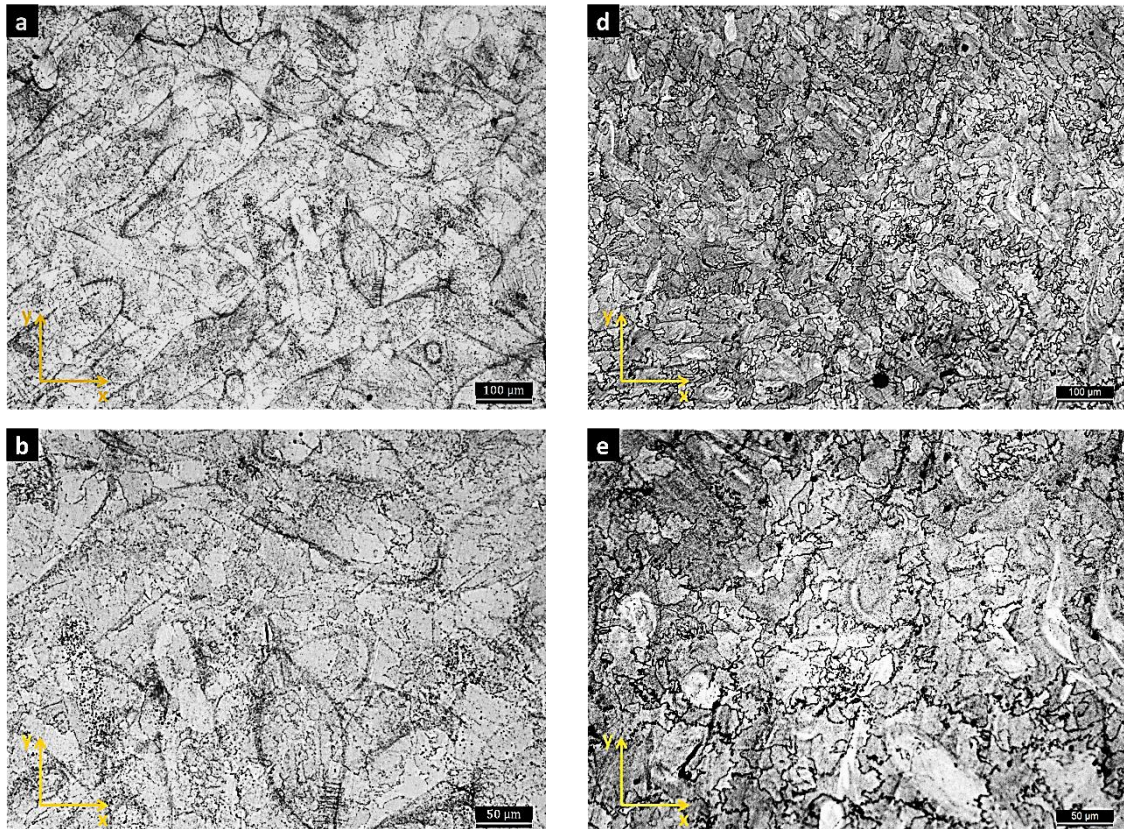


Figure 57: EDS maps of the composite sample in HT4 conditions at 3000x showing the presence of TiC particles.

The OM images in Figure 58 show the plane x-y of the alloy (a-c) and the composite (d-f) at different magnifications. The images highlight the melt pools, which do not disappear at 870 °C. Even in this case the grains dimension is lower in the composite. In particular, in Figure 58 f shows a zone where the presence of various TiC particles tends to further refine the grains (highlighted in red) which confirm the fact that the TiC particles have a key role in controlling the size of the grains.



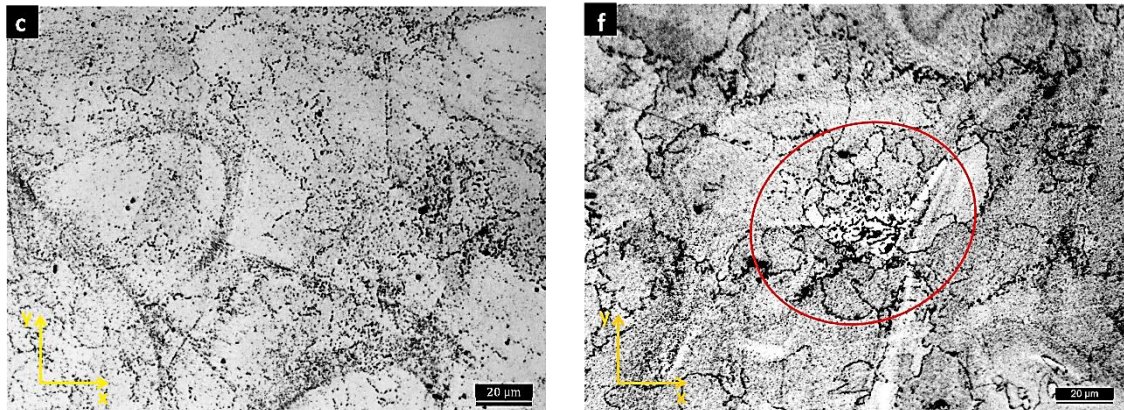
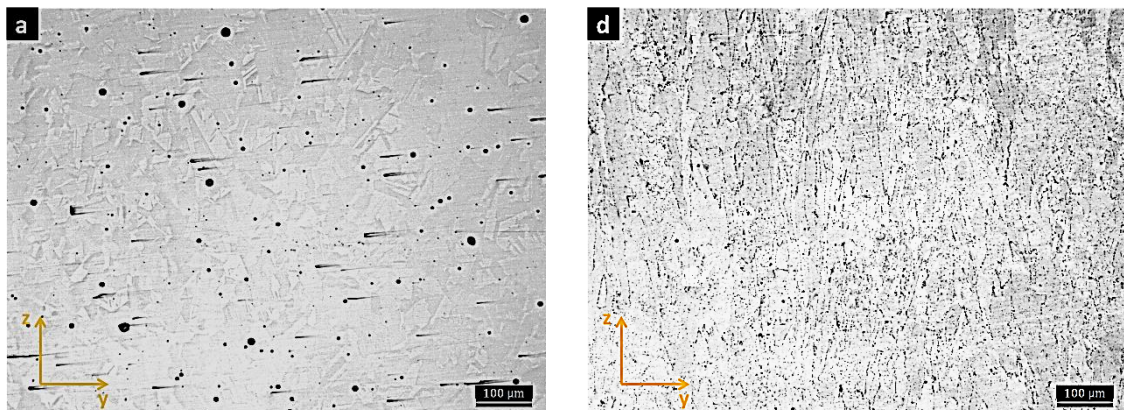


Figure 58: OM images of the alloy (a-c) and the composite (d-f) in HT4 conditions at 100x, 200x and 500x along the x-y plane. In f is highlighted in red a zone where the presence of a large number of TiC particles tends to refine the crystalline structure.

6.3.6 Microstructure of samples solutioned at 1190 °C for 2 hours (HT5)

This heat treatment at 1190 °C for 2 hours was carried out to see if the higher temperature, compared with the HT1 condition, affects the recrystallization of the composite. The temperature of 1190 °C was chosen. OM images in Figure 59 and SEM images in Figure 60 show that in the alloy there are not substantial differences compared to the HT1 condition. The concentration of precipitates in the composite is lower than the HT1 condition, and some twin boundaries appear more frequently. The fact that the composite present columnar grains even at temperatures close to the melting point may mean that the material has better mechanical properties and creep resistance at high temperature, compared with the alloy.



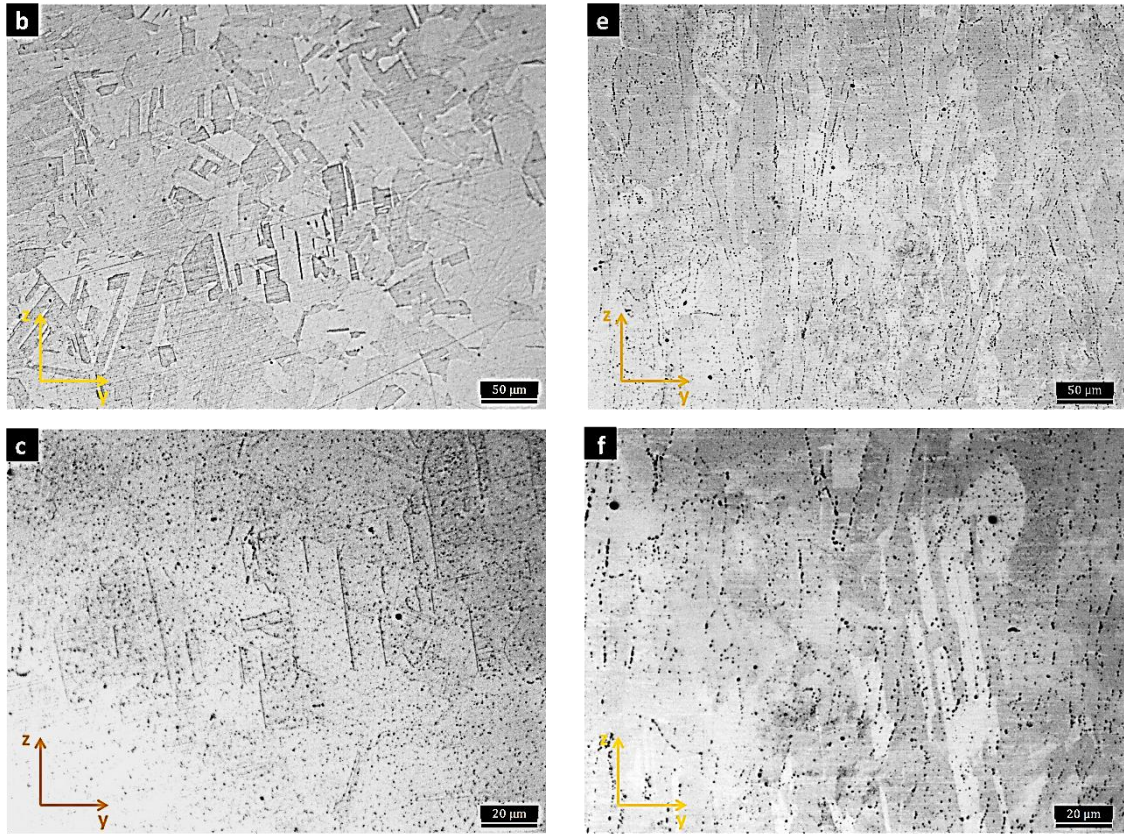
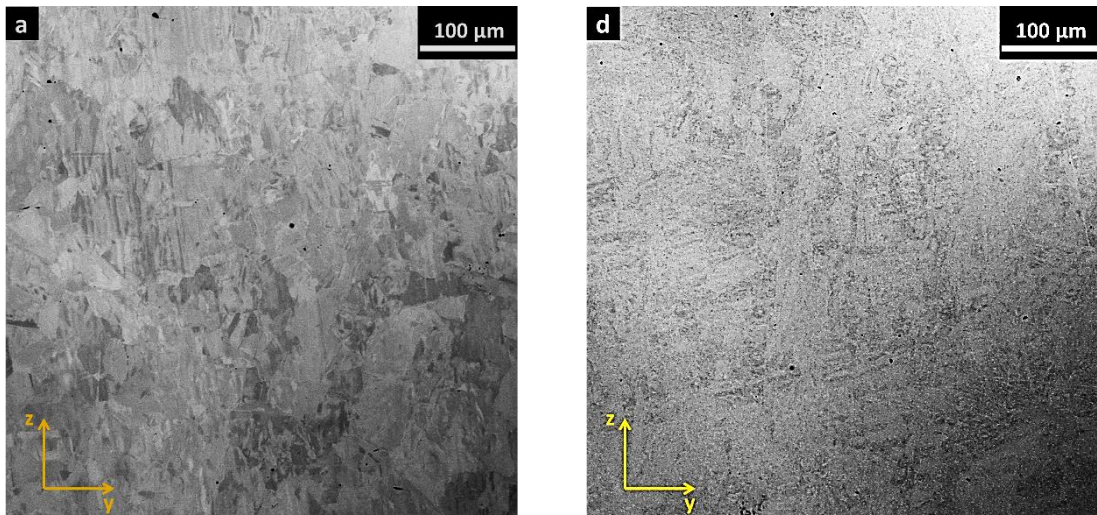


Figure 59: OM images of the alloy (a-c) and the composite (d-f) in HT5 conditions at 100x, 200x and 500x along the building direction (z-axis).



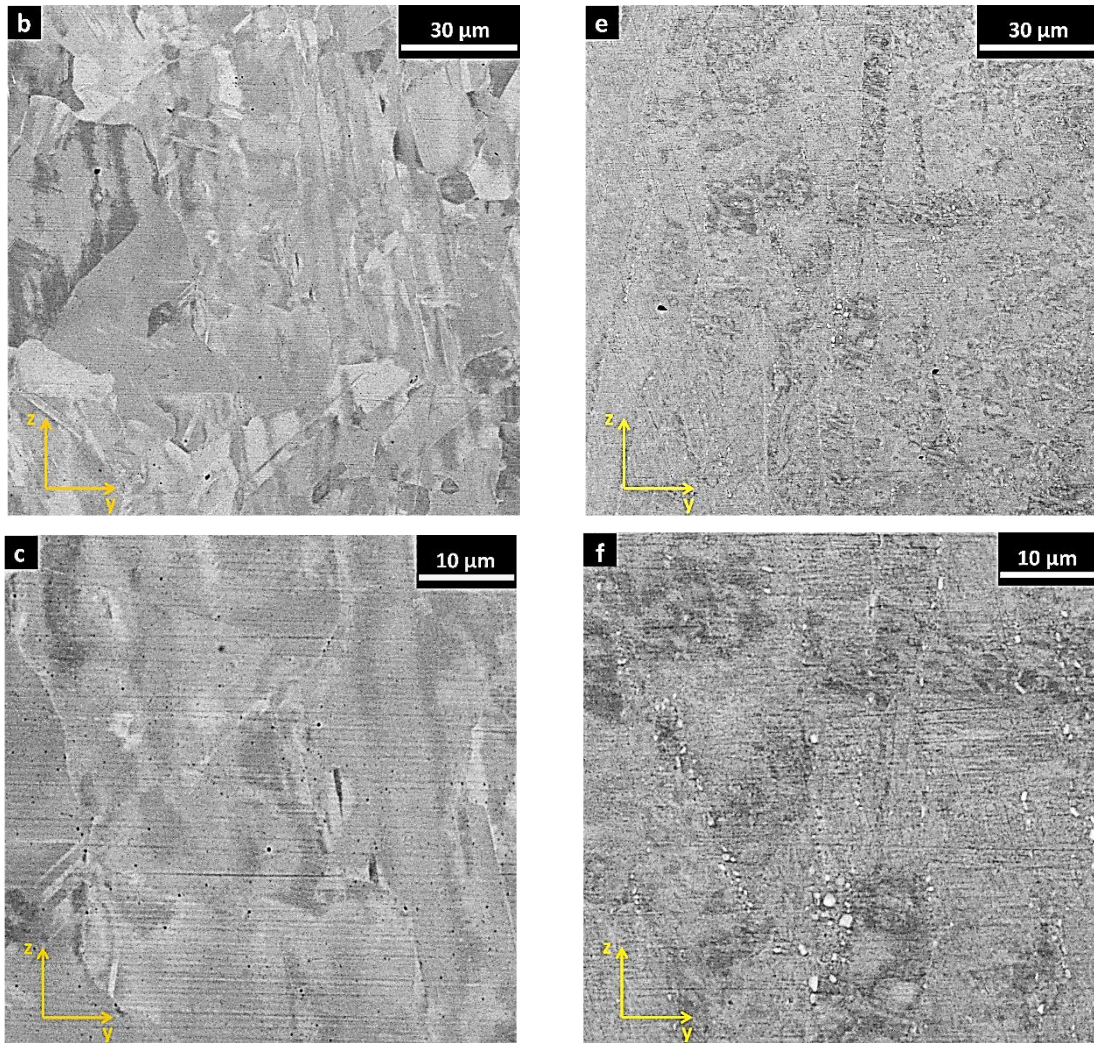


Figure 60: SEM images of the alloy (a-c) and the composite (d-f) samples in HT5 conditions along the building direction (z-axis) at 500x, 2000x, 5000x.

6.4 Brinell hardness tests

Results of Brinell hardness test are shown in Figure 61 and Table 8.

- In AB condition the hardness of the composite is 312 HBW, that is 6 % higher than the alloy. The introduction of ceramic particles slightly increased the hardness of the composite material.
- In HT1 conditions the hardness of the composite is 254 HBW that is 36 % higher than the alloy in the same conditions. This great difference is probably due to the TiC particles along the grain boundaries limiting the recrystallization and grain growth and from the higher dimension of precipitates than the alloy.
- In HT2 conditions the hardness of the composite is 354 HBW that is 28 % higher than the alloy. The higher hardness than the HT1 condition is caused by the phased formation like γ'' phases.
- In HT3 conditions the hardness of the composite is 301 HBW, that is 13 % higher than the alloy. For this temperature occurs carbides formation as well as dendritic structures dissolution.

- In HT4 conditions the hardness of the composite is 319 HBW that is 17 % higher than the alloy. It is interesting to note that this value is higher than the AB condition, probably thanks to the precipitation of a high number of δ phases.
- In HT5 conditions the hardness of the composite is 248 HBW, that is 25 % higher than the alloy. It can be noticed that the hardness is slightly lower than the HT1 condition, probably because of the higher level of recrystallization and the lower number of precipitates.

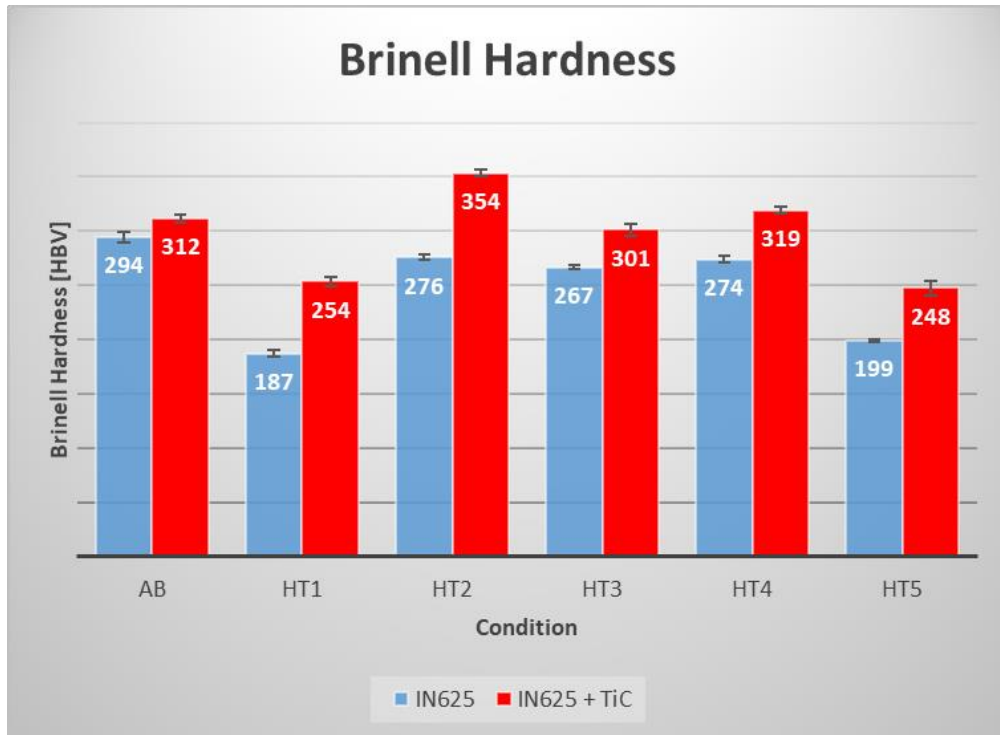


Figure 61: Brinell hardness results.

Table 8: Brinell hardness results. In blue are highlighted the results of the alloy, in red for the composite.

Condition	Description	Brinell Hardness [HBV]		St. dev		Var. %
AB	-	294	312	5	4	6 %
HT1	S 1150 °C for 2 h	187	254	3	4	36 %
HT2	S 1150 °C for 2h + A 700 °C for 8 h	276	354	3	3	28 %
HT3	S 980 °C for 1 h	267	301	2	5	13 %
HT4	S 870 °C for 1 h	274	319	3	3	17 %
HT5	S 1190 °C for 2 h	199	248	2	7	25 %

Summarizing, TiC particles have a general hardening effect in the composite because of the hard nature of the ceramic particles. The effect is more evident in HT1 condition where the solutioning at 1150 °C is not sufficient to recrystallize the grains, due to the fact that TiC particles improve the thermal stability of the composite.

6.5 Tensile tests

Figure 62 shows the result of the tensile tests performed in AB and HT1 conditions. The values were normalized. The following considerations can be drawn:

- In AB condition the composite presents the highest UTS and YS with the lowest elongation. The AB alloy presents lower tensile strengths but superior elongation at failure. It is clear that the composite present superior mechanical properties, but with an unavoidable decrease of the ductility.
- HT1 composite presents higher tensile strengths and lower elongation at failure than HT1 base alloy. This indicated that the composite presents a more microstructure stability at higher temperature than the base alloy.

In general, the adding of TiC particles tends to improve the tensile properties of the Inconel 625 which are strongly related to the hardness of the ceramic particles. Moreover, for the HT1 condition, the main effect of the TiC reinforcement is to limit the recrystallization, reducing the mechanical alterations.

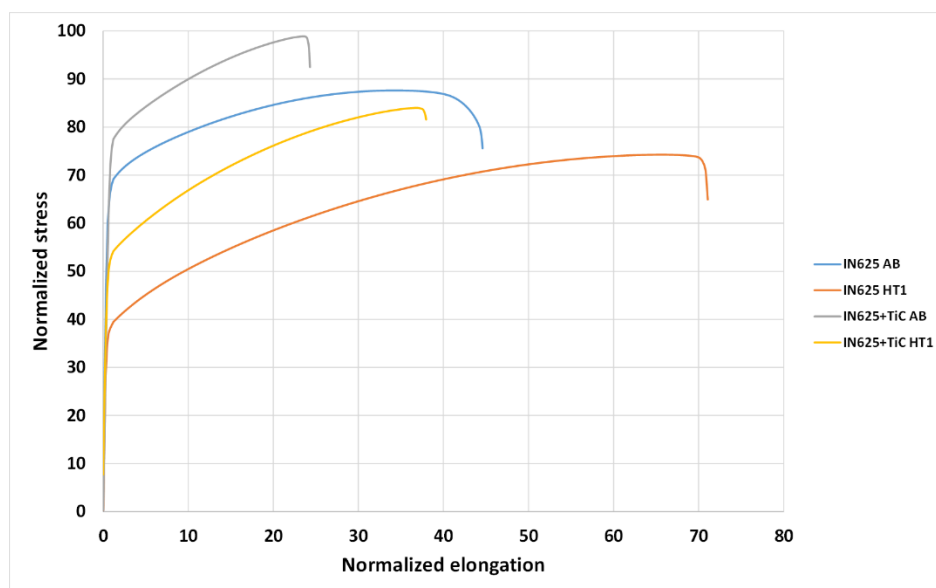


Figure 62: Tensile tests result of the alloy and composite in AB and HT1 conditions.

7 Conclusions

In this thesis, it was fabricated the TiC/Inconel 625 composite by LPBF with micrometric TiC particles. The study started with a feasibility study of the powders of Inconel 625 with different contents of TiC through the flowability test, showing that only the powder with 1 wt. % of TiC flows through the Carney flowmeter with a flow time of 14.5 ± 0.5 s, indicating that a higher content of TiC in these conditions may cause a non-uniform layer of powder inside the building chamber, thus creating defects during the process. Afterward, the following stages of the study focused on the Inconel 625 + 1 wt. % TiC composite processed by LPBF, comparing the results with the Inconel 625 alloy.

Different samples of the composite were produced in order to find out the optimal process parameters. The results have shown that it is necessary to increase the VED to obtain the minimum percentage of porosity compared with the base alloy because of the addition of the TiC particles altering the viscosity of the melt pools. It was found that the optimal parameters occur with a VED of 198 J/mm^3 . At lower VED, a major number of defects remained.

The analysis of the microstructure shows large differences between the alloy and the composite. In particular, the presence of TiC particles tends to refine the grains, inhibiting the grain growth during the application of heat treatments at high temperatures. From the samples heat-treated with a solubilization treatment at $1150 \text{ }^\circ\text{C}$ for 2 hours, it resulted that the composite still presents columnar grains, even if seems that the recrystallization started, while the alloy already presents full equiaxed grains.

The different microstructures involve different mechanical properties. In fact, the TiC particles tend to harden the material in the AB state of about 5 % in the composite, but the main differences occur in the heat-treated samples at high temperatures (HT1 condition), with a difference up to 36 %, because of the limited recrystallization and grain growth in contrast to base alloy. In particular, it was found the highest Brinell hardness in HT2 condition (354 HBV) which includes a solutioning treatment at $1150 \text{ }^\circ\text{C}$ for 2 hours and an ageing treatment at $700 \text{ }^\circ\text{C}$ where forms also the γ'' phase. The improvement of hardness is also related to the higher UTS and YS but with a reduced ductility.

These results may make the TiC/IN625 obtained by LPBF a possible candidate material for aerospace applications. For example, the presence of columnar grains after the heat treatments at high temperatures may indicate that the composite could be applied for components that require a higher operative temperature than the pure Inconel alloy and that it could present a higher creep resistance. The next steps may be the study of the corrosion and oxidation resistance at high temperatures as well as its fatigue and creep properties.

8 References

- [1] R. Liu, Z. Wang, T. Sparks, F. Liou, and J. Newkirk, "Aerospace applications of laser additive manufacturing," *Laser Additive Manufacturing: Materials, Design, Technologies, and Applications*. pp. 351–371, 2017, doi: 10.1016/B978-0-08-100433-3.00013-0.
- [2] S. Cooke, K. Ahmadi, S. Willerth, and R. Herring, "Metal additive manufacturing: Technology, metallurgy and modelling," *J. Manuf. Process.*, vol. 57, no. August, pp. 978–1003, 2020, doi: 10.1016/j.jmapro.2020.07.025.
- [3] S. Biamino, "Appunti del corso 'Materiali per applicazioni Aerospaziali.'" 2019.
- [4] F. Calignano *et al.*, "Overview on additive manufacturing technologies," *Proc. IEEE*, vol. 105, no. 4, pp. 593–612, 2017, doi: 10.1109/JPROC.2016.2625098.
- [5] S. Zakeri, M. Vippola, and E. Levänen, "A comprehensive review of the photopolymerization of ceramic resins used in stereolithography," *Addit. Manuf.*, vol. 35, no. February, p. 101177, 2020, doi: 10.1016/j.addma.2020.101177.
- [6] K. V. Wong and A. Hernandez, "A Review of Additive Manufacturing," *ISRN Mech. Eng.*, vol. 2012, pp. 1–10, 2012, doi: 10.5402/2012/208760.
- [7] H. K. D. H. Bhadeshia, *Additive manufacturing*, vol. 32, no. 7. 2016.
- [8] AMFG, "Metal 3D Printing: What is Direct Energy Deposition?," 2018. <https://amfg.ai/2018/09/27/metal-3d-printing-what-is-direct-energy-deposition/?cn-reloaded=1> (accessed Oct. 30, 2020).
- [9] D. S. Shim, G. Y. Baek, and E. M. Lee, "Effect of substrate preheating by induction heater on direct energy deposition of AISI M4 powder," *Materials Science and Engineering A*, vol. 682. pp. 550–562, 2017, doi: 10.1016/j.msea.2016.11.029.
- [10] Д. Кокс, "Powder Characterization and Optimization for Additive Manufacturing.," *Russ. Union Cat. Sci. Lit.*, vol. 6, no. 3, pp. 1–6, 2013, [Online]. Available: http://library.gpntb.ru/cgi-bin/irbis64r/62/cgiirbis_64.exe?C21COM=S&I21DBN=RSK&P21DBN=RSK&S21FMT=fullwebr&Z21ID=&S21STN=1&S21REF=10&Z21MFN=856891.
- [11] R. Koike *et al.*, "Graphical Evaluation Method for Void Distribution in Direct Energy Deposition," *Procedia Manuf.*, vol. 6, pp. 105–112, 2016, doi: 10.1016/j.promfg.2016.11.014.
- [12] S. Anwar, N. Ahmed, S. Pervaiz, S. Ahmad, A. Mohammad, and M. Saleh, "On the turning of electron beam melted gamma-TiAl with coated and uncoated tools: A machinability analysis," *J. Mater. Process. Technol.*, vol. 282, no. February, 2020, doi: 10.1016/j.jmatprotec.2020.116664.
- [13] G. Marchese *et al.*, "Influence of heat treatments on microstructure evolution and mechanical properties of Inconel 625 processed by laser powder bed fusion," *Mater. Sci. Eng. A*, vol. 729, no. May, pp. 64–75, 2018, doi: 10.1016/j.msea.2018.05.044.
- [14] M. Salarian, H. Asgari, and M. Vlasea, "Pore space characteristics and corresponding effect on tensile properties of Inconel 625 fabricated via laser powder bed fusion,"

- Mater. Sci. Eng. A*, vol. 769, no. August 2019, p. 138525, 2020, doi: 10.1016/j.msea.2019.138525.
- [15] S. A. Farzadfar, M. J. Murtagh, and N. Venugopal, "Impact of IN718 bimodal powder size distribution on the performance and productivity of laser powder bed fusion additive manufacturing process," *Powder Technol.*, vol. 375, pp. 60–80, 2020, doi: 10.1016/j.powtec.2020.07.092.
- [16] L. Jiao, Z. Y. Chua, S. K. Moon, J. Song, G. Bi, and H. Zheng, "Femtosecond laser produced hydrophobic hierarchical structures on additive manufacturing parts," *Nanomaterials*, vol. 8, no. 8, 2018, doi: 10.3390/nano8080601.
- [17] Q. B. Nguyen, M. L. S. Nai, Z. Zhu, C. N. Sun, J. Wei, and W. Zhou, "Characteristics of Inconel Powders for Powder-Bed Additive Manufacturing," *Engineering*, vol. 3, no. 5, pp. 695–700, 2017, doi: 10.1016/J.ENG.2017.05.012.
- [18] G. Marchese *et al.*, "The influence of the process parameters on the densification and microstructure development of laser powder bed fused inconel 939," *Metals (Basel)*, vol. 10, no. 7, pp. 1–19, 2020, doi: 10.3390/met10070882.
- [19] G. Marchese *et al.*, "Characterization and Comparison of Inconel 625 Processed by Selective Laser Melting and Laser Metal Deposition," *Adv. Eng. Mater.*, vol. 19, no. 3, pp. 1–9, 2017, doi: 10.1002/adem.201600635.
- [20] M. Javidani, J. Arreguin-Zavala, J. Danovitch, Y. Tian, and M. Brochu, "Additive Manufacturing of AlSi10Mg Alloy Using Direct Energy Deposition: Microstructure and Hardness Characterization," *J. Therm. Spray Technol.*, vol. 26, no. 4, pp. 587–597, 2017, doi: 10.1007/s11666-016-0495-4.
- [21] B. Zhang, Y. Li, and Q. Bai, "Defect Formation Mechanisms in Selective Laser Melting: A Review," *Chinese J. Mech. Eng. (English Ed.)*, vol. 30, no. 3, pp. 515–527, 2017, doi: 10.1007/s10033-017-0121-5.
- [22] B. Vrancken, R. Wauthle, J. P. Kruth, and J. Van Humbeeck, "Study of the influence of material properties on residual stress in selective laser melting," *24th Int. SFF Symp. - An Addit. Manuf. Conf. SFF 2013*, pp. 393–407, 2013.
- [23] S. Li, G. Chen, S. Katayama, and Y. Zhang, "Relationship between spatter formation and dynamic molten pool during high-power deep-penetration laser welding," *Appl. Surf. Sci.*, vol. 303, pp. 481–488, 2014, doi: 10.1016/j.apsusc.2014.03.030.
- [24] Y. Liu, Y. Yang, S. Mai, D. Wang, and C. Song, "Investigation into spatter behavior during selective laser melting of AISI 316L stainless steel powder," *Mater. Des.*, vol. 87, pp. 797–806, 2015, doi: 10.1016/j.matdes.2015.08.086.
- [25] C. Meier, R. W. Penny, Y. Zou, J. S. Gibbs, and A. J. Hart, "Thermophysical phenomena in metal additive manufacturing by selective laser melting: Fundamentals, modeling, simulation and experimentation," *arXiv*, 2017, doi: 10.1615/annualrevheattransfer.2018019042.
- [26] "Additive at Scale: Avio Aero Flies into the Future," *GE Additive*, 2021. <https://www.ge.com/additive/stories/additive-at-scale-avio-aero> (accessed Jan. 07, 2021).
- [27] R. C. Reed, "The superalloys, fundamentals and applications." Cambridge University Press, 2006, doi: <https://doi.org/10.1017/CBO9780511541285>.

- [28] M. J. Donachie and S. J. Donachie, "Superalloys: a technical guide." p. 439, 2002, [Online]. Available: <http://books.google.com/books?hl=en&lr=&id=vjCJ5pI1QpkC&pgis=1>.
- [29] A. Mouritz, "Introduction to Aerospace Materials," *Introduction to Aerospace Materials*. 2012, doi: 10.2514/4.869198.
- [30] G. Marchese *et al.*, "Role of the chemical homogenization on the microstructural and mechanical evolution of prolonged heat-treated laser powder bed fused Inconel 625," *Mater. Sci. Eng. A*, vol. 796, no. January, p. 140007, 2020, doi: 10.1016/j.msea.2020.140007.
- [31] "Turbofan schematic." [https://commons.wikimedia.org/wiki/File:Turbofan_operation_\(lbp\).png](https://commons.wikimedia.org/wiki/File:Turbofan_operation_(lbp).png) (accessed Dec. 11, 2020).
- [32] L. Casalino and D. Pastrone, "Appunti del corso 'fondamenti di macchine e propulsione.'" .
- [33] T. Okura, "Materials for Aircraft Engines," *Aircr. Propuls. Final Rep.*, vol. ASEN 5063, pp. 1–14, 2015.
- [34] "Inconel Alloy 625 in Aerospace Engineering," *Jaiman Metalloys LLP*, 2020. <https://www.blog.jaimannickelalloys.com/inconel-alloy-625-in-aerospace-engineering/> (accessed Jan. 09, 2021).
- [35] Rolls-Royce, *The Jet Engine*, 5th ed. London: Rolls-Royce, Print., 2005.
- [36] Q. Yu, C. Wang, Z. Zhao, C. Dong, and Y. Zhang, "New Ni-based superalloys designed for laser additive manufacturing," *J. Alloys Compd.*, no. xxxx, p. 157979, 2020, doi: 10.1016/j.jallcom.2020.157979.
- [37] Y. Zhao, Q. Guo, Z. Ma, and L. Yu, "Comparative study on the microstructure evolution of selective laser melted and wrought IN718 superalloy during subsequent heat treatment process and its effect on mechanical properties," *Mater. Sci. Eng. A*, vol. 791, no. June, p. 139735, 2020, doi: 10.1016/j.msea.2020.139735.
- [38] B. Riquelme, M. Vergara, C. Altamirano, and M. F. Cavieres, "Effect of the scanning strategy on microstructure and mechanical anisotropy of HastelloyX superalloy produced by Laser Powder Bed Fusion," *Toxicol. Vitr.*, p. 104947, 2020, doi: 10.1016/j.matchar.2021.110951.
- [39] G. Marchese *et al.*, "The role of texturing and microstructure evolution on the tensile behavior of heat-treated Inconel 625 produced via laser powder bed fusion," *Mater. Sci. Eng. A*, vol. 769, no. July 2019, p. 138500, 2020, doi: 10.1016/j.msea.2019.138500.
- [40] G. Marchese *et al.*, "Microstructural investigation of as-fabricated and heat-treated Inconel 625 and Inconel 718 fabricated by direct metal laser sintering: contribution of Politecnico di Torino and Istituto Italiano di Tecnologia (IIT) di Torino," *Met. Powder Rep.*, vol. 71, no. 4, pp. 273–278, 2016, doi: 10.1016/j.mprp.2016.06.002.
- [41] C. Guo *et al.*, "Single-track investigation of IN738LC superalloy fabricated by laser powder bed fusion: Track morphology, bead characteristics and part quality," *J. Mater. Process. Technol.*, vol. 290, no. September 2020, p. 117000, 2021, doi: 10.1016/j.jmatprotec.2020.117000.

- [42] A. S. Shaikh, F. Schulz, K. Minet-Lallemand, and E. Hryha, "Microstructure and Mechanical Properties of Haynes 282 Superalloy Produced by Laser Powder Bed Fusion," *Mater. Today Commun.*, vol. 26, no. January, p. 102038, 2021, doi: 10.1016/j.mtcomm.2021.102038.
- [43] J. H. Boswell, D. Clark, W. Li, and M. M. Attallah, "Cracking during thermal post-processing of laser powder bed fabricated CM247LC Ni-superalloy," *Mater. Des.*, vol. 174, p. 107793, 2019, doi: 10.1016/j.matdes.2019.107793.
- [44] H. L. Eiselstein and D. J. Tillack, "The Invention and Definition of Alloy 625," pp. 1–14, 2012, doi: 10.7449/1991/superalloys_1991_1_14.
- [45] V. Shankar, K. Bhanu Sankara Rao, and S. L. Mannan, "Microstructure and mechanical properties of Inconel 625 superalloy," *J. Nucl. Mater.*, vol. 288, no. 2–3, pp. 222–232, 2001, doi: 10.1016/S0022-3115(00)00723-6.
- [46] Special Metals Corporation, "Specification Sheet: Inconel Alloy 625," *Spec. Met. Corp.*, vol. 625, no. 2, pp. 1–28, 2013.
- [47] S. K. Rai, A. Kumar, V. Shankar, T. Jayakumar, K. B. S. Rao, and B. Raj, "Characterization of microstructures in Inconel 625 using X-ray diffraction peak broadening and lattice parameter measurements," *Scr. Mater.*, vol. 51, no. 1, pp. 59–63, 2004, doi: 10.1016/j.scriptamat.2004.03.017.
- [48] L. E. Shoemaker, "Alloys 625 and 725: Trends in properties and applications," *Proc. Int. Symp. Superalloys Var. Deriv.*, pp. 409–418, 2005, doi: 10.7449/2005/superalloys_2005_409_418.
- [49] S. Floreen, G. E. Fuchs, and W. J. Yang, "The Metallurgy of Alloy 625," pp. 13–37, 2012, doi: 10.7449/1994/superalloys_1994_13_37.
- [50] "EOS NichelAlloy IN625." https://www.eos.info/03_system-related-assets/material-related-contents/metal-materials-and-examples/metal-material-datasheet/nickelalloy-inconel/niall-in625-m290_material_data_sheet_06-17_en.pdf (accessed Dec. 21, 2020).
- [51] I. Moore, "ResearchGate." https://www.researchgate.net/figure/Schematic-Time-Temperature-Transformation-TTT-diagram-for-solution-annealed-wrought_fig1_310605881 (accessed Dec. 21, 2020).
- [52] "Nickel 625 vs. Nickel 725," *MakeItFrom.com*. <https://www.makeitfrom.com/compare/Nickel-Alloy-625-N06625-NA21/Nickel-Alloy-725-N07725> (accessed Feb. 08, 2021).
- [53] I. Yadroitsev, L. Thivillon, P. Bertrand, and I. Smurov, "Strategy of manufacturing components with designed internal structure by selective laser melting of metallic powder," *Appl. Surf. Sci.*, vol. 254, no. 4, pp. 980–983, 2007, doi: 10.1016/j.apsusc.2007.08.046.
- [54] D. E. Cooper, N. Blundell, S. Maggs, and G. J. Gibbons, "Additive layer manufacture of Inconel 625 metal matrix composites, reinforcement material evaluation," *J. Mater. Process. Technol.*, vol. 213, no. 12, pp. 2191–2200, 2013, doi: 10.1016/j.jmatprotec.2013.06.021.
- [55] L. Chen, Y. Sun, L. Li, and X. Ren, "Effect of heat treatment on the microstructure and high temperature oxidation behavior of TiC/Inconel 625 nanocomposites fabricated by

- selective laser melting,” *Corros. Sci.*, vol. 169, no. March, p. 108606, 2020, doi: 10.1016/j.corsci.2020.108606.
- [56] L. Chen, Y. Sun, L. Li, and X. Ren, “Microstructure evolution, mechanical properties, and strengthening mechanism of TiC reinforced Inconel 625 nanocomposites fabricated by selective laser melting,” *Mater. Sci. Eng. A*, vol. 792, no. June, p. 139655, 2020, doi: 10.1016/j.msea.2020.139655.
- [57] Q. Jia and D. Gu, “Selective laser melting additive manufacturing of TiC/Inconel 718 bulk-form nanocomposites: Densification, microstructure, and performance,” *J. Mater. Res.*, vol. 29, no. 17, pp. 1960–1969, 2014, doi: 10.1557/jmr.2014.130.
- [58] L. Chen, Y. Sun, L. Li, Y. Ren, and X. Ren, “In situ TiC/Inconel 625 nanocomposites fabricated by selective laser melting: Densification behavior, microstructure evolution, and wear properties,” *Appl. Surf. Sci.*, vol. 518, no. March, p. 145981, 2020, doi: 10.1016/j.apsusc.2020.145981.
- [59] B. Zhang, G. Bi, S. Nai, C. N. Sun, and J. Wei, “Microhardness and microstructure evolution of TiB₂ reinforced Inconel 625/TiB₂ composite produced by selective laser melting,” *Opt. Laser Technol.*, vol. 80, pp. 186–195, 2016, doi: 10.1016/j.optlastec.2016.01.010.
- [60] A. Bakkar, M. M. Z. Ahmed, N. A. Alsaleh, M. M. E. S. Seleman, and S. Ataya, “Microstructure, wear, and corrosion characterization of high TiC content Inconel 625 matrix composites,” *J. Mater. Res. Technol.*, vol. 8, no. 1, pp. 1102–1110, 2019, doi: 10.1016/j.jmrt.2018.09.001.
- [61] S. Cao, D. Gu, and Q. Shi, “Relation of microstructure, microhardness and underlying thermodynamics in molten pools of laser melting deposition processed TiC/Inconel 625 composites,” *J. Alloys Compd.*, vol. 692, pp. 758–769, 2017, doi: 10.1016/j.jallcom.2016.09.098.
- [62] D. Kong *et al.*, “Effect of TiC content on the mechanical and corrosion properties of Inconel 718 alloy fabricated by a high-throughput dual-feed laser metal deposition system,” *J. Alloys Compd.*, vol. 803, pp. 637–648, 2019, doi: 10.1016/j.jallcom.2019.06.317.
- [63] R. Wang *et al.*, “Novel selective laser melting processed in-situ TiC particle-reinforced Ni matrix composite with excellent processability and mechanical properties,” *Mater. Sci. Eng. A*, vol. 797, no. June, p. 140145, 2020, doi: 10.1016/j.msea.2020.140145.
- [64] “ASTM B213 – 20 Standard Test Methods for Flow Rate of Metal Powders Using the Hall Flowmeter Funnel,” *ASTM Int.*, pp. 4–6, 2016, doi: 10.1520/B0213-20.2.
- [65] “ASTM B964 – 16 Standard Test Methods for Flow Rate of Metal Powders Using the Carney Funnel,” *ASTM Int.*, pp. 4–6, 2016, doi: 10.1520/B0964-16.2.
- [66] “ASTM B212 – 17 Standard Test Method for Apparent Density of Free-Flowing Metal Powders Using the Hall Flowmeter Funnel,” *ASTM Int.*, vol. 99, no. Reapproved 2006, pp. 1–4, 2013, doi: 10.1520/B0212-17.2.
- [67] “ASTM B417 – 18 Standard Test Method for Apparent Density of Non-Free-Flowing Metal Powders Using the Carney Funnel,” *ASTM Int.*, pp. 11–13, 2012, doi: 10.1520/B0417-18.2.

- [68] S. Bai, N. Perevoshchikova, Y. Sha, and X. Wu, “The effects of selective laser melting process parameters on relative density of the AlSi10Mg parts and suitable procedures of the archimedes method,” *Appl. Sci.*, vol. 9, no. 3, 2019, doi: 10.3390/app9030583.
- [69] ASTM B311-17, “Standard Test Method for Density of Powder Metallurgy (PM) Materials Containing Less Than Two Percent Porosity,” *ASTM Int.*, vol. i, pp. 1–5, 2017, doi: 10.1520/B0311-17.2.
- [70] “Macchina lucidatrice per metalli MECATECH 234,” *Direct Industry*. <https://www.directindustry.it/prod/presi/product-87039-823115.html> (accessed Feb. 02, 2021).
- [71] “Mecatome T210,” *Presi*. <https://www.presi.com/en/product/mecatome-t210/> (accessed Feb. 02, 2021).
- [72] “Inverted Research Microscope for Materials Testing Leica DMI5000 M,” *Leica Microsystems*. <https://www.leica-microsystems.com/products/light-microscopes/p/leica-dmi5000-m/> (accessed Feb. 03, 2021).
- [73] “Phenom XL,” *Phenom-world.com*. https://www.phenom-world.com/downloads/specification_sheets/SPEC_SHEET_PHENOM_XL_2015_LR_1.pdf (accessed Feb. 10, 2021).
- [74] “ASTM E10-18 Standard Test Method for Brinell Hardness of Metallic Materials Standard Test Method for Brinell Hardness of Metallic Materials 1 Standard Test Method for Brinell Hardness of Metallic Materials,” *ASTM Int. West Conshohocken, PA, 2017*, *www.astm.org*, no. June, pp. 1–36, 2012, doi: 10.1520/E0010-18.
- [75] C. van Hengel, “Stress-strain curve,” *Fibre Met. Laminates*, pp. 101–109, 2001, doi: 10.1007/978-94-010-0995-9_7.
- [76] ASTM E8, “ASTM E8/E8M standard test methods for tension testing of metallic materials 1,” *Annu. B. ASTM Stand. 4*, no. C, pp. 1–27, 2010, doi: 10.1520/E0008.

9 Acknowledgements

Vorrei ringraziare la Prof.ssa Sara Biamino per avermi permesso di poter svolgere questo lavoro di tesi sperimentale. Ringrazio il Dott. Giulio Marchese per avermi seguito, aiutato nella stesura della tesi, per tutti gli insegnamenti, i consigli e per la professionalità dimostrata durante questi mesi. Ringrazio Francesco Viola per avermi seguito durante le attività di laboratorio, per i suoi consigli e per la pazienza dimostrata dal primo all'ultimo giorno. Ringrazio i miei genitori e mio fratello Andrea per il loro sostegno morale ed economico avuti nei miei confronti durante tutta la mia carriera universitaria. Infine, ci tengo a ringraziare me stesso per la mia determinazione e fiducia in me stesso che mi hanno permesso di raggiungere il traguardo dopo cinque anni intensi e difficili.